ABSTRACT

Title of Dissertation: Radiative and Cloud Microphysical Effects of Forest Fire Smoke over North America and Siberia

Brian Vant-Hull, Doctor of Philosophy, 2007

Dissertation Directed By: Professor Zhanqing Li, advisor
Department of Atmospheric and Oceanic Science

Aerosol affects climate both through direct radiative effects and by indirect effects on cloud development. Absorbing aerosols have additional influence on the vertical temperature profile of the atmospheric column. Forest fire smoke contributes roughly half of the global absorbing aerosol, with most of the unsupervised burning occurring in the forests of Canada and Siberia.

Radiative effects of smoke are studied for the case of a Canadian smoke plume that blanketed the U.S. mid-Atlantic seaboard. Optical properties derived from aircraft in situ measurements demonstrate that the smoke formed a layer with a base 2 km above the surface, and absorptive heating in this layer could have strengthened and maintained the subsidence inversion responsible for the layer structure. An optical model of the smoke formed from a blend of aircraft and AERONET measurements allows retrieval of the smoke aerosol by satellite, so that comparisons are possible to measurements made by any instrument in the region. For this case an optical model based purely on AERONET measurements provides the best satellite retrieval of

optical depth, but a model based mainly on aircraft measurements agreed best with spectrum wide-forcing measurements, demonstrating the dangers of a simple optical model for all retrievals.

A study done in the Amazonian burning season demonstrates that sun/observation geometry is useful to control bias from shadowed and illuminated portions of clouds. Sub-pixel mixing of cloud and aerosol also produces bias that is minimized for optically thick clouds. Since such biases can never be fully eliminated, the only valid study is a comparison of two data sets with equivalent geometry and so, presumably, equal bias. Canada and Siberia were chosen so that forested areas are compared at the same latitudes. Summertime Canadian aerosol is primarily smoke, while Europe contributes a great deal of sulfate to Siberia aerosol. The average cloud droplet size was significantly smaller in Siberia, as expected from the higher sulfate load with greater activity as cloud condensation nuclei (CCN). The aerosol indirect effect on cloud microphysics increases with aerosol loading in both regions, but much more so in Canada. This is attributed to a large sulfate background in Siberia, so the addition of smoke makes a smaller percentage change to the amount of cloud CCN.

RADIATIVE AND CLOUD MICROPHYSICAL EFFECTS OF FOREST FIRE SMOKE OVER NORTH AMERICA AND SIBERIA

By

Brian Vant-Hull

Dissertation submitted to the Faculty of the Graduate School of the
University of Maryland, College Park, in partial fulfillment
of the requirements for the degree of
Doctor of Philosophy
2007

Advisory Committee:
Professor Zhanqing Li, Chair
Professor Russel R. Dickerson
Professor Daniel Kirk-Davidoff
Professor Rachel Pinker
Dr. Lorraine A. Remer

Preface

This document contains original scientific content produced by the author and collaborators. Significant scientific contributions consist of the following:

1. Comparison of measurement and calculation of the radiative heating in the July 8, 2002 smoke plume that blanketed the Maryland/Virginia area (chapter 2).
2. Satellite retrievals of radiative forcing from the July 8 2002 smoke plume based on the radiative properties measured on the same day and location (chapter 2).
3. A comparison of optical depth and radiative forcing retrievals based on different measurement instruments (chapter 2).
4. A theoretical derivation of the different between effective radius retrievals of shadowed and illuminated clouds based on the scattering angle, with experimental confirmation (chapter 3).
5. The theoretical exploration of the effects of sub-pixel cloud/aerosol mixing on retrievals of optical depth and effective radius, with experimental confirmation (chapter 3).
6. Development and application of a comparison method to study the effects of aerosols on clouds despite three-dimensional biases (chapter 4).
7. A statistical comparison of the effects of aerosol on clouds in Canada and Siberia, demonstrating that for the same aerosol optical depth the average Siberian cloud droplets are smaller than those of Canada. In both regions the slope of the aerosol/effective radius curve increases with aerosol optical depth, though at a greater rate in Canada than Siberia (chapter 4).
8. A statistical demonstration that the cloud liquid water tends to decrease with aerosol loading (chapter 4).

Specific author contributions: All wording of this document is the author's own. All planning and work required to produce the results reported are the author's own, with the following exceptions: in chapter 2 the data reduction and interpretation leading to the plots of figures 2.5-2.11 and tables 2.1 and 2.1 were peformed by Brett Taubman, the lead author of the first paper listed below. I performed the radiative transfer calculations of sections 2.5 through 2.7 at the request of Mr. Taubman.

Published papers based on this work:

Taubman, B.A., L. Marufu, B. Vant-Hull, C. Piety, B. Doddridge, R. Dickerson, Z. Li, "Smoke over Haze: Aircraft Observations of Chemical and Optical Properties and the Effects on Heating Rates and Stability". *J. Geophys. Res.* 109,(D2), 10.1029/2003JD003898, 2004.

Vant-Hull, B., Z. Li, B. Taubman, R. Levy, L. Marufu, F.L. Chang, B. Doddridge, R. Dickerson, "Smoke over Haze: Comparative analysis of satellite, surface radiometer and airborne in-situ measurements of aerosol optical properties and radiative forcing over the eastern U.S.", *J. Geophys. Res.* Doi: 10.1029/2004JD004518, 2004.

Vant-Hull, B., A. Marshak, L. Remer, and Z. Li, "The effects of scattering angle and cumulus cloud geometry on satellite retrievals of cloud drop effective radius". *Geosci. Rem. Sens. Lett.*, **45** No. 4 1039-1045, 2007.

Dedication

To my office mate Tianle, who always knew how to do things differently. To my sometime collaborator Sasha Marshak, who always knew how to do things right. But most of all to my official and honorary advisors, Zhanqing Li and Lorraine Remer, whose management styles were so far on opposite ends of the spectrum that I eventually found where I belonged comfortably in between.

Acknowledgements

My work was funded primarily from two sources, the NASA Graduate Student Researchers Program (GSRP), and the Department of Energy Atmospheric Radiation Measurement (ARM) program. Additional funding came from the NASA Radiation Program Office and a grant from the National Science Foundation. I'd also like to thank the MODIS Atmosphere team and the AERONET team for the continuing efforts to provide the data that is the basis of this work.

Table of Contents

List of Common Acronyms for Meteorology

AIE – aerosol indirect effect

AOD - aerosol optical depth

BT – brightness temperature

CBL – convective boundary layer

CCN - cloud condensation nuclei

COT – cloud optical thickness

GMT – Greenwich mean time

LW – cloud liquid water

MSL – mean sea level

NDVI – normalized vegetation index

NIR - near infrared

OD – optical depth

PBL – planetary boundary layer

PSAP – particle soot absorption photometer

RH – relative humidity

SSA – single scattering albedo

TOA - top of the atmosphere

TPW – total precipitable water

3D – three dimensional

Common Radiation Transfer Symbols

g - asymmetry parameter
σ - optical cross section
τ - optical depth
ω_o - single scattering albedo
r_e – effective radius

Chapter 1: Introduction

1.1 General Comments and Broad Outlines

Aerosols produce significant radiative forcing at the surface, affecting both local weather patterns and global climate [Ramanathan et al, 2001a; Penner et al, 1992]. In the role of cloud condensation nuclei (CCN) aerosols can affect drop sizes [Twomey, 1977; Ackerman et al, 1995; Rosenfeld, 1999]. Absorbing aerosols have the additional effect of heating the atmosphere while cooling the surface, which may impact cloud development both through stabilization of the atmospheric column [Taubman et al, 2004; Ackerman et al, 2000]. Such cloud effects could strongly affect precipitation [Rosenfeld et al, 1999; Ramanathan, 2001]. Smoke from biomass burning, which comprises nearly half of all absorbing aerosol throughout the world [Ramanathan et al, 2001a], have particularly strong effects on surface and atmospheric radiation budgets [Li, 1998b; Li and Kou, 1998]. Though the theory of how aerosol radiative properties directly affects climatic variables is well established, the indirect effect upon clouds remains a largely unsolved problem [Stephens, 2005], and will be a major focus of this thesis. Until the present work, large-scale statistical studies suitable for climate inference have not been performed for forest fire smoke from the temperate forests.

The chapter presents a brief critical review of the state of the field concerning the direct radiative effects of aerosol and the interactions between aerosols and clouds. The concluding section of this chapter outlines the need for the type of study presented in this

thesis. Those who are not familiar with the concepts of radiation transfer, cloud physics or current instrumentation and methods (MODIS, AERONET, etc) are referred to the appendices for brief introductions to each topic.

1.2 Current State of Aerosol Studies

Though the link between aerosols and clouds was established by turn of the century cloud chamber experiments, the concept of aerosols as an active player in direct radiative forcing of the climate system only arose in the late 1960's [Charlson and Pilat, 1969; Yu et al, 2006] followed by an awakening of interest in cloud effects in the 1970's [Hobbs et al, 1970; Fitzgerald et al, 1973; Eagan et al, 1974; Twomey, 1977]. Around the turn of the millennium the field was invigorated by improved instrumentation and methods: the launch of satellites designed with aerosol and cloud retrievals in mind (on the 'A-train': MODIS, POLDER, MISR, CloudSat [Stephens, 2002]), the deployment of AeroNet with the subsequent development of sophisticated retrieval techniques [Holben et al, 1998; Dubovik et al, 2000], increased deployment of micropulse and Raman LIDAR systems [Ferrare et al, 2001], and improved calibration of commercially available in situ particle measurement systems [Anderson and Ogren, 1998; Bond et al, 1999].

The next two sections will be concerned primarily with recent work concerning smoke and clouds. Global or generalized studies will only be discussed in relation to this

narrow topic.

1.2.1 Direct Radiative Effects

The global aerosol system is generally clustered into 5 types [Kaufman, 2002]: dust, with an atmospheric injection rate determined by wind plus soil type and moisture; oceanic, composed of evaporated sea brine drops produced by wave/wind action; biomass burning or smoke, produced either by random events such as lightning or by deliberate agricultural burns; ambient continental aerosol with a high organic content due to pollen and other vegetative emission; and anthropogenic/industrial, composed of a mixture of sulfates and soot, though Omar et al [2005] has shown that the anthropogenic component currently divides into two clusters depending on the soot content. Of these, smoke is the most variable and difficult to forecast, so is included in aerosol transport models as an observed input rather than predicted from sources [Chin et al, 2004]. These classifications have always been made on a phenomenological basis, but it was not until the advent of the AERONET system [Holben et al, 1998] and comprehensive almucantar retrieval algorithms [Dubovik et al, 2002] that a long-term, self-consistent set of global measurements were available to produce classification based on optical properties alone [Levy 2007; Omar, 2005; Dubovik, 2002]. These measurements have demonstrated that the sulfate and smoke components tend to increase in size with aerosol optical depth. For sulfates this tends to be a humidification effect [Jeong et al, 2007], but for smoke in the boreal forests this may be due more to aggregation [O'Neill, 2002, 2005; Colarco, 2004].

Calculation of aerosol radiative effects (forcing) requires an aerosol optical model.

The test of such a model is often referred to as *column closure*, in which radiant observations in several directions - typically at the top of the column looking down and those at the bottom looking up - agree with calculated model output for multiple wavelengths [Russel et al, 1999b; Fieberg et al, 2002; Bundke et al, 2002; Procopio et al, 2003]. Since it is rare for a single instrument to measure radiances in several directions as well as particle properties (AERONET comes close, as in Procopio et al [2003, 2004]), a related issue is consistency between instruments [Haywood et al, 2003; Vant-Hull et al, 2004]. Field campaigns typically generate enough measurements so that column closure tests are interesting. A review of the consistency obtained in recent campaigns will serve as a guide to how the field has evolved. Only those campaigns pertaining to the current study will be discussed.

The Smoke, Clouds, and Radiation in Brazil (SCAR-B) experiment of 1995 hosted one of the largest aerosol measurement instrument deployments to date [Kaufman et al, 1998]. A number of AERONET stations were deployed, MODIS and HIRS simulators were flown on aircraft, as well as a full set of in situ aerosol measurement instruments. The closure tests consisted of flying the aircraft in a pattern above sun photometers, so that horizontal legs were averaged, with successive horizontal legs integrated vertically. A particle counter binned the aerosol by size, while scattering was measured by nephalometer and absorption by an integrating filter or PSAP (see appendix C). Humidification factors were accounted for by periodic comparison of outer to interior sample measurements.

The integrated sum of in situ absorption and scattering generally yielded optical

depths about 20% lower than measured by sun photometer. This was attributed to the upper part of the atmospheric column not measured by aircraft. Backscatter coefficients calculated from the measured size distributions were 10-15% lower/greater than the measured values depending on the wavelength. Calculations based on AERONET retrievals showed similar behavior. An early almucantar retrieval was used that requires the complex index of refraction and does not account for multiple scattering [Nakajima et al, 1996]. Based on the in situ size measurements, a model was constructed of smoke as spheres with a solid carbon core surrounded by non absorbing material. The forward calculated scattering and absorbing coefficients were within 25% of the measurements. No attempt was made to compare the flux calculations based on this model to measurements.

The Tropospheric Aerosol and Radiation Forcing experiment (TARFOX [Russel et al, 1999B]) was conducted off the American Mid Atlantic Coast in 1997, using aircraft in situ and sunphotometer measurements. During TARFOX the chemical composition of the aerosol was combined with size distributions measured in situ to create an optical model tested by onboard sun photometers [Francis et al, 1999]. In 2 of 3 cases the agreement was good, requiring perturbations of the size distribution within the instrumental error to obtain a match to the observed radiances.

The Lindenburg Aerosol and Cloud Experiment (LACE) studied a smoke plume transported from Canada. As in TARFOX, chemical composition was combined with in situ size distributions, but a 3 mode lognormal distribution was assumed, oblate spheroids were assumed based on polarization, and lidar measurements fixed the layer locations

and optical depths. Measurements by sunphotometer showed optical depth closure to within 25% [Fieberg et al, 2002].

Based on this history, in situ measurements may never agree with remote sensing retrievals to high accuracy. The choice of which to use may depend solely on the need for vertical profile information.

Since the advent of comprehensive optical property retrieval by AERONET and the launch of the A-Train satellite system, there have been no extensive field campaigns designed specifically to study smoke (SAFARI 2000 was on the cusp, and did not use these instruments). The 2002 SMOCC campaign in Amazonia [Andreae et al, 2004] consisted of a single instrumented aircraft in combination with MODIS aerosol measurements. As this was mainly a cloud measurement experiment, it will be discussed in the next section.

The new style of 'campaign' uses primarily remote sensing, as typified by the aerosol forcing experiments of Procopio et al [2003, 2004], in which a dynamic aerosol model with properties that changes with optical depth was constructed purely from AERONET retrievals. Broadband forcings were calculated, then validated by a set of narrow band measurements made by AERONET in several locations as well as by MODIS satellite overpass. In the future for vertical profiling of optical properties, multi-wavelength LIDAR may serve the same purpose as in situ aircraft measurements [Rajeev and Parameswaran, 1998].

1.2.2 Recent Studies of Aerosol Effects on Clouds

The strongest effect aerosols have on clouds is through the role of CCN. When water vapor is divided among more condensation nuclei the resulting drop size must decrease [Twomey, 1977]. Though aerosol may be related to or even affect the water supply [Han, 2000; Ackerman, 1995], the bulk of experimental observation bears out the general decrease of drop size with aerosol loading [Rosenfeld and Lensky, 1997; Koren and Kaufman, 2005, Feingold et al, 2002]. The decrease in drop size limits coalescence and precipitation, thus increasing the cloud lifetime [Haywood and Boucher, 2000].

The purest study of aerosol effects on clouds was conducted during the Monterrey Area Ship Track (MAST) experiment [Durkee et al, 2000]. Smoke stacks from ships inject aerosol into pre-existing stratus clouds, so that the environmental parameters inside and outside each plume were constant, and the clouds were nearly plane-parallel. Not only were meteorological and aerosol measurement instruments mounted on the ships, but instrumented aircraft flights were scheduled and the known ship locations could be matched to satellite overpasses. Though there were no qualitative surprises, the high quality of the measurements obtained were useful as numerical tests of models of droplet formation and drizzle suppression [Ferek et al, 2000].

A key feature of cumulus clouds is the vertical development of drop size, so that clouds must be compared in equal stages of growth. Daniel Rosenfeld and Itimar Lensky [1997, 1998] developed a scheme to map out the cloud cycle by using the spectrum of cloud top heights in a single scene as measured by satellite. They were able to show that in areas of increased aerosol loading the drop size is decreased throughout the cloud

column. This approach depends on scenes small enough that the cloud base can be assumed to be the same throughout the ensemble, a requirement that limits the sample size to the level of case studies. Chang and Li [2002] showed how to retrieve profile information on a pixel basis using multispectral information, used by Chen et al [2007] to estimate precipitation probabilities on a per pixel basis.

As turbulent objects, cumulus clouds have large intrinsic variability, so large scale statistical studies are necessary to separate signal from noise. The need for large data volume favors satellite data sets. Such studies concerning smoke have to this date been conducted exclusively in Amazonia, under the assumption that cloud base is fairly constant. Kaufman and Fraser first applied the large scale statistical method in Amazonia to show that the slope of cloud drop effective radius as a function of aerosol optical depth(AOD) may change with water vapor. Feingold et al [2002] used a more complete data set to indicate that the change of slope may be due to saturation with AOD rather than the effects of water vapor. To support this claim they offered a theoretical model of competition between droplets for water vapor that caused saturation in droplet formation as the number of droplets increased.

Many large-scale studies are of interest even if they do not relate exclusively to smoke. Working on a global scale, Han et al [2002] demonstrated that the correlation of cloud liquid water (CLW) with AOD could be positive or negative, depending on the meteorological region. The increase of CLW with AOD is predicted by drizzle suppression, but a decrease often occurs over land where the droplet sizes are smaller and evaporation at the base of the cloud may affect the dynamics. This observation is

corroborated by aircraft penetrations that often do see this same relationship [Brenguier, 2005].

Working over the Atlantic, Kaufman et al [2005] showed by multivariate analysis that shallow cloud fraction increased with and is directly affected by AOD for all aerosol types, in agreement with the drizzle suppression mechanism seen in the MAST experiment. Also over the Atlantic with the same techniques, Koren et al [2004] discovered that an increase in aerosol often resulted in increased cloud heights. This was attributed to the delayed onset of precipitation, allowing the clouds to develop higher. This behavior was confirmed by aircraft penetrations of the coast of Amazonia, in which not only were the clouds seen to develop higher in the presence of smoke, but the eventual precipitation was more dynamic since it occurred in the ice phase rather than the water phase [Andreae et al, 2004].

Direct measurements of CCN activity are relevant to the aerosol effect on clouds. Novakov et al [1996] demonstrated in laboratory experiments that smoke from burning cellulose can act as CCN. Roberts et al [2002] performed a detailed chemical and CCN activity analysis on wet season aerosol in Brazil, presumably the background aerosol during the burning season. He found that sulfates, which made up 15% of the aerosol by mass, accounted for 80% of the CCN spectra. This analysis depends heavily on droplet activation or Kohler theory, which was tested empirically by Conant et al [2004]. Measurements of the aerosol properties directly below a cloud were used to model the CCN spectrum, which agreed with the actual drop distribution found at the bottom of the cloud to within 25%. Unfortunately there have been no experiments to test the

competition between sulfate and smoke particles as condensation nuclei, a situation important to this study.

The direct radiative effect of aerosols can affect the atmosphere in ways that influence cloud development. Aerosols shade the surface, decreasing the heated layer that can feed convection. Absorbing aerosol can heat the upper atmosphere, and the combination of the two effects can result in a lower lapse rate and a more stable atmospheric column [Taubman et al, 2004], reducing the thermal height and cloud development. This shading can also reduce transpiration, a major source of water vapor over forested regions [Koren et al, 2004]. Koren and Kaufman [2006] used AERONET cloud screening data to related AOD and cloud fraction (CF) as a function of aerosol absorption. The showed that the slope between AOD and CF was positive for non absorbing aerosol, then decreased and became negative as the aerosol absorption increased. Though this may be theoretically attractive, the study has been questioned based on the use of data that is not quality assured: the almucantar retrievals used to derive aerosol absorption are generally not valid if there is a significant cloud fraction [Eck, 2006].

1.3 Three-Dimensional Effects

Unless stratiform clouds are under study, the experimental situation is inherently three-dimensional (3D). All operational satellite retrievals are based on plane-parallel geometry. Typically researchers have dealt with the issue by using center pixels and

restricted satellite geometry, then assuming large averages will resolve the issue [Kaufman and Fraser, 1997; Feingold et al, 2002]. Yet Vant-Hull et al [2006] and Wen et al [2006] demonstrated that 3D effects for cloud drop effective radius and AOD, respectively were systematic and could not be eliminated by averaging. No study of cloud/aerosol interactions has yet been published that fully accounts for these biases.

1.4 Conclusions: the Direction Forward

The studies presented above exhibit two significant gaps:

1. There is no large-scale statistical study of smoke/cloud interactions in the temperate zones.
2. The large scale studies that have been done are typically performed using 1 degree averages, severely limiting quality control on the cloud scale.

As argued in chapter 4, the first statement will lead us to Canada and Siberia, where the forests are large and fires are often allowed to develop unchecked.

The second point requires a more subtle response, eventually leading to the selection of cumulus clouds over stratus as the focus of study. Though high-resolution cloud data may make it easier to select cloudy pixels that conform to the plane parallel criterion of the satellite retrievals, the end result would be stratiform clouds that extend over hundreds of km size pixels. But since aerosol retrievals are excluded from cloudy pixels, this would eliminate valuable local aerosol information. The alternative is to use

the high resolution cloud data to select subsets of clouds that are geometrically similar, and open enough to allow local retrieval of aerosol. For 1 km resolution, this matches the description of fair weather cumulus. Cumulus clouds cannot satisfy the plane-parallel ideal. But if subsets of geometrically similar clouds are compared, the biases should be similar as well, and the comparison remains valid.

Clouds are only half the aerosol/cloud system. The optical properties of aerosols are a result of the physical properties, which in turn determine the efficiency as cloud condensation nuclei. Chapter 2 explores smoke optical properties and direct radiative forcing based on measurements made on a plume created by Canadian forest fires. A number of calculations are made based directly on in situ measurements made by aircraft. The addition of other measurement instruments allows these calculations to be extended not only across the solar spectrum, but across the entire region once a full aerosol model is created around which satellite retrievals can be built. These retrievals are compared to a series of surface and space based observations.

Studies of aerosol effects on clouds are only as good as the cloud and aerosol retrievals themselves. Chapter 3 explores the effects the three dimensional nature of clouds has on retrievals built on 1-dimensional theory. From this a mitigation strategy is formed to study cloud-aerosol interactions despite otherwise intractable retrieval biases. It should be noted that since aerosols can only be studied in clear air, side-by-side retrievals of cloud and aerosol properties require scattered or broken cloud fields, which are manifestly three-dimensional.

The final chapter presents what is believed to be the first study of cloud-aerosol interactions that explicitly accounts for 3D biases. The result is a comparison of cloud microstructure in Siberia and Canada, for which the aerosol composition is shown to vary

while other environmental variables are held constant. The microphysical differences are explained by a simple model of aerosol and cloud condensation nuclei loosely based on the measurements made in Chapter 2, bringing the set of experiments full circle.

Chapter 2: Optical Properties and Radiative Effects of a Canadian Forest Fire Smoke Plume over the U.S. Mid Atlantic Region

2.1 Introduction

For aerosol studies satellite retrievals are the most useful data set for climate studies because of their spatial and temporal coverage [Kaufman *et al*, 2002]. These retrievals generally require prior knowledge of optical properties for the aerosol being retrieved [King *et al*, 1999]. This poses a special difficulty for remote sensing of biomass burning aerosols whose optical properties vary widely depending on vegetation type, burning mode (smoldering or flaming), and age [Kaufman *et al*, 1998; Reid *et al*, 1999; Wong and Li 2002]. The single scattering albedo, ω_o, is one optical characteristic often used to distinguish smoke from other background aerosol. The SCAR-B experiment [Kaufman *et al*, 1998] in Brazil measured single scattering albedos as low as 0.6 (0.55 micron wavelength) in fresh smoke [Reid *et al*, 1998B], increasing up to 0.91 as the smoke aged, associated with the growth of the particles as the liquid content increased. Measurements of Canadian smoke during the BOREAS experiment found ω_o ranging from 0.70 for fresh smoke to 0.98 for aged smoke [Miller and O'Neill, 1997; Li and Kou, 1998]. Laboratory measurements of smoke emitted from pine needles from these trees show that ω_o for fresh smoke can range from 0.66 to 0.97 depending on whether the fire is in the flaming or smoldering phase [Miller and O'Neill, 1997]. Smoke may also evolve chemically during transport by

mixing with other emissions [Kreidenweis *et al*, 2001].

This variability makes it impossible to evaluate the reliability of a single measurement or instrument, so field campaigns allow inter-comparison between many instruments and measurement scenarios. In many previous field campaigns, a subset of aerosol optical properties (size distribution, phase function, optical depth) were retrieved from sun photometers using algorithms that required fixed values for the remaining properties (complex index of refraction or single scattering albedo) [Kaufman *et al* 1998; Russel *et al*, 1999B], while recent studies employ a more advanced and comprehensive algorithm proposed by Dubovik *et al* [2000] for sun photometer retrievals [Dubovik *et al*., 2002]. Likewise, the absorption measurements using the PSAP (particle soot absorption photometer) instrument before 1999 could not take advantage of the Bond calibration [1999]. In both the SCAR-B and INDOEX experiments, ω_o measured in situ by aircraft was 2 to 3 percent lower than that measured remotely by sun photometer [Dubovik *et al*, 2002; Ramanathan *et al*, 2001b]. Though these differences are within instrumental error, the preponderance of lower values measured in situ versus sun photometer suggests a true experimental difference. By contrast, much closer agreements were found between in situ and surface radiometer values of ω_o for aerosols dominated by biomass burning obtained during the SAFARI campaign [Haywood *et al*, 2003, Magi *et al*, 2003]. Other campaigns such as LACE-98 [Bundke *et al*, 2002] achieved consistency between measurement techniques by introducing a free parameter in the form of a variable liquid layer coating the carbonaceous core of aged smoke. This chapter represents

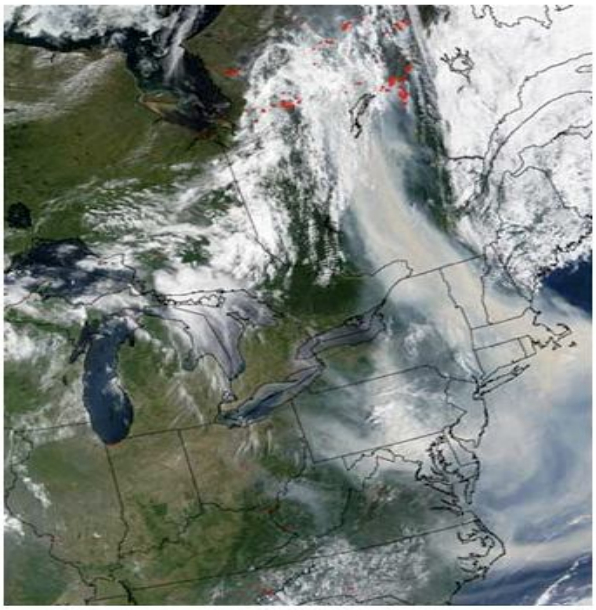

Figure 2.1: Seawifs image of the smoke plume on July 8.

another comparison between instruments for the case of a smoke plume.

In early July of 2002, forest fires in Quebec gave rise to a thick smoke plume that flowed south to blanket the Northeastern and Mid-Atlantic seaboard of the U.S., as shown in the satellite imagery of Figure 2.1. The smoke was able to travel this distance without being dispersed by mixing because it stayed above the convective boundary layer, as demonstrated by micro-pulse LIDAR (MPL) aerosol mass retrievals from NASA Goddard [Colarco, 2003] shown in Figure 2.2. On July 6 the smoke plume is clearly above the convective boundary layer (CBL), but on the night of the 7th merges with it, and the though it maintains a separate identity at the top of the CBL throughout the following day, the aerosol load beneath it has increased, presumably by convective mixing.

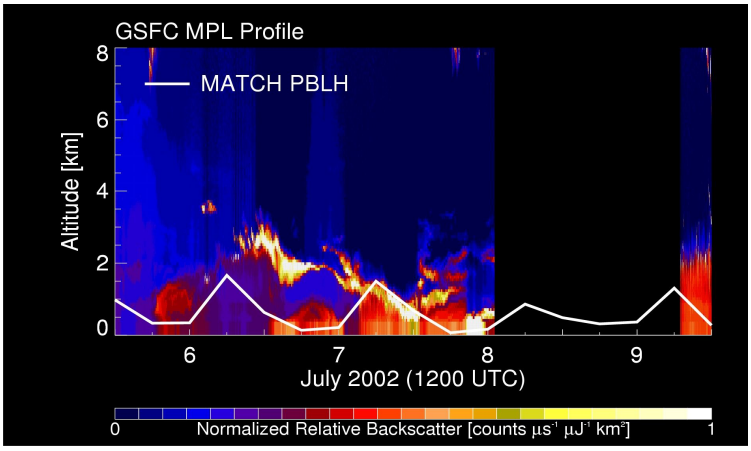

Figure 2.2: micropulse lidar imagery at GSFC.

On July 8 a small research aircraft operated by the University of Maryland and equipped with meteorological sensors, trace gas detectors, and aerosol optical property measurement instruments flew five ground-to-ceiling spirals in the Maryland/Virginia area, as shown in figure 2.3. These observations confirmed that the smoke was confined to a layer with a lower altitude of 2 km MSL. The measurements were used to characterize the optical properties and radiative effects of the plume throughout the surrounding region. The first half of this chapter describes the data set as collected by Lackson Marufu and analyzed by Brett Taubman, followed by the radiative transfer calculations I did at his initiation [Taubman *et al*, 2003]. The second half of this chapter consists of the extension of the original point location calculations to the entire area using satellite retrievals I devised for this purpose. These retrievals were compared to AERONET, SURFRAD, and CERES measurements to evaluate the consistency between different retrieval and measurement methods [Vant-Hull *et al*, 2004].

The chapter begins with a section on meteorology and transport (section 2.2), followed by a description of the flight and measurement instruments (2.3). The basic optical property data is presented in section 2.4, followed by the calculations used to arrive at a full physical/optical model of the smoke aerosol (2.5). This optical model is extrapolated across the solar spectrum in section 2.6, then used in section 2.7 to calculate the radiative forcing and heating rates at each location. In section 2.8 several regionally averaged optical models are presented, based either on the in situ aircraft measurements or on

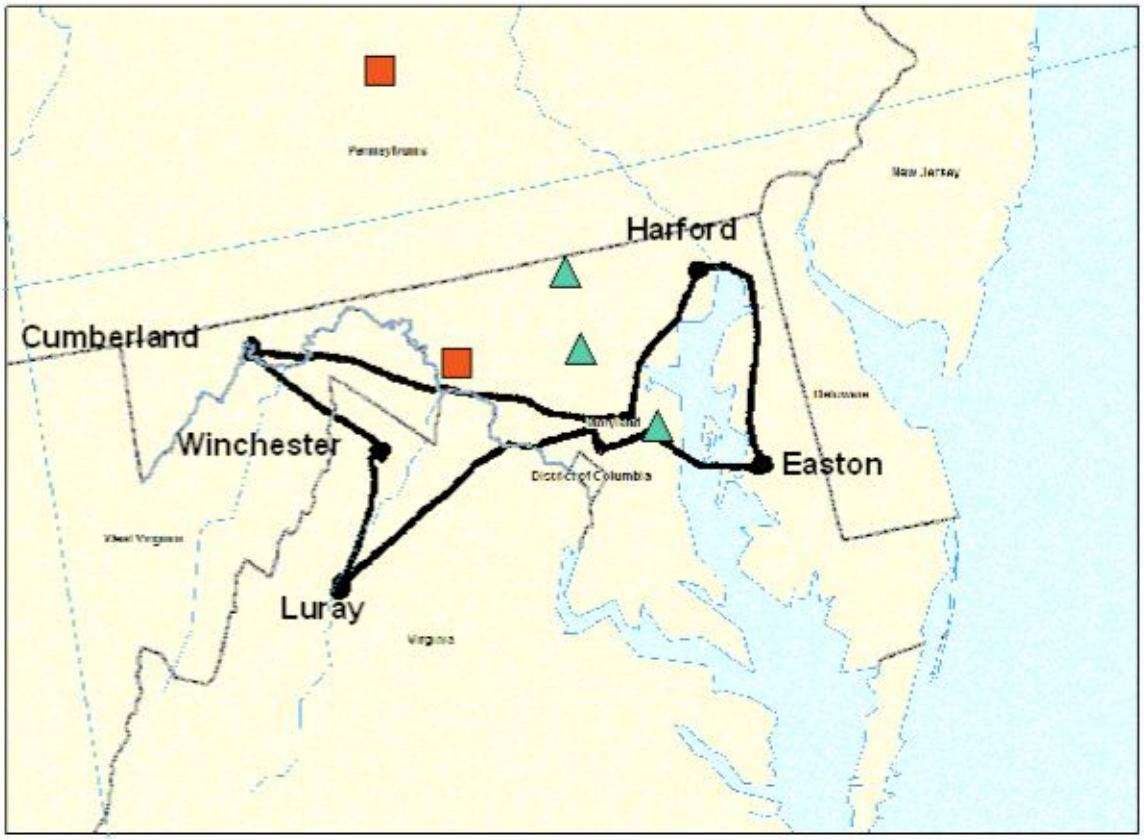

Figure 2.3: Aircraft flight pattern on July 8. AERONET sites are shown as green triangles, SurfRad/ISIS sites as red squares.

AERONET retrievals; and these models are compared (section 2.9). In section 2.10 area-wide calculations of radiative forcing from satellite retrievals are presented and compared to measurements. An uncertainty analysis follows for the aerosol optical depths (section 2.11) and the radiative forcings (section 2.12). The implications of the retrieval comparisons for satellite retrievals of aerosol radiative forcing is discussed in section 2.13, and the chapter ends with a summary.

2.2 Meteorology and Transport

From July 5 through July 7 the broad features of the pressure system from eastern Canada down the mid Atlantic coast remained stable: a cutoff low over Maine with a broad high-pressure system over the central U.S. (Figure 2.4a). Smoke from the Quebec fires were funneled south around the west of the low, then along the coast by the high, where a region of difluence caused the plume to fan out over the Maryland area by July 8 as shown in the 500 mb analysis of Fig. 2.4b. By July 9 the low-pressure system moved eastward, so that the winds along the mid Atlantic coast shifted to blow the plume offshore.

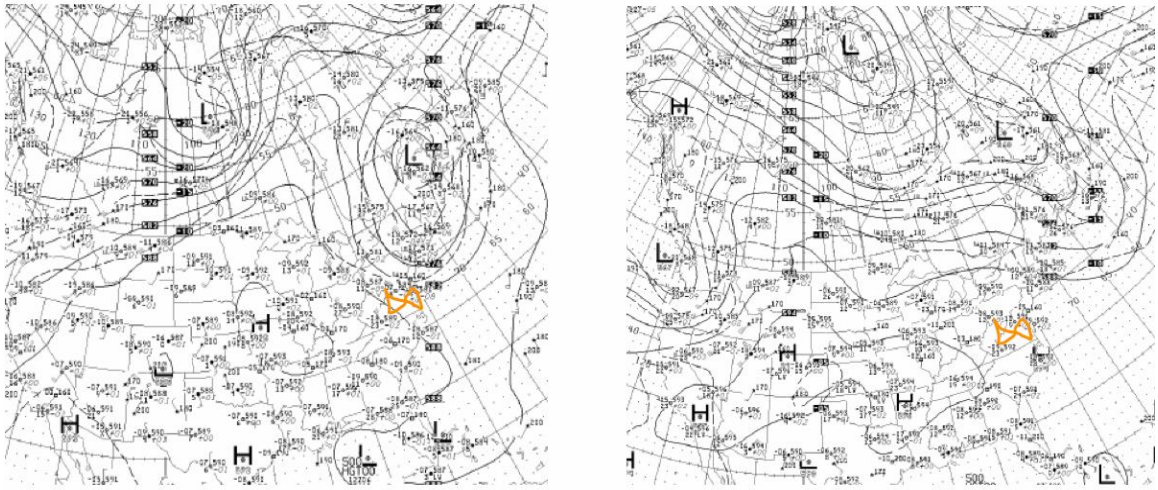

Figure 2.4: NCEP 500 mb height analysis for 12:00 UTC on July 6 (left) and July 8 (right). The flight location is shown in orange.

For each of the five measurement locations, 72-hour back trajectory analyses were performed using the NOAA Air Resources Laboratory (ARL) HYbrid Single-Particle Lagrangian Integrated Trajectory (HYSPLIT) model (Version 4) [Draxler and Rolph, 2003]. Since the smoke was largely confined to a layer above 2 km MSL, the

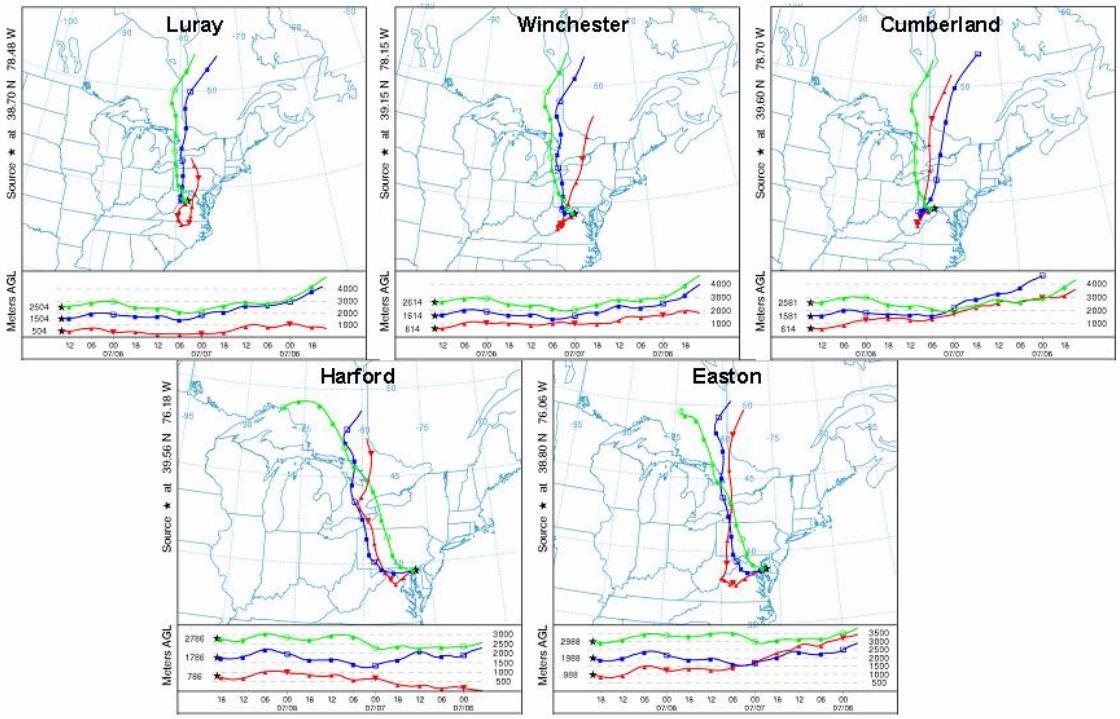

Figure 2.5: 72-hour back trajectories for the 5 spiral locations calculated by the NOAA ARL HYSPLIT EDAS model with initial altitudes of 1000, 2000 and 3000 m MSL.

calculations were performed for injection levels of 1000, 2000 and 3000 meters MSL as shown in Figure 2.5. For all locations the two upper level trajectories originate in Quebec, while the 1000 m trajectories are variable for the morning locations of Luray and Winchester. This fits with the idea of lower level PBL layer aerosols as likely to be local in origin.

2.3 Instrument Platform and Flight Pattern

The instruments are mounted on a small plane with a ceiling of 3000 meters MSL.

A forward inlet feeds the aerosol measurement instruments; an aft facing inlet feeds the trace gas instruments, with a meteorological probe in between. Position was measured using a Garmin-90 GPS with 10-second resolution. Temperature and relative humidity (RH) were measured using a thermistor and capacitive thin film packaged in a Rustrak RR2-252 RH probe, with precisions of 0.5^{o} C and 2% RH and a 30 second response time. Pressure was measured using a Rosemount model 2008 pressure transducer with 5 mb precision. Throughout this chapter aircraft altitudes are calculated by conversion from pressure with reference to the U.S. standard atmosphere. This conversion is adjusted for ambient surface pressure averaged for takeoff and landing locations, calibrated to known surface elevations.

Optical scattering by aerosol was measured by a TSI 3563 integrating nephalometer at wavelengths of 450, 550, and 700 nm [Anderson *et al*, 1996], with an averaging time of 5 minutes. Corrections were made to account for the fact that neither the detectors nor the scattering pattern were arranged uniformly on a sphere. This is done by assuming a wavelength dependant correction factor linearly scaled to the measured Ångstrom exponent, as calibrated to standard particles [Anderson and Ogren, 1998]. The estimated uncertainty of the instrument after corrections is 10%.

Aerosol light absorption at 565 nm was measured using a Radiance Research Particle/Soot Absorption Photometer (PSAP). Aerosol was deposited on the filter at a continuous rate while the transmitted intensity was recorded [Anderson *et al*, 1999]. The change in absorption per volume of air represents the aerosol absorption. Minute averages were used to calculate the changes in absorption. The transmitted light must be

adjusted for scattering as measured by nephalometers in order to obtain the absorptive component [Bond *et al*, 1999]. Given accurate corrections for flow rate, spot size, etc the estimated instrument uncertainty is 20%.

A Met-One Model 9012 optical particle counter measured size distributions for 6 preset size bins from 0.15 to 0.50 μm particle radii. Inlet losses varied with particle size, so for radiation transfer calculations this size distribution was rejected in favor of parameters calculated from scattering values, as described in section 2.5.

Trace gasses were also measured, but as only the qualitative value as markers for the type of aerosol are of interest, the instrumentation will not be discussed in detail.

The aircraft performed 5 spirals over the locations shown in Figure 2.3, extending from ~5 m above the ground to the 3 km MSL ceiling, at a vertical climb rate of approximately 100 meters/minute. The coordinates and times of each spiral are summarized in Table 2.1. The first 3 were in the morning, the last two in the afternoon.

Location	latitude	longitude	time
Luray, VA	38.7 N	78.5 W	13 Z
Winchester, VA	39.2 N	78.2 W	14 Z
Cumberland, MD	39.6 N	78.7 W	15 Z
Harford, MD	39.6 N	76.2 W	19 Z
Easton, MD	38.8 N	76.1 W	20 Z

Table 2.1: Locations and times of measurement spirals on July 8, 2002.

2.4 Results: Basic Aerosol Properties

2.4.1 In Situ Measurements

All results will be presented as vertical profiles at each of the five locations. Figure 2.6 shows temperature and RH. At 2 km MSL a temperature inversion accompanied by a drop in RH is present for all locations. This is consistent with subsidence from the regional high pressure on this day. The low-level morning inversion

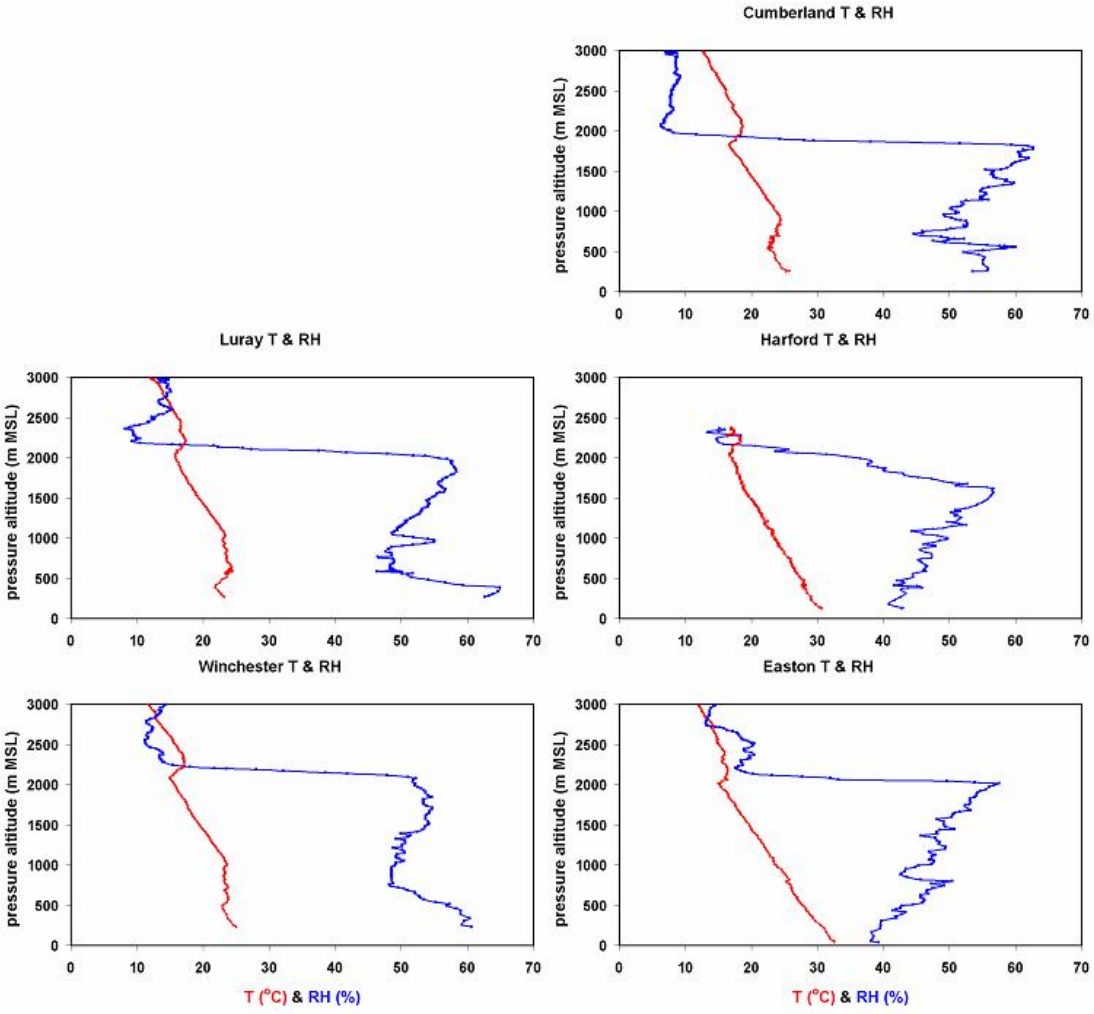

Figure 2.6: Temperature and relative humidity profiles measured at each spiral location.

has dissipated by the afternoon flights over Harford and Easton. A large jump in particle number concentration with diameters between 0.4 and 1.0 microns is seen at all locations except Cumberland, suggesting the smoke plume is sequestered above this inversion (Fig. 2.7). The hypothesis that the presence of absorbing smoke could strengthen this inversion will be investigated in relation to calculations of the radiative properties of the smoke.

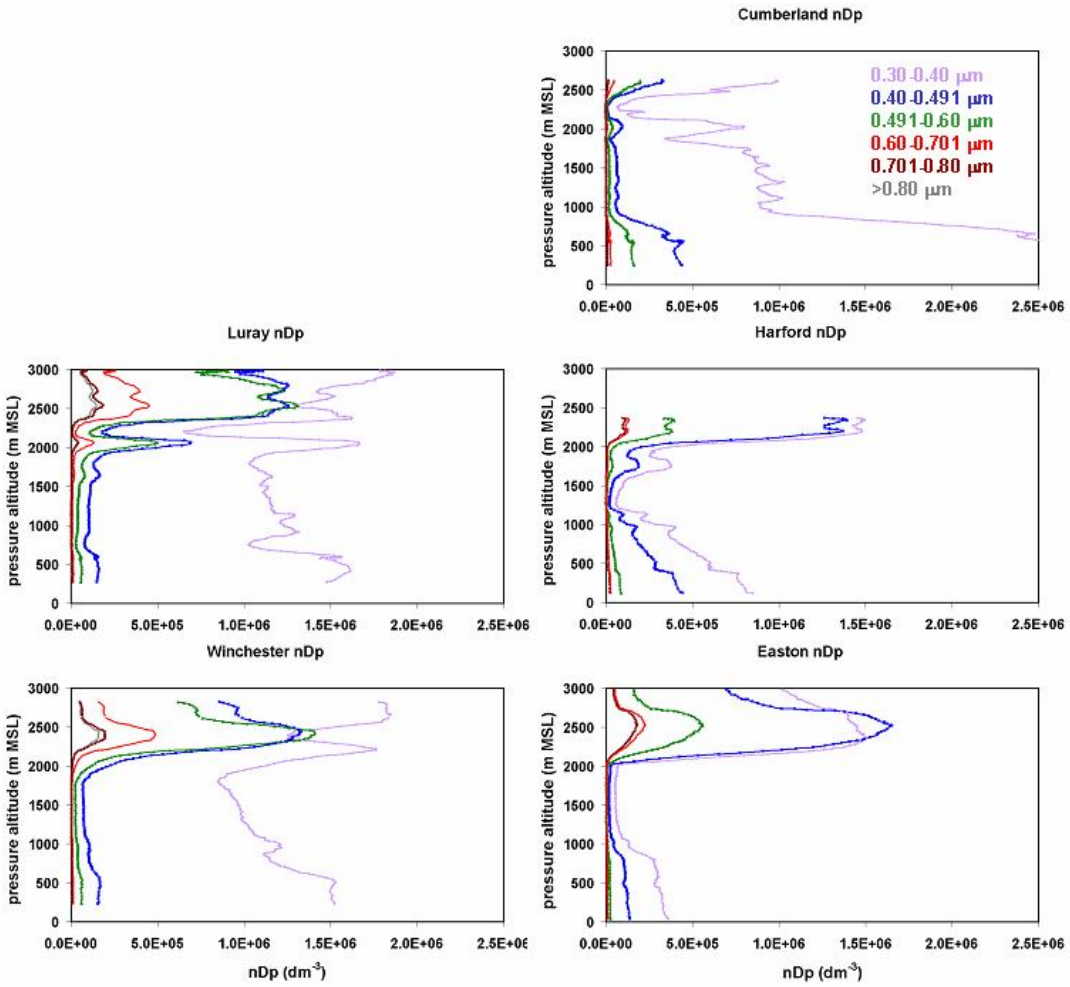

Figure 2.7: Size distributions from the MET-One optical particle counter. The bins are given in diameters.

It is interesting to note that in the western locations of Cumberland, Luray and Winchester the smallest size bin shows much larger increases near the ground than the eastern locations (Fig. 2.7). A clue to this behavior may be found in the trace gas measurements. At all sites except Cumberland a peak in ozone and carbon monoxide occurs above 2 km MSL, consistent with the indication of smoke from the particle counts at these locations [McKeen *et al*, 2002; Crutzen *et al*, 1979; Stith *et al*, 1981]. The low level SO_2 concentration is much higher in Harford, Cumberland and Easton than in Luray and Winchester. Taubman *et al* [2004] speculated that the absence of smoke in Cumberland allowed greater photo-oxidation of SO_2 into aerosolized SO_4, thus leading to the highest low level small particle count among all the regions. But this does not explain the increased low altitude particle density in the other western sites. Vant-Hull *et al* [2005] suggested that the Cumberland low-altitude plume might be due to a coal burning power plant upwind of the site. If this is the case, it may explain the similar plumes at Winchester and Luray, south of Cumberland.

The nephalometers heat the air, resulting in an instrument RH of $\lesssim$ 20%. To correct the scattering coefficient σ_s back to ambient conditions the empirical equation is applied:

$$\frac{\sigma_s(RH_{amb})}{\sigma_s(RH_{ref})} \equiv F(RH) = \left(\frac{1-RH_{amb}}{1-RH_{ref}}\right)^{-\gamma} \qquad (2.1)$$

Where 'ref' refers to the reference humidity inside the nephalometer [Anderson *et al*, 2003]. The parameter γ was set to 0.35 as per Remer *et al* [1997] due to similarities in

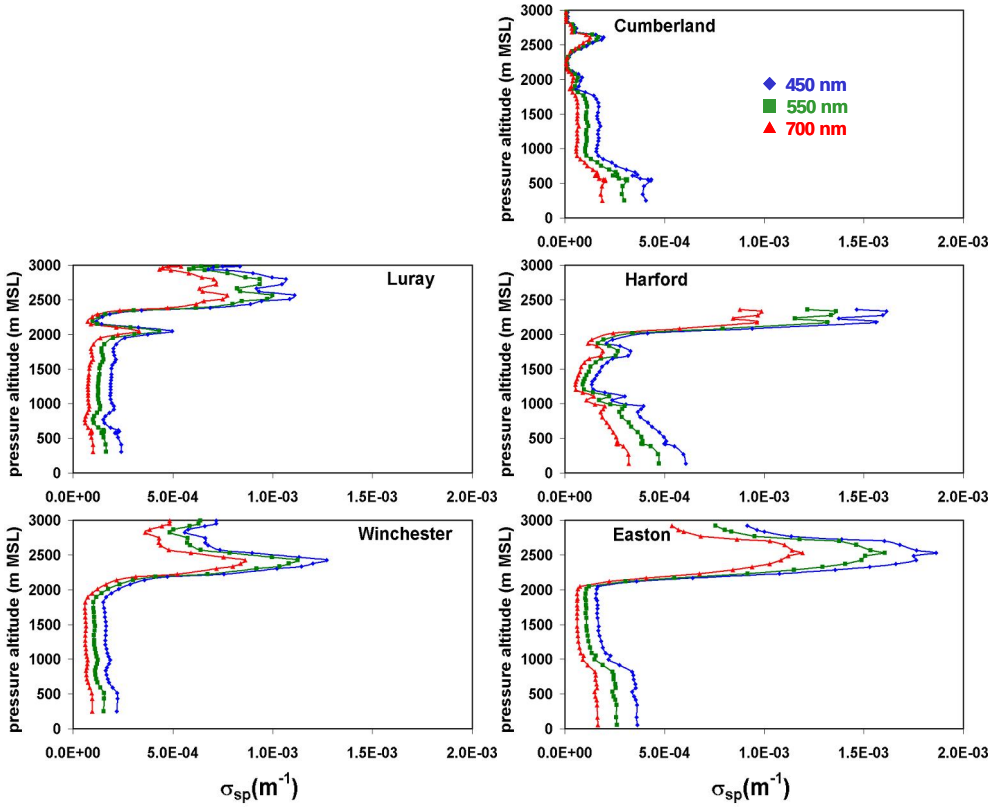

Figure 2.8: Scattering cross section profiles measured by nephalometer.

the region and instrument. This equation does not account for different aerosol responses to humidification. A correction linear in the Ångstrom exponents calculated from the nephalometer data was used to adjust scattering for the particle size at the measurement wavelength [Anderson and Ogren, 1998].

The vertical scattering profiles of Figure 2.8 once again indicate an aerosol plume above 2 km for all locations except Cumberland. The variation of scattering with wavelength indicates the particle size distribution, and can be used to further distinguish the upper level plume from the ambient aerosol below it. Vertical profiles of the scattering Ångstrom exponent α in Figure 2.9 exhibit generally smaller exponents above

2 km. This indicates smoke particles that are larger than the ambient aerosol below, as may be expected since the smoke has aged during its roughly 1000 km trip from the source region [Reid and Hobbes, 1998]. The values for smoke lie within the extremes seen for other high optical depth smoke plumes [Eck et al, 2003].

Layer averages of the Ångstrom exponents based on aircraft measurements for each site appear in Table 2.2, along with single scattering albedo and aerosol optical depth (AOD) as discussed in section 2.5. AOD was used as a weighting factor to calculate the averages at the bottom of the chart.

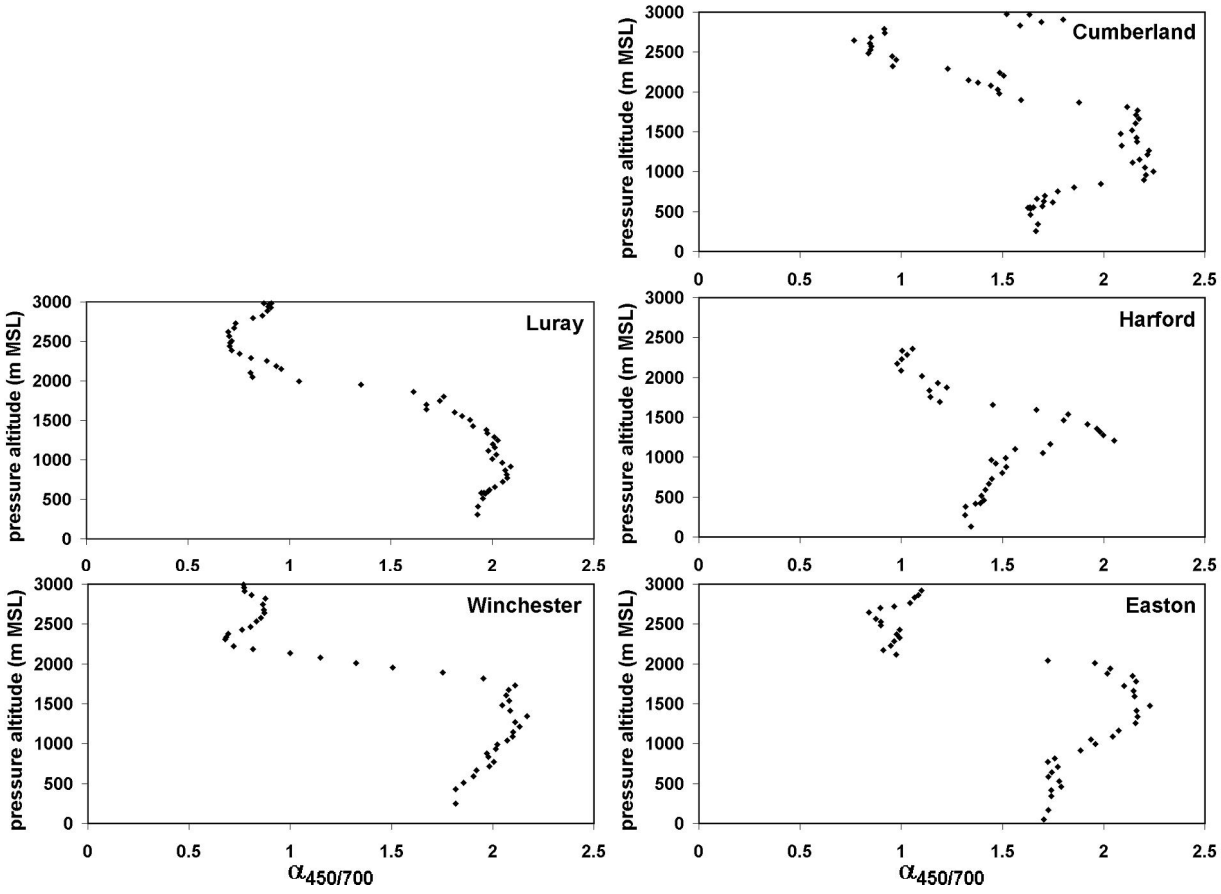

Figure 2.9: Ångstrom exponent profiles calculated from the scattering cross sections of Fig. 2.8.

		τ_{550}	ω_o 550 nm	$\alpha_{450/550}$	$\alpha_{550/700}$
Luray	Smoke	0.74 ± *.11*	0.91 ± *.02*	0.57 ± *.18*	1.04 ± *.11*
	PBL	0.29 ± *.05*	0.95 ± *.01*	1.84 ± *.42*	1.99 ± *.34*
Winchester	Smoke	0.75 ± *.11*	0.94 ± *.01*	0.60 ± *.44*	1.05 ± *.22*
	PBL	0.23 ± *.03*	0.95 ± *.01*	1.90 ± *.34*	2.06 ± *.30*
Cumberland	Smoke	0.08 ± *.01*	0.86 ± *.03*	1.17 ± *.64*	1.29 ± *.30*
	PBL	0.34 ± *.05*	0.94 ± *.01*	1.85 ± *.26*	2.05 ± *.21*
Harford	Smoke	0.55 ± *.08*	0.93 ± *.01*	0.87 ± *.10*	1.26 ± *.09*
	PBL	0.51 ± *.08*	0.94 ± *.01*	1.45 ± *.33*	1.70 ± *.29*
Easton	Smoke	1.18 ± *.18*	0.93 ± *.01*	0.71 ± *.10*	1.18 ± *.09*
	PBL	0.35 ± *.05*	0.96 ± *.01*	1.83 ± *.19*	2.03 ± *.16*
Average	Smoke	NA	**0.93** ± .02	**0.69** ± .11	**1.14** ± .09
	PBL	**0.34** ± .10	**0.95** ± .01	**1.76** ± .31	**1.96** ± .30

Table 2.2: Averaged optical properties for the smoke and PBL layer at each spiral location. The optical depth values represent the measured portion of the plume only.

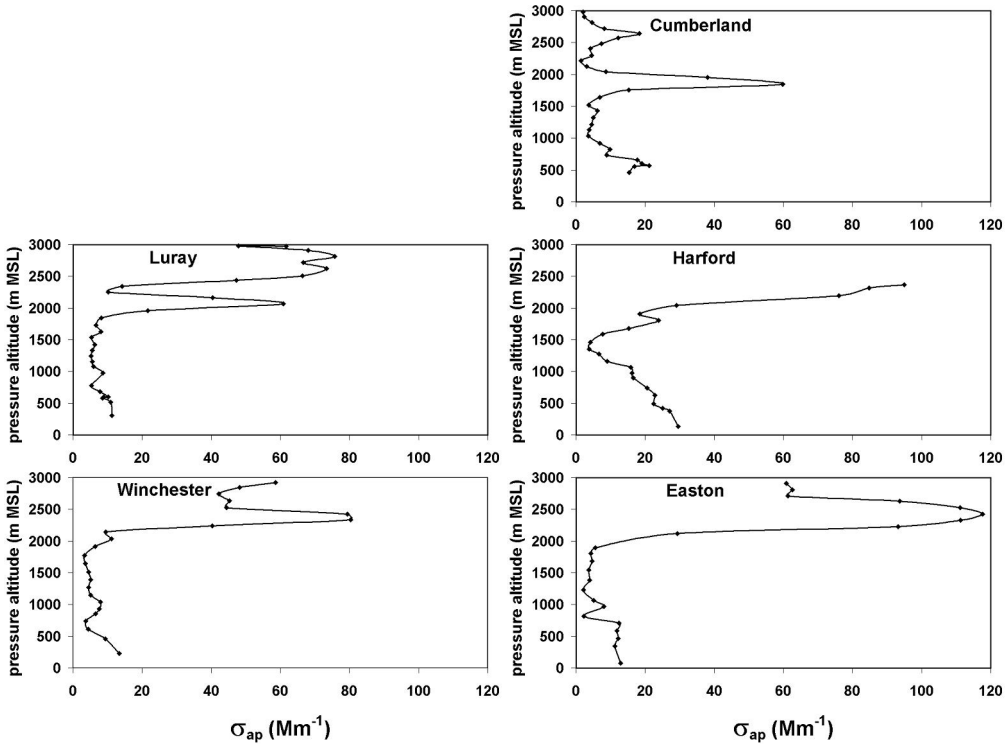

Figure 2.10: Absorption profiles measured by the PSAP instrument.

The characteristic that most distinguishes smoke from the ambient aerosol is its light absorption. The PSAP instrument must be adjusted for scattering (measured by the nephalometers) in order to calculate the drop in transmittance due to absorption alone [Bond *et al*, 1999]. The absorption was adjusted from the value at 565 nm to 550 nm assuming a damped harmonic oscillator model so that $\sigma_a \propto 1/\lambda$ [Bodhaine, 1995]. The results appear in Figure 2.10, showing strong absorption above 2 km for all the sites, with Cumberland showing a weaker but still very apparent peak.

2.4.2 Aeronet Retrievals

There are three AERONET sites in the region loosely defined by the aircraft flights, shown by the triangles of Fig. 2.3. The Goddard Space Flight Center (GSFC) site is located at the edge of the greater DC metropolitan area. Quality assured retrievals of optical depth fluctuated between 1.3 and 2.2 throughout the day of the aircraft measurements, indicating the influence of smoke for the entire day. Optical depths as high as ~7 could be inferred for later in the day at this and other sites, though low radiances degraded the quality of the retrievals and so these higher values were not publicly distributed [Eck *et al*, 2003]. The SERC site is on a sparsely inhabited peninsula protruding into the Chesapeake Bay, and also showed high optical depths throughout the day but with smaller variability (between 1.8 and 2.2). The Maryland Science Center (MDSC) site is located in downtown Baltimore next to the harbor and showed generally lower optical depths between 1.3 and 1.8.

Throughout the day the smoke layer was optically several times thicker than the underlying PBL aerosol (average optical depth of 0.34 as measured by the aircraft). By consequence AERONET retrievals should strongly reflect the smoke properties. Table 2.3 compares aerosol properties retrieved from AERONET [Dubovik *et al*, 2000] at the GSFC site for the day of the flight against those obtained from the aircraft in situ measurements. They represent fine mode aerosol, as the almucantar retrievals indicate that the coarse mode comprised only 3% of the total optical depth at 0.55 μm. Two values of the AERONET asymmetry parameter are listed: g = 0.65 is the listed value, while g = 0.62 comes from applying Mie theory calculations to the retrieved index of refraction and size distribution [Mishchenko *et al*, 2002]. When optical depth was retrieved by satellite using phase functions calculated from Mie theory (corresponding to the lower value of the asymmetry parameter), the results were nearly identical to optical depth retrievals using the higher listed value of the asymmetry parameter in the Henyey-Greenstein phase function. For consistency the Mie theory calculations are used throughout this study. The MDSC values of ω_o and asymmetry parameter were slightly higher than the GSFC values, possibly due to the location in a highly urbanized area. These values, therefore, were not considered as representative for the entire plume as those from GSFC and were not used in subsequent calculations. Only optical depth was retrieved at the SERC site, and in the clear days that immediately followed the smoke event, low optical depths prevented retrieval of other aerosol optical properties at any of the sites.

2.5 Development of a Two Layer Aerosol Optical Model

Calculation of the radiative effects of the smoke requires knowledge of the optical depth, single scattering albedo, and phase function. This is done in two steps: first the quantities are extracted from the data at one wavelength, then a model of the complex index of refraction that varies with wavelength is used with the size distribution to calculate the radiative properties across the spectrum.

The scattering and absorption coefficients are in units of effective cross sectional area per volume, so when added and integrated over vertical distance the optical depth results:

$$\tau(\lambda, RH) = \int_{z_1}^{z_2} \sigma_s(RH_{ref}) F(RH) dz + \int_{z_1}^{z_2} \sigma_a(\lambda, RH) dz \qquad (2.2)$$

where F(RH) is from equation 2.1, and the subscripts ‘s’ and ‘a’ refer to scattering and absorption. The 3 km MSL ceiling prevented the plane from capturing the entire smoke plume in each location. Nonetheless the measurements were used to calculate the aerosol optical depth that appears in table 2.2. The total uncertainties were calculated by adding in quadrature the combined instrument and correction factor uncertainties for scattering and absorption (15% and 20% respectively).

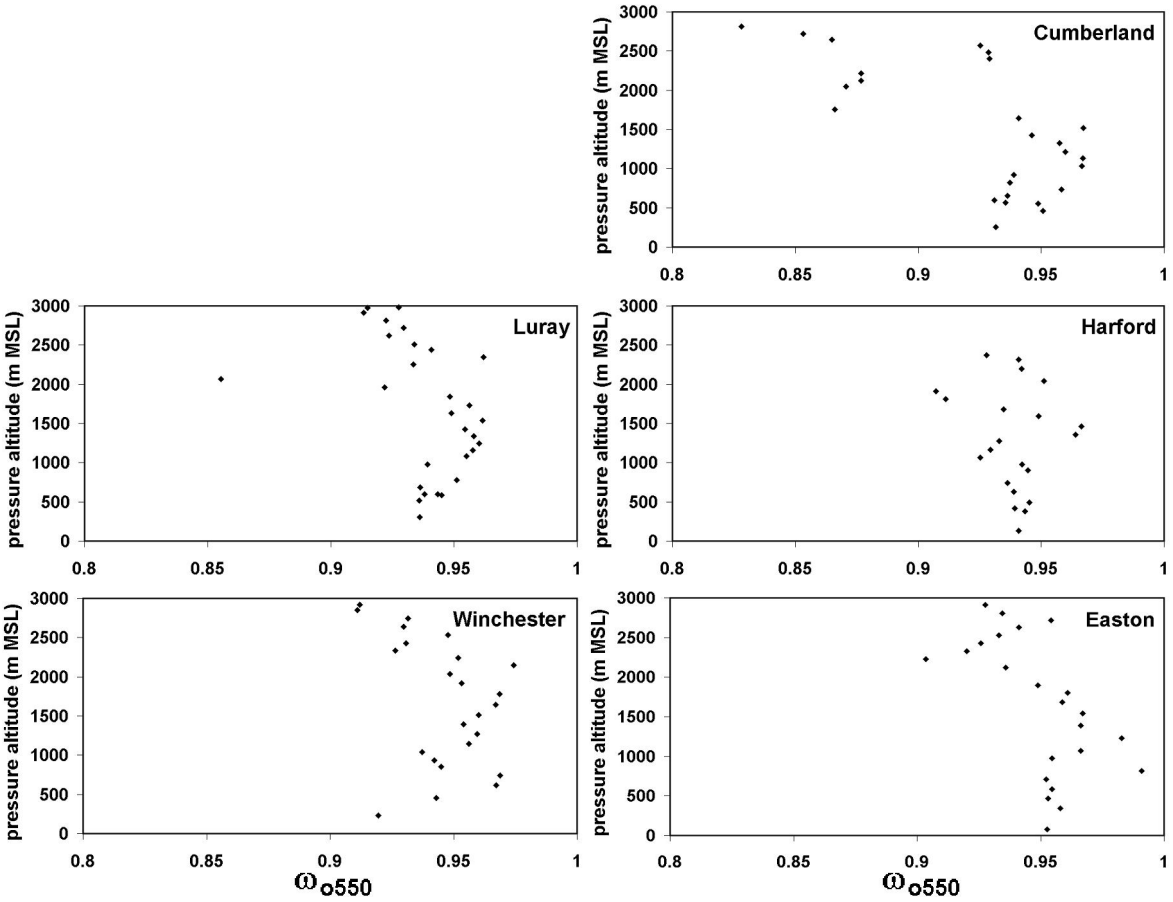

Figure 2.11: Single scattering albedo calculated from the values of Figs. 2.8 and 2.10

The single scattering albedo ω_o is calculated from the absorption and scattering cross sections at 550 nm. Vertical profiles appear in figure 2.11. A decrease in ω_o is seen above 2 km MSL for all locations except Harford. Cumberland had the lowest ω_o despite all other indications it had the weakest smoke signal, though this may be due to sampling issues from a lower particle count. Average values of ω_o for the ambient layer and the smoke dominated layer appear in table 2.3. Typical values (excluding Cumberland) are $0.93 \pm .01$ and $0.95 \pm .02$ for the smoke and PBL aerosol, respectively. These values are consistent with other studies in the region [Remer *et al*, 1998; Dubovik *et al*, 2002]. Uncertainties were calculated by assuming orthogonal variation in the effects of absorption and scattering, so that

$$\frac{|\Delta\omega_o|}{\omega_o} = (1-\omega_o)\left\{\left(\frac{\Delta\sigma_{sp}}{\sigma_{sp}}\right)^2 + \omega_o{}^2\left(\frac{\Delta\sigma_{ap}}{\sigma_{ap}}\right)^2\right\}^{1/2} \qquad (2.3)$$

	Effective radius $\mathbf{r_e}$	variance d(ln r)	Refractive index (n+ik)	single scattering albedo w_o	asymmetry parameter g
AERONET GSFC	0.15 mm	0.61	1.56+.0067i	$0.964 \pm .03$	0.65/0.62
Aircraft smoke	0.22 mm	0.46	1.58 + 0.015i	$0.930 \pm .02$	$0.66 \pm .04$
Aircraft PBL	0.08 mm	0.86	1.43 + 0.006i	$0.949 \pm .02$	$0.62 \pm .04$

Table 2.3: Regional aerosol properties assumed from AERONET and aircraft measurements.

The scattering phase function must be calculated from the size distribution and index of refraction of the aerosol. On July 8 the NASA Goddard AERONET station retrieved the real part of the index of refraction to be 1.56. This is a column average, so assuming a smoke to ambient optical depth ratio of 5:1 and setting the value of the ambient aerosol to the 7-year average of n=1.43 [Remer *et al*, 1997;Dubovik *et al*, 2002], a value of n = 1.58 was assigned to the smoke. Though higher than the average this value falls within the range of other measurements for smoke from this region [Fiebig *et al*, 2003]. For moderate absorption the scattering exhibits no significant dependence on the imaginary index of refraction (m). The AERONET value of m was assumed in order to find the size distribution based on scattering, and then later adjusted to match the single scattering albedo measured in situ. A mono-modal lognormal size distribution is completely described by two parameters: volume weighted average radius, and the logarithmic variance [Wilks, 1995]. These two parameters were adjusted until Mie

theory calculations [Mishchenko *et al*, 200] reproduced the measured scattering Ångstrom exponents for the pairs of wavelengths (450 nm, 550 nm) and (550 nm, 700 nm). For all radiation transfer calculations that follow, the scattering phase function was approximated by the first 8 terms of a Legendre polynomial expansion.

A single size distribution for each aerosol layer was used throughout the region (Table 2.3). This was done for two reasons. First, a single AERONET retrieval of the index of refraction had to represent the entire area. Second, since the two measured Ångstrom exponents available completely determined the size distribution, the retrieved distributions were very sensitive to these measurements. The retrieval is non-linear, so rather than average a number of retrievals skewed by individual measurement error, it is best to use averaged measurements in the retrieval, then investigate the response of the retrieval to perturbations in input measurements. This is done in section 2.12. The layer-averaged Ångstrom exponents at each site were weighted by AOD and averaged once more to arrive at the regional averaged measurements used to calculate the size distribution. This regional size distribution was used with the in situ AOD and single scattering albedo at each site to calculate local radiative effects.

2.6 Extrapolation of Single band to Wideband Optical Properties

To compute broadband radiative fluxes the single value of absorption measured at 565 nm and the three measurements of scattering at 450, 550 and 700 nm must be extrapolated across the solar spectrum from 0.3 to 3 micrometers. The size distributions

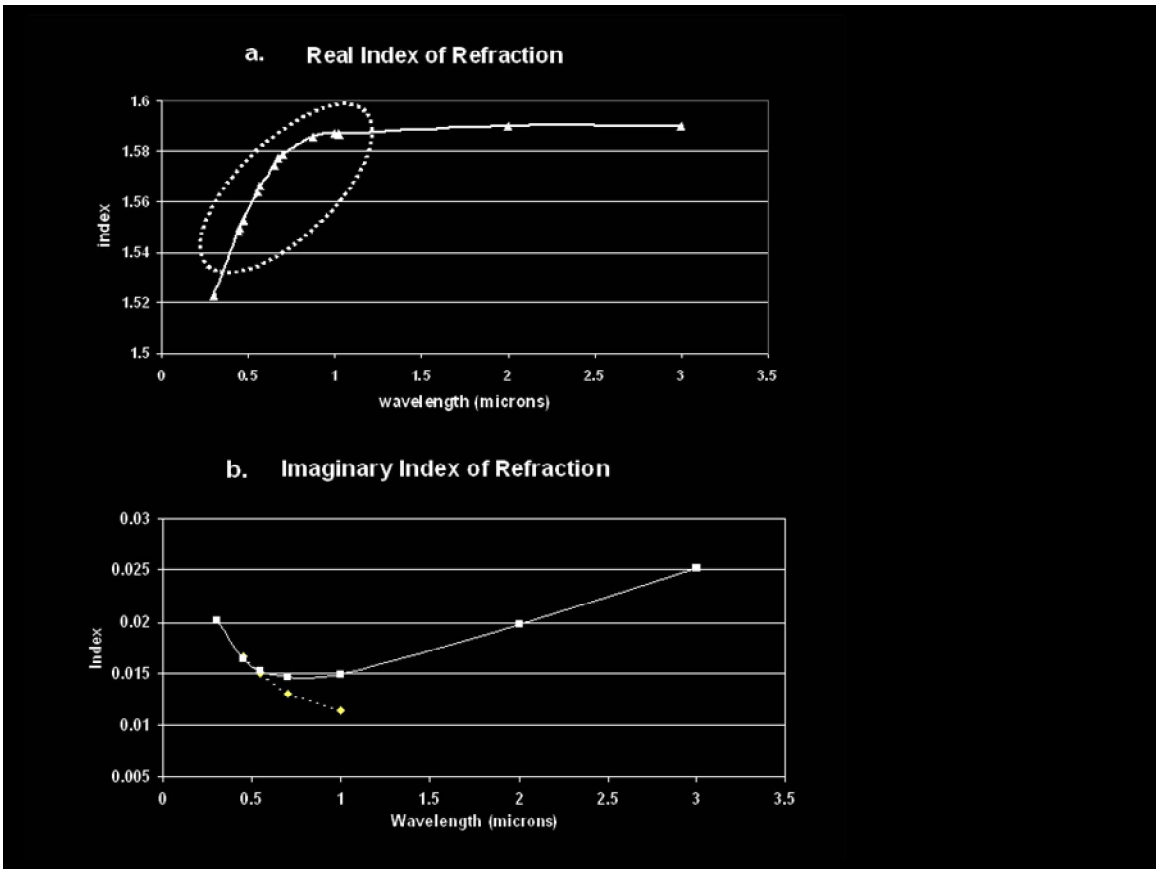

Figure 2.12: Assumed variation of the real and imaginary index of refraction based on AERONET retrievals and black carbon characteristics. The dotted circle in the top figure shows retrieved values; those outside are extrapolated. The dotted line in the bottom shows retrieved values, while the solid line is fitted to BC measurements.

inferred by matching Mie calculations to the Ångström exponents at these wavelengths may be used to calculated optical properties at any other wavelength [Mishchenko *et al*, 2003], but only if the real and imaginary parts of the index of refraction are known across the spectrum.

The most likely composition of aged smoke is a carbonaceous core with a sheath of a water/sulphate mixture [Fiebig *et al*, 2003; Remer *et al*, 1998]. The core would be composed of black carbon (soot) and other organic compounds [Conny and Slater, 2002].

With the exact composition unknown, the real part of the index of refraction was based on extrapolation of AERONET measurements, as shown in figure 2.12a. For comparison, Torres *et al* [2002] assumed a constant real index of refraction of 1.55 throughout the UV and visible for carbonaceous aerosols based on a number of measurements. Our values are slightly lower in the UV (n = 1.52 to 1.54) and slightly higher in the visible and NIR (n = 1.55 to 1.59), with a trend that resembles the Chang and Charampopolous [1990] measurements for black carbon. The imaginary part is commonly assumed to be due entirely to black carbon content [Bergstrom *et al*, 2002; Ramanathan *et al* 2001A; Fiebig *et al*, 2003]. Since the measured properties of soot vary widely with composition [Bergstrom *et al*, 2002; Russell *et al*, 1999b], the most applicable carbon absorption measurements must be selected to match observations in this area. Similar work was done during the TARFOX experiment [Bergstrom *et al*, 2002, Russell, 1999a,b], in which smoke was assumed to be mixed with aerosols from the same general area of the current study. In that study it was concluded that measurements of the refractive index of soot made by Chang and Charalampopoulos [1990] provide the best fit to observed data, and so the same data set will be used here. For the present study the imaginary index of refraction at 550 nm was adjusted until the calculated ω_o matched the in-situ measurements, and the proportionality between this value and the soot data was used to calculate the imaginary refraction index at all other wavelengths (Figure 2.12b). This is equivalent to adjusting the composition of black carbon as done in the TARFOX experiment.

2.7 Radiative Forcing Calculations for Each Site

2.7.1 Radiative Fluxes

Given scattering and absorption cross sections at every wavelength as calculated by Mie theory, aerosol optical depth measured at one wavelength was used to determine the optical depth at all other wavelengths by proportionalities, and the spectrally integrated radiative forcing calculated as a result. This technique was applied to the satellite derived maps of optical depth at 0.55 μm described above. The Santa Barbara DISORT Atmospheric Radiation Transfer (SBDART) code was used for all calculations [Richiazzi *et al*, 1998] using the LOWTRAN-7 solar spectrum and sixteen streams. Optical properties were calculated at wavelengths of 0.3, 0.4. 0.55, 0.7, 1.0, 2.0 and 3.0 μm, and the code interpolated these throughout the solar spectrum.

For wavelengths shorter than 2.1 μm the surface albedo used was from the MODIS Land Team Level 3 Eight Day Reflectance product [Vermote and Vermeulen, 1999]. This product uses a composite of cloud-free scenes to calculate surface reflectance at each wavelength, with an aerosol correction technique similar to that used by the MODIS Atmosphere Team aerosol product [Kaufman *et al*, 1998]. The period chosen was roughly 2-3 weeks after the smoke event, in which the average aerosol optical depth was typically 0.2 or less, thus reducing correction uncertainties. Nadir view scenes are preferentially selected for this product, and the time of the satellite overpass used in this study was close to noon, reducing the need for angular corrections. CERES mixed vegetation albedos were used for wavelengths higher then 2.1 μm (from code

available at the surface and radiation budget working group webpage, Charlock *et al*, 2002: http://snowdog.larc.nasa.gov/pub/surf/pages/explan.html)

Instantaneous forcings at TOA, surface, and atmospheric absorption due to both the smoke and PBL aerosol layers were arrived at by calculating the radiances with and without each layer, then subtracting to find the forcing. The results at each location appear in Table 2.4. The negative signs indicate surface cooling. The difference between the surface and TOA forcings are accounted for by atmospheric absorption. Since the entire plume was not measured at each site these values do not indicate the actual values, but do show representative trends.

	Total forcing			**PBL**			**Smoke**		
	ΔF TOA Wm^{-2}	Atmos Wm^{-2}	ΔF sfc Wm^{-2}	ΔF TOA Wm^{-2}	Atmos Wm^{-2}	ΔF sfc Wm^{-2}	ΔF TOA Wm^{-2}	Atmos Wm^{-2}	ΔF sfc Wm^{-2}
Luray	-47±7	115±17	-162±24	-26±4	30±5	-56±8	-21±3	85±13	-106±16
Winchester	-50±8	108±16	-168±25	-20±3	23±3	-43±6	-30±5	85±13	-115±17
Cumberland	-25±4	57±9	-82±12	-27±4	36±5	-63±9	2±1	21±3	-19±3
Harford	-42±6	124±19	-166±25	-31±5	57±9	-88±13	-11±2	67±10	-78±12
Easton	-57±9	167±25	-224±34	-29±4	29±4	-58±9	-28±4	138±21	-166±25

Table 2.4: Solar spectrally integrated forcing calculated for each site based on aircraft measurements.

For smoke the TOA forcing is much smaller than the surface, demonstrating that most of the attenuation of the surface light was due to absorption rather than scattering. The average single scattering albedo for smoke was 0.93, so single absorption events alone would reduce intensities by 7%. But since surface attenuations at various sites were several tens of percents, multiple scattering must have multiplied the absorption probability of single smoke particles. Backscattering from the more reflective layer

underneath the smoke would have additionally increased the absorption.

Forcing uncertainties arise from measurement errors in optical depth, as well as uncertainties in the assumptions of index of refraction and size distributions used to extrapolate from the measurement wavelength of 0.55 μm across the solar spectrum. For the ranges of AOD values found, forcing varied nearly linearly with optical depth, so the uncertainties carry over directly. Sensitivity tests in extrapolation were conducted by varying the real part of the index of refraction by +/- 0.04 (larger than the AERONET uncertainty of 0.03), and varying the angstrom exponents used to derived the size distributions by one standard deviation. The variations from these three possibilities were added in quadrature to arrive at the values quoted in Table 2.4. Further discussion of this error analysis is provided in section 2.12 with regard to regional calculations.

2.7.2 Heating Rates and Implications

Lowered radiative heating of the surface and absorptive heating in the atmosphere would have stabilized the column against convective mixing, slowing dispersal of the smoke plume [Park *et al*, 2001]. To explore this mechanism the heating rate was calculated for every vertical level measured by the plane, approximately every 100 m. The total absorptive heating, from sunrise until the time of the measurement, was surmised by integrating the calculation over every hour in this period. This calculation did not account for loss of heat due to thermal diffusion and radiation.

The temperature profile at each of the five locations showed similar characteristics independent of the aerosol loading: a steady lapse rate from the surface up

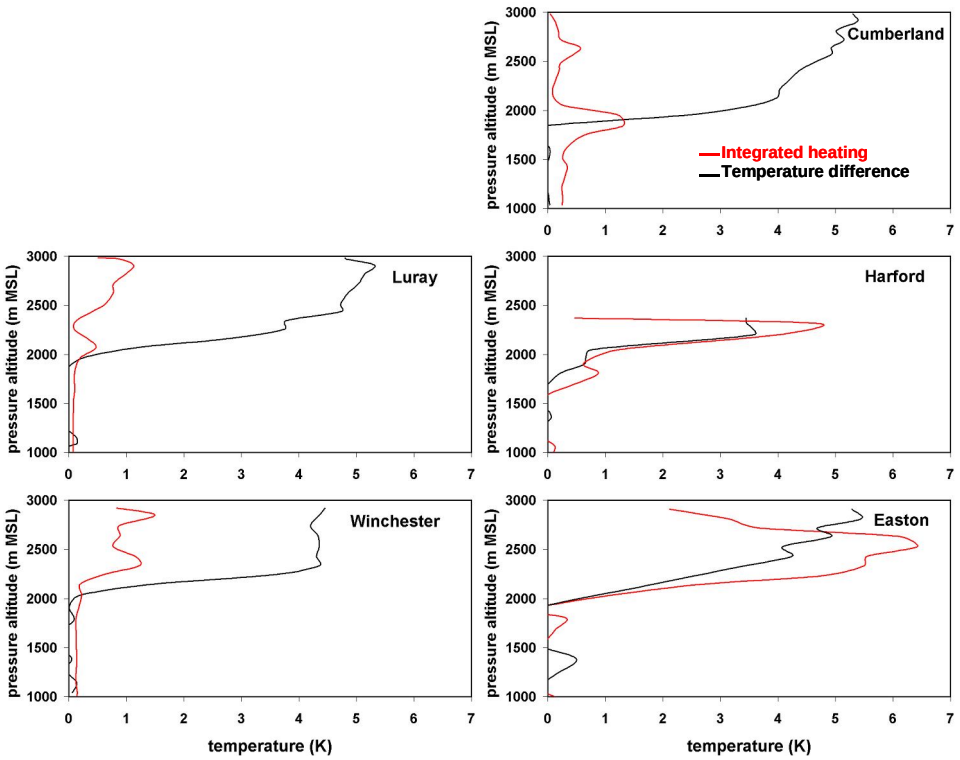

Figure 2.13: Magnitude of temperature inversion (black) compared to calculated heating (red). Morning profiles are on the left, afternoon on the right.

to the smoke layer, followed by a temperature inversion of 4 or 5 degrees centigrade (Figure 2.6). The sudden drop in dewpoint at the inversion altitude indicates subsidence from the high pressure system. The size of the inversion is calculated by extrapolation of the PBL temperature profile into the smoke layer, then subtracting it from the actual temperature profile. The influence of absorption in the smoke layer is evaluated by comparing the integrated heating rate to the size of the temperature inversion, as done in Figure 2.13.

The integrated heating is too small to account for the temperature inversion in the morning sites, but can account for it in the afternoon sites of Harford and Easton. The

smoke could not have caused the inversion, as indicated by its presence in the morning as well as at Cumberland, where the smoke presence was negligible. But it could easily have strengthened and helped maintain the inversion; capping convection and reducing smoke dispersal by mixing. This mechanism could explain how some smoke plumes maintain their integrity over long-range transport [Keil and Haywood, 2003].

2.8 Comparison of Region-Wide Optical Models

In section 2.5 regional average size distributions for each aerosol layer were calculated from averaged scattering Ångstrom exponents measured in situ at the various sites. The same can be done for the single scattering albedo. Since AERONET retrievals provide similar information for the column average, it is fruitful to compare the two models as done in Table 2.3 as reference for the following discussion.

Figure 2.14a shows the lognormal curves of the size distributions for the smoke and PBL layers derived from the Ångström exponents, together with data points from the MET-One measured size distributions as a consistency check. The AERONET retrieval is given for comparison. Though the lognormal curve for the AERONET distribution was

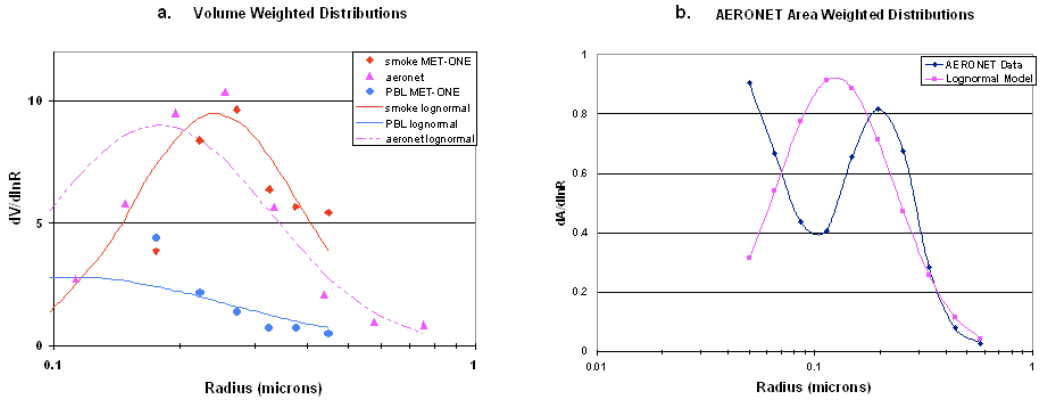

Figure 2.14: a) Volume weighted size distributions from AERONET, Met-One particle counter, and the scattering Ångstrom exponents. b) Area weighted AERONET compared to scattering model.

based directly on statistics from the data, the volume-weighted curve does not appear to fit the data well. Figure 2.14b replots the AERONET data in the more radiatively significant area weighted form (effective radius) that accentuates the lower wing of the distribution. A bimodal distribution is now clearly visible, with the fitted mono-modal lognormal curve expected to serve as an optically equivalent average distribution [Tanre et al, 1996]. Table 2.3 presents the volume-weighted radius and variance for the lognormal curves fitted to the AERONET retrieval, with the PBL aerosol and smoke values derived from Ångström exponents. As expected for a column average, the smoke and PBL values bracket those of AERONET.

The column averaged volume weighted radius (r_v) retrieved from AERONET was 0.18 μm, corresponding to the effective radius of 0.15 μm listed in Table 2.3. The climatological PBL r_e is 0.16 μm [Dubovik et al, 2002], which is very close to the smoke dominated column value. Performing a weighted average will have very little effect on the smoke value. The column averaged size distribution retrieved by AERONET,

therefore, was used to represent pure smoke.

The column averaged AERONET value of ω_o interpolated to 550 nm is about 0.964. At GSFC the climatological value (1998-2001) of ω_o is $0.98 \pm .02$ [Dubovik *et al*, 2002]. Assuming the ω_o retrieval represents a weighted average of PBL aerosol with approximately 5 times as much smoke aerosol, the smoke ω_o would be about 0.962. Since this value is not a significant departure from the original AERONET value, the column-averaged ω_o was used to represent smoke for the model comparisons that follow.

2.9 Comparison of Regional Optical Depth Estimated by Satellite

2.9.1 The Satellite Retrieval Algorithm

The satellite retrievals described in this section assume that the values of ω_o and phase function measured at one location are valid throughout the area shown in figure 2.3. The in situ measurements at the four locations and the three AERONET sites all showed variations from the mean values that were within the instrumental and statistical uncertainties of the respective instruments and data sets (see Table 2.2, the sensitivity section below, and Dubovik *et al* [2000]). It is therefore consistent to assume average values for these properties within the area defined by the flight locations. Based on the size of the meteorological system in which the measurements were made, the study area was extended across several degrees of latitude and longitude in order to include all three AERONET sites, the SURFRAD and ISIS sites depicted in Figure 2.3.

The satellite TOA radiances were measured in band 4 (550 nm) of the MODIS

instrument at 5 km resolution, using the Terra overpass from 1540 to 1545 GMT. This band was chosen because it was closest to the in situ absorption measurement at 565 nm while corresponding directly to one of the scattering wavelengths measured. It is also in the middle of the range of wavelengths retrieved by AERONET, so properties such as index of refraction and single scattering albedo may be easily interpolated.

As before the SBDART code was used for all radiative calculations [Ricchiazi *et al*, 1998]. Tests have been conducted in which the radiance outputs of the satellite algorithm for retrieved optical depths were compared to an adding-doubling radiation transfer code written in house and extensively validated by Chang [2000]. The comparisons agree to within a few W/m^2/steradian.

The surface albedo was as described in section 2.7.1. Atmospheric inputs included average aircraft measurements of temperature, ozone, and water vapor up to 3 km, with the standard mid-latitude summer atmosphere above 3 km.

A two-layer aerosol as depicted in Figure 2.15 was assumed: the PBL aerosol in the layer from the surface to 2km, with the smoke added to the layer from 2 to 3 km. The PBL aerosol was set to the average optical depth of 0.34 ± 0.1 as measured by the aircraft, with a ω_o of $0.95 \pm .01$ and an asymmetry parameter of 0.62. The uncertainty in optical depth is due to the spatial variability between measurement spirals. The smoke optical properties were derived either from the average aircraft values (ω_o= 0.93 and g = 0.66) or AERONET retrievals (ω_o= 0.963 and g = 0.62). To perform a satellite retrieval of optical depth, aerosol in the PBL layer was assumed to be spatially invariant while the

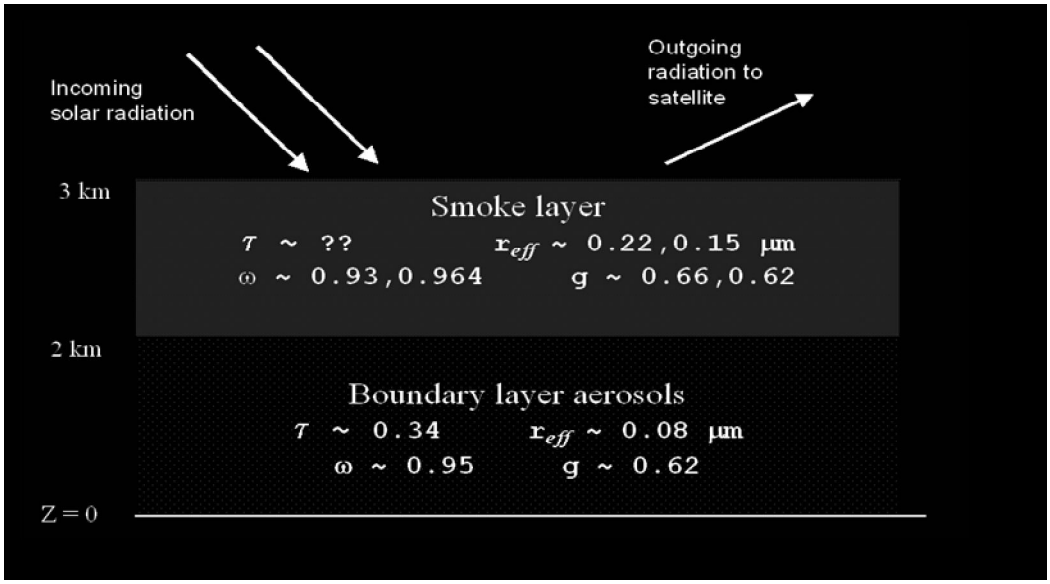

Figure 2.15: Optical properties assumed for each layer. When two values are given, the first is based on aircraft in situ measurements, the second on AERONET retrievals.

quantity of smoke was adjusted until the calculated and measured radiances at TOA matched.

Visible MODIS imagery for the Terra satellite at 1540 GMT shows how the addition of smoke brightens the scene from dark to gray (Figure 2.16a). It is not easy to distinguish between thick smoke and cloud using visible wavelengths. As shown in Figure 2.16b the MODIS operational cloud screen (MOD35), using a combination of visible and brightness temperature thresholds, mis-identified smoke as clouds since training sets typically do not include thick smoke plumes. With cloud droplets typically a few microns in radius while smoke particles fall in the submicron range, reflectivity in the near IR wavelengths may be used to distinguish between the two [Kaufman *et al*, 1990b]. A cloud screen based on NIR thresholds indicates that the area under analysis is almost entirely cloud free (Figure 2.16c).

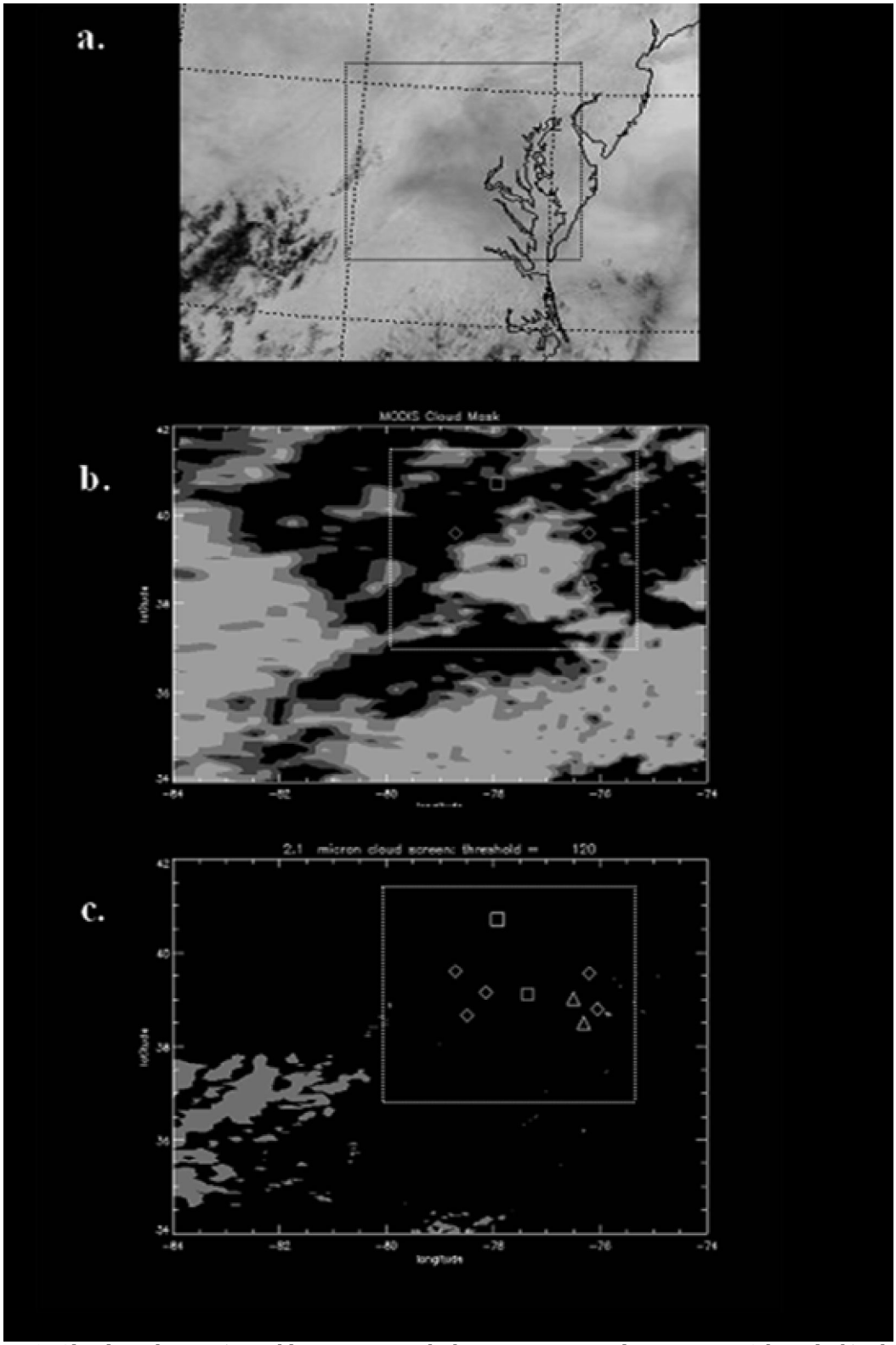

2.16: Cloud masking. a) Visible imagery, with the area corresponding to Fig. 2.3 boxed. b) The MODIS aerosol team cloud mask, with clouds shown as dark. c) Remaining clouds after the 2.1 μm threshold is applied.

2.9.2 Comparisons of Satellite Optical Depth Retrievals

A comparison of the two sets of aerosol optical properties is summarized in Table 2.3. Although the size distribution parameters for smoke and PBL aerosol bracket those of AERONET, the single scattering albedo for AERONET is higher than either in situ measurement. Sensitivity tests in a later section demonstrate that this difference is the primary factor in disparities between the optical depth retrievals.

AERONET observed optical depth at each of the three sites within the region of interest was compared to the satellite retrieved optical depth calculated from two primary optical models: AERONET column average, or in situ layered structure as measured by aircraft. Two mixed models employ the same PBL layer, but use combinations of aircraft and AERONET ω_o and phase functions in the smoke layer (Table 2.5).

Single Scattering Albedo	Scattering Phase Functions	GSFC (4 pixels)	SERC (3 pixels)	MDSC (4 pixels)
In Situ + PBL	**In Situ + PBL**	**2.25 ± .10**	**2.18 ± .26**	**1.92 ± .08**
AERONET + PBL	In Situ + PBL	1.71 ± .07	1.67 ± .21	1.46 ± .06
AERONET+ PBL	AERONET+ PBL	1.55 ± .06	1.51 ± .19	1.33 ± .05
Pure AERONET	**Pure AERONET**	**1.54 ± .06**	**1.50 ± .19**	**1.31 ± .05**
AERONET Observations		***1.68 ± .04***	***1.79 ± .03***	***1.34 ± .04***

Table 2.5: Comparison of Optical Depth Retrievals. The first three rows show the satellite retrieved optical depth of smoke added to the assumed optical depth of the PBL aerosol, the fourth row is a satellite retrieval of the entire column of aerosol based on the AERONET derived properties. The source of the optical parameters used as inputs are listed on the left. Uncertainties represent the variation in values retrieved from surrounding pixels only, and does not reflect instrument or algorithm error. The bottom row lists the optical depths observed by AERONET interpolated to the time of the satellite overpass, with instrumental and interpolation uncertainties included.

For purposes of comparison, AERONET optical depth measurements at wavelengths of 440 and 670 nm were interpolated logarithmically to 550 nm, and also interpolated linearly in time to match the satellite overpass. The stated algorithm uncertainty for the AERONET observations is ± 0.02 [Holben *et al*, 1998] with the interpolations also adding estimated uncertainties up to $\pm .02$. The optical depths measured by AERONET and calculated by satellite data for the four models are shown in Table 2.5. The four pixels that fall within a 0.1° box centered on each sensor were averaged so that data within a radius of about 7 km were included; the uncertainties shown are the sample standard deviations only. One of the points in the SERC set was over the bay with spuriously high surface reflectance, and so was rejected.

MODIS collection 4 aerosol retrievals are included for comparison due to general interest in this operational data set. Values of optical depth were generated for both the smoke model used in the western U.S. and the operational retrieval for the eastern U.S. with cloud screening turned off. The operational values of $\omega_o = 0.96$ and $g = 0.66$ are closer to the AERONET retrievals than any of the other models, yielding a value of optical depth very close to that directly observed by AERONET.

Satellite retrievals using the aircraft and AERONET optical properties produced the highest and lowest optical depths, respectively, with the mixed models exploring the sensitivity of satellite retrievals to absorption (represented by ω_o) and size distribution (represented by scattering phase functions). The largest change is due to variations in ω_o:

the roughly 30% increase in optical depth is disproportionate to the 3.5% decrease in scattering per photon interaction. For large optical depths multiple scattering assumes a dominant role [Bohren, 1987], and with multiple chances for each photon to be absorbed the decrease in reflected light is a nonlinear function of the single scattering albedo [Wong and Li, 2002]. When aircraft scattering phase functions are changed to those from AERONET the retrieved optical depth decreases by roughly 10%, as expected for increased backscattering due to smaller particles. Use of the PBL aerosol layer with an AERONET smoke layer produces an optical depth almost identical to the pure AERONET aerosol: the combination of lower ω_o with smaller particles at the bottom of the plume produces nearly the same TOA reflectance.

The effect of a thick absorbing aerosol is apparent in the regional distribution of satellite retrieved optical depth (Fig. 2.17). For the 1540 GMT Terra satellite overpass the two primary models are shown, with the MODIS operational retrieval exhibited for comparison with the cloud screening turned off (17d) [Kaufman *et al*, 1997]. Ratios between the optical depths of the two models show that the model disparity increases with optical depth (Figure 17c).

The gray areas in the upper left of figure 2.17 indicate areas where the calculated amount of reflectance from the assumed PBL aerosol optical depth of 0.34 was larger than the satellite observation. They correspond to mountainous regions of clearer air. The gray areas that lie in a line between the two AERONET sites correspond to parts of the Chesapeake Bay where the surface reflectance product produced spuriously high reflectances, and so these points must also be rejected. Other scattered gray areas are the

result of the cloud-screening algorithm.

The comparison demonstrates the high sensitivity of satellite-based retrieval of aerosol optical depth to the aerosol optical properties. The retrievals using AERONET optical properties are the lowest, while those using in-situ measurements are the highest.

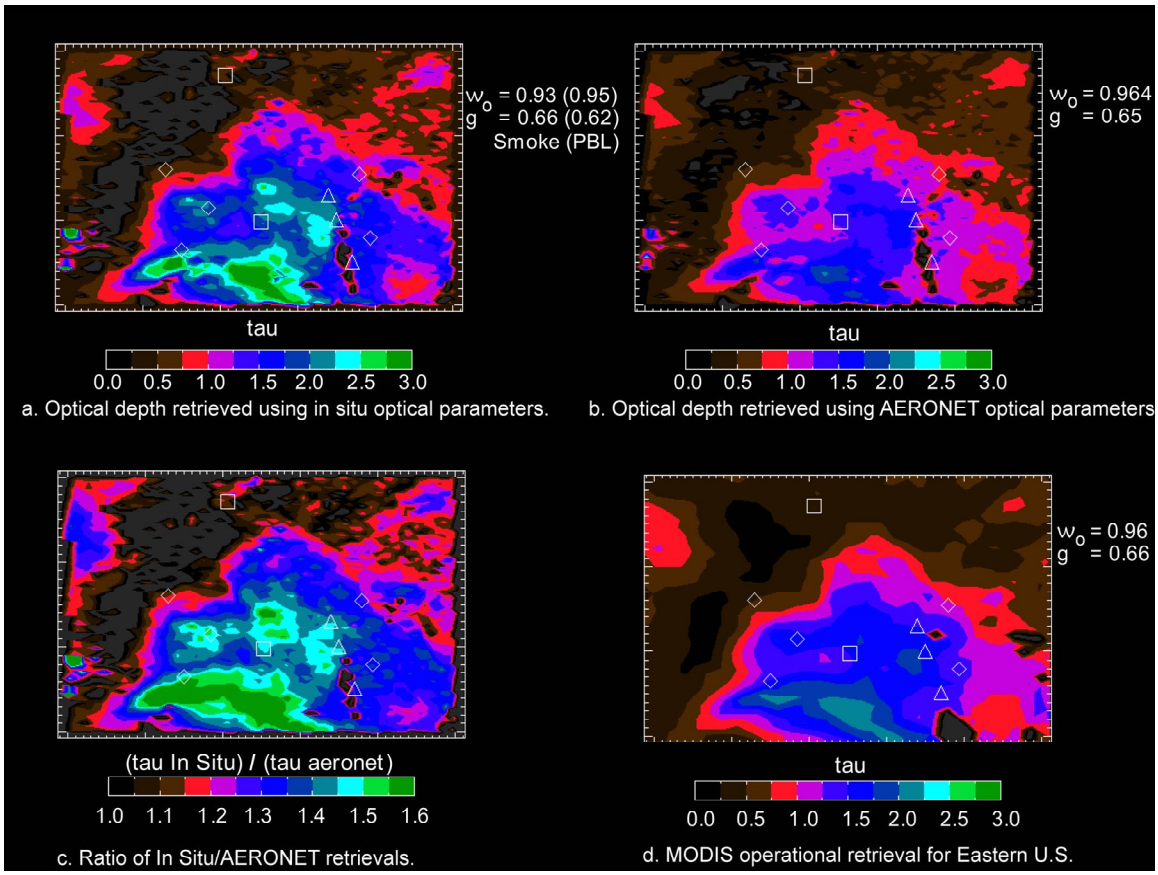

Figure 2.17: Comparison of optical depth retrievals via satellite. For symbol definitions see Figure 2.3.

As shown in figure 2.17c for thick plumes it is not uncommon to see ratios of 1.5 or more. We may thus argue that the aerosol optical depth retrieved by satellite is subject to considerable uncertainty linked to the measured optical properties used as inputs, especially for thick layers of absorbing aerosol.

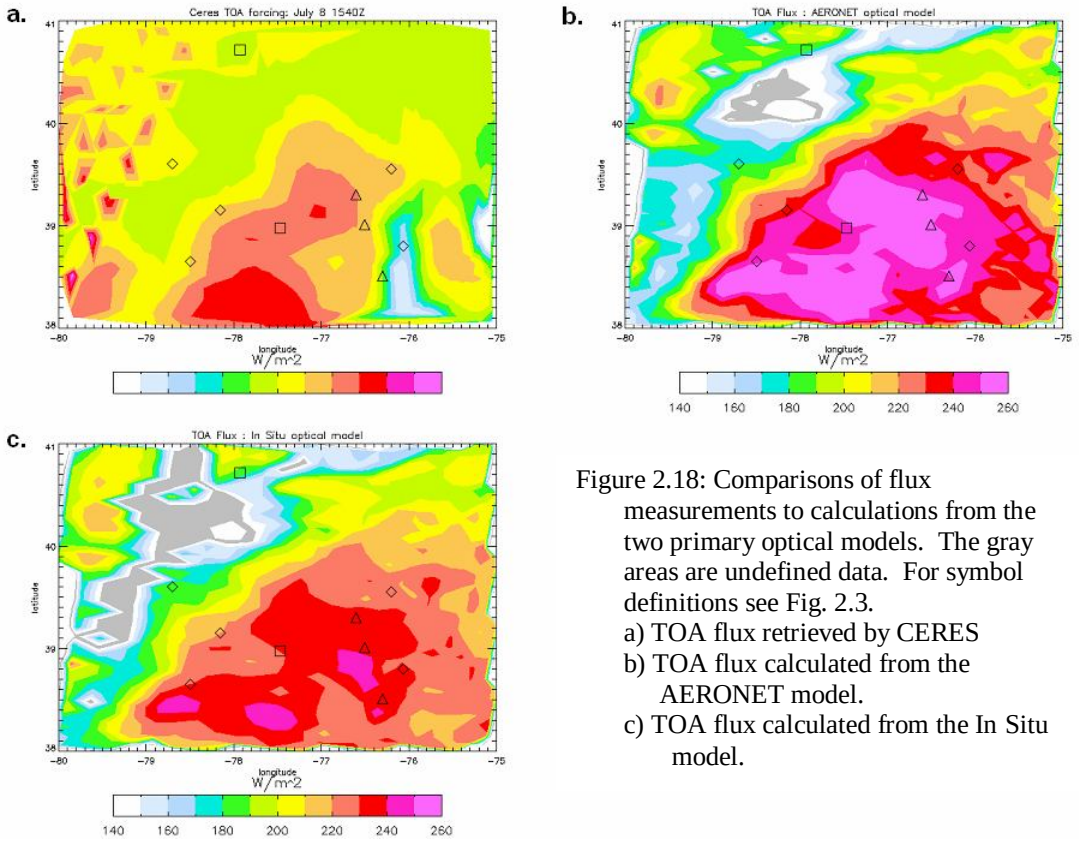

Figure 2.18: Comparisons of flux measurements to calculations from the two primary optical models. The gray areas are undefined data. For symbol definitions see Fig. 2.3.
a) TOA flux retrieved by CERES
b) TOA flux calculated from the AERONET model.
c) TOA flux calculated from the In Situ model.

2.10 Comparison of Forcing Calculations

The forcing calculations described in section 2.7 were applied to the four regional optical models of the previous section, providing regional surface and TOA maps of spectrally integrated fluxes or forcing. Such maps allow comparison to surface

measurements at several locations (figure 2.18), while TOA flux calculations may be compared to satellite observations.

Table 2.6 shows a comparison of spectrally integrated surface forcing measurements (clear sky flux minus smoky sky flux) taken by SurfRad and ISIS instruments to calculations for the four optical models. All measurements and calculations correspond to the time of the satellite overpass, with temporal interpolation

Single scattering albedo	Scattering phase functions	SurfRad 1541 Z		ISIS 1541 Z	
		Tau	Forcing (W/m^2)	Tau	Forcing (W/m^2)
In Situ + PBL	**In Situ + PBL**	**0.57 ± .12**	**-102** ± 19	**1.93 ± .09**	**-297** ± 11
AERONET + PBL	In Situ + PBL	0.53 ± .09	-87 ± 12	1.47 ± .04	-193 ± 4
AERONET + PBL	AERONET+ PBL	0.51 ± .08	-88 ± 12	1.33 ± .03	-188 ± 3
Pure AERONET	**Pure AERONET**	**0.45 ± .12**	**-58** ± 17	**1.32 ± .03**	**166** ± 3
Measured Forcing			***-113*** *± 11*		***-246*** *± 8*

Table 2.6: Spectrum integrated surface forcing at the two broadband radiometer sites. The top four rows are calculations based on satellite retrievals of optical depth, the bottom row are the actual measurements. Uncertainties indicate spatial variation between pixels surrounding the site for the satellite retrievals; temporal interpolation error for radiometers.

of the data as needed. The low optical depth at the SurfRad site means the column is dominated by the PBL aerosol, while the ISIS site is dominated by smoke. In both cases the aircraft in situ model performed best: calculations were about 10% below measurements when dominated by PBL aerosol, and about 20% high when dominated by smoke. Forcings calculated for the pure AERONET model were half the

measured value when dominated by PBL aerosol, 2/3 when dominated by smoke.

It is unlikely that the low forcing values calculated from the AERONET optical properties are due to the use of fine-mode retrievals alone: although the proportion of optical depth due to coarse mode increases with wavelength, the almucantar retrievals indicate the coarse mode optical depth at 1.02 microns was less than 10% of the total optical depth. Even if the coarse mode comes to dominate the forcing in the longer wavelengths the solar spectrum contains insufficient energy in this region to contribute significantly to the total forcing. The larger surface forcing calculated for the aircraft model is due in large part to the retrieval of larger optical depths, which in turn is due primarily to larger absorption measurements. Note that the size distribution affects the spectral variations of aerosol optical depth and single scattering albedo. At the SurfRad site as the model changed from AERONET+PBL to pure AERONET, the decrease in forcing was largely due to substituting the significantly narrower AERONET size distribution for the dominant PBL distribution. Broadband forcing is the integral of spectral forcing at each wavelength. A narrow size distribution produces a narrow scattering spectrum. Broader size distributions thus produce a larger broadband forcing as the scattering spectrum is integrated across the wavelength domain.

The CERES instrument, mounted on the same satellite platform as the MODIS instrument used to retrieve optical depth, provides broadband radiation measurements that can be used to estimate TOA forcing. The product used was the ERBE-like inversion of radiance to instantaneous TOA flux (ES-08) [Green and Robbins, 1997]. In

this product the measured radiances are converted to fluxes using anisotropy functions based on inferred surface type. This data set must then be considered to be a retrieval rather than a measurement of broadband flux. In figure 2.18 the TOA flux retrieved by CERES is compared to that calculated using the aircraft and AERONET aerosol optical models based on the retrieved optical depths. The fluxes calculated by both models are higher than those retrieved by CERES, though the aircraft model is significantly closer to the CERES data. Since the retrieved optical depth using the AERONET model is lower than that using the aircraft model, the larger forcing is due entirely to the aerosol optical properties: smaller, less absorbing particles with a broader distribution produce a larger backscatter signature than the smoke particles measured by the aircraft. This is similar to the SurfRad case in which the predominance of the smaller PBL aerosol with a broad distribution produced larger surface forcing than the AERONET model aerosol.

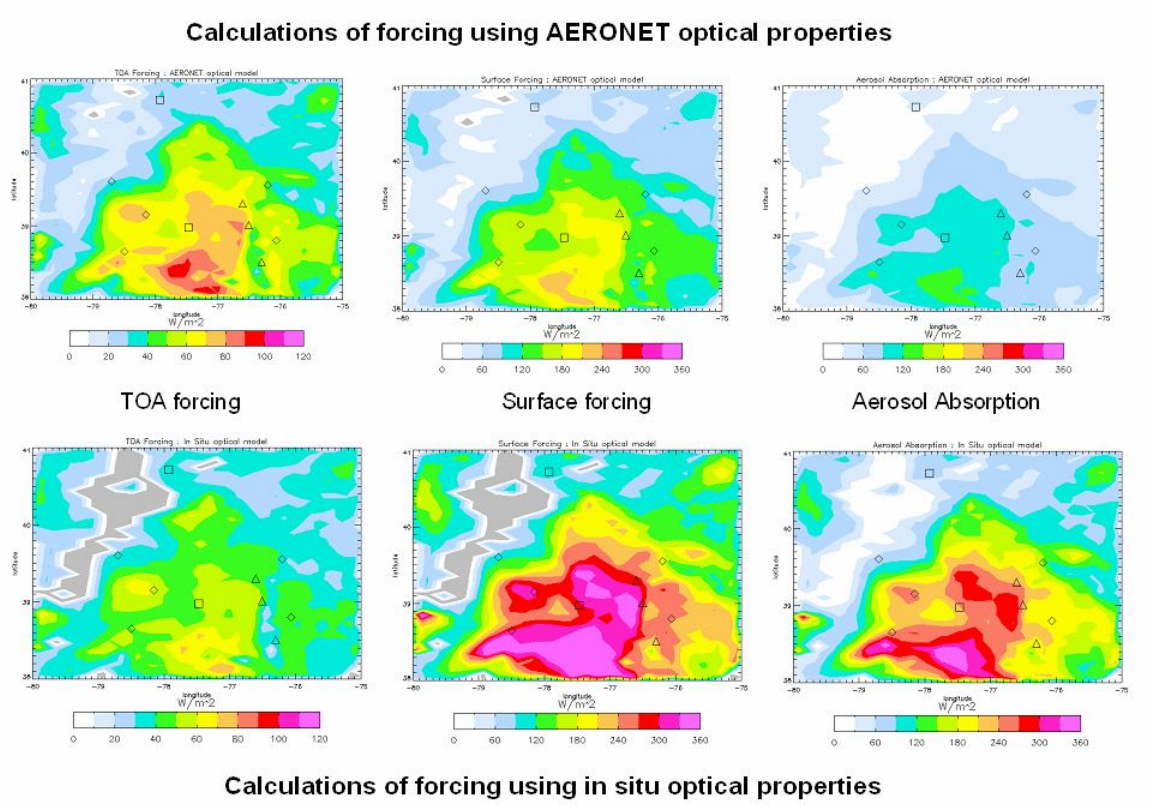

Figure 2.19: Radiative forcing maps calculated from the optical depth retrievals and optical models. The top row is based on AERONET, the bottom row is based on in situ data. For symbol definitions see figure 1. Gray areas are undefined data. The color scale ranges from 0 to 120 W/m^2 for TOA forcing, 0 to 360 W/m^2 for the absorption and surface forcing.

The presence of aerosol darkens the surface, increases the reflected flux at TOA, and causes atmospheric heating by absorption. Maps of surface forcing, TOA forcing, and absorption for the two primary models appear in figure 2.19. Given that the flux measurements at the surface and TOA both came closer to agreement with the aircraft optical model, the calculated forcing based on the aircraft model may be closer to reality.

2.11 Uncertainty Analyis for Retrieved Optical Depth

2.11.1 Absorption and Single Scattering Albedo

For a fixed TOA reflectance, satellite derived optical depth varies rapidly with single scattering albedo as shown in figure 2.20. It is seen that an increase in ω_o results in a decrease in optical depth at a rate that grows with optical depth. There is no simple relation that captures this behavior perfectly; a rough approximation for the range of optical depths in figure 2.20 is achieved by the relation

$$\Delta\tau \approx -(5\tau^{5/2})\Delta\omega_o \qquad (2.4)$$

So for the typical optical depth τ = 2, an increase in the single scattering albedo of 0.01 results in a decrease in optical depth of ~0.28 or 14%. When the AERONET retrieval of ω_o= 0.973 at the MDSC site is used in this formula (a value previously rejected as nonrepresentative of the entire plume), it can be seen that the increase in ω_o of +0.01 would result in a drop of optical depths of approximately 0.1, bringing the MDSC optical depth in Table 3 close enough to the AERONET measurement to be within satellite retrieval uncertainty.

The estimated instrumental measurement uncertainty of absorption and scattering is 25% and 15%, respectively [Taubman *et al*, 2004]. For most aerosols the absorption is much smaller than the scattering, so scattering uncertainties largely cancel when the ω_o ratio is calculated. For the assumed instrumental uncertainties in scattering and absorption the resulting uncertainty in ω_o is about 2% or 0.02 [Reid *et al*, 1998A]. This matches the statistical sampling uncertainty, implying that instrumental variations in the measured properties may be as significant as spatial or temporal variations.

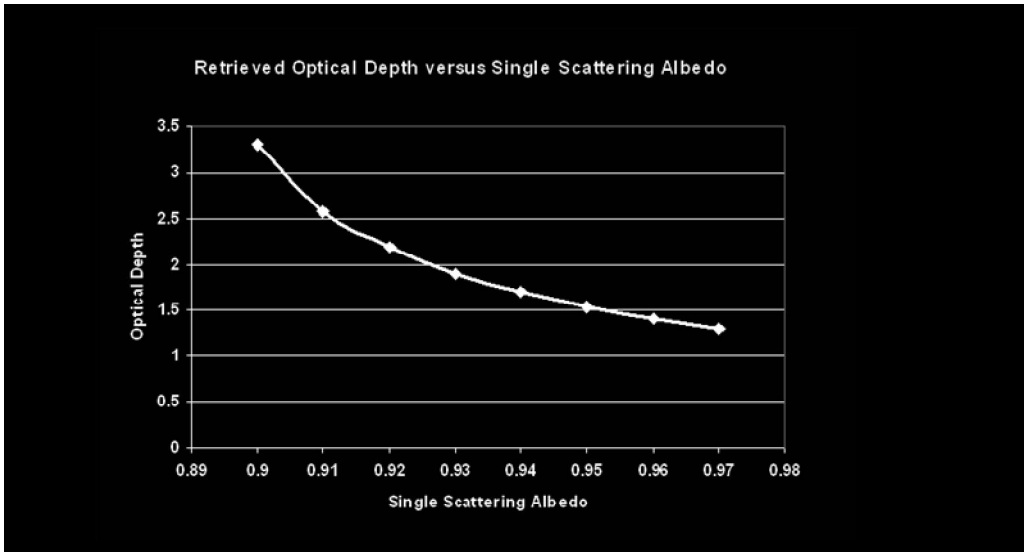

Figure 2.20: Retrieved AOD as a function of single scattering albedo for fixed TOA radiance.

2.11.2 Surface Reflectance

The sensitivity of retrieved optical depth, τ, to the surface reflectance depends on sun – satellite geometry as well as the optical depth. To test this sensitivity a point was selected in the middle of the flight pattern to represent the typical geometry used in this study. For a fixed radiance measured by satellite, changes in the surface reflectance are balanced by a contrary change in retrieved aerosol optical depth. A set of calculated test cases indicate how the sensitivity of optical depth to surface reflectance decreases with optical depth. For a typical uncertainty in surface reflectance of $\pm .02$ we can expect an uncertainty in optical depth of ± 0.1 for optical depths close to 2, smaller for higher optical depths. This is about a 5% uncertainty for the optical depths measured at the AERONET sites.

2.11.3 Phase function

The phase functions were determined from the scattering Ångström exponents, which are assumed to be variable within one standard deviation of the average values. The sensitivity of retrieved optical depth of smoke to the perturbations in the Ångström exponents is shown in Table 2.7. Asymmetry factors are included as an indication of how the calculated optical properties are affected by these perturbations.

The optical properties are affected more by the spread of the Ångström exponents than their actual magnitudes. For this case so long as the exponents are moved towards or away from each other by one standard deviation of their initial value, a change in optical depth of 15-20% is effected.

	Angstrom Exponents	g	Tau GSFC
"average"	$\alpha_{450/550}$ + 0, $\alpha_{550/700}$ + 0	**0.662**	**1.90**
"high"	$\alpha_{450/550}$ +s.d., $\alpha_{550/700}$ + s.d.	0.656	1.87
"low"	$\alpha_{450/550}$ - s.d., $\alpha_{550/700}$ - s.d.	0.667	1.94
"tight"	$\alpha_{450/550}$ + s.d., $\alpha_{550/700}$ - s.d.	0.638	1.60
"wide"	$\alpha_{450/550}$ - s.d., $\alpha_{550/700}$ + s.d.	0.691	2.33

Table 2.7: Retrieved optical depth of smoke as a function of the scattering phase functions derived from scattering angstrom exponents measured in situ. Note that optical depth does not include PBL.

The real part of the index of refraction also affects the derived phase functions. The bottom of Table 2.8 shows how the retrieval is very stable for $1.54 < n < 1.62$, but produces large variations in optical depth when n becomes lower. Numerical tests of the AERONET *al*gorithm [Dubovik *et al*, 2000] indicate that for a real refraction index of

1.45 and optical depths of 0.5, the accuracy is about $\pm .03$, well within the stable range for this optical depth retrieval.

		Tau ISIS (Sterling VA)	Surface Forcing (Watts/m^2)	TOA Forcing (Watts/m^2)
Average properties:	Total	**1.93**	**-297**	**-50**
	PBL	**0.34**	**-64**	**-25**
Angstrom exponent variations				
"tight"		1.66	-279	-54
"wide"		2.28	-324	-44
"low"		1.96	-299	-49
"high"		1.90	-295	-51
Index of refraction variations				
n = 1.50		2.45	-345	-43
n = 1.54		1.97	-299	-49
n = 1.62		1.92	-298	-50

Table 2.8: effects of variation of scattering Angstrom exponents and real index of refraction on retrieved radiative forcing. Refer to table 5 for explanation of the types of variations in the two exponents. The PBL aerosol layer was not varied, so these values of forcing may be subtracted to find the forcing due to smoke alone.

2.11.4 Boundary layer aerosol thickness

All the calculations above involving a two level model assume a constant boundary layer aerosol optical depth of 0.34 ± 0.1 in order to isolate the effect of smoke aerosol. While this value represents the average conditions of the background aerosol, the actual value is expected to vary across the region at the time of satellite overpass. The retrieved optical depth of the smoke layer must compensate for variations in the PBL

layer, which is unrealistically held constant. The resulting uncertainty in smoke optical depth should thus be approximately equal to the 0.1 uncertainty of the PBL.

2.11.5 Total Uncertainty in Optical Depth

Adding the above effects in quadrature results in a combined uncertainty of $\pm 22\%$ for the satellite retrieved optical depths close to 2 in the vicinity of the AERONET stations. This is sufficient to encompass the range of values calculated for the various optical models. From a satellite retrieval standpoint the optical properties as measured either in situ or by AERONET are therefore equivalent given the current instrumental uncertainties for moderate optical depths.

2.12 Uncertainty Analysis of Forcing Calculations

Forcing calculations may be affected both by the retrieved optical depth at 550 nm and by the size distribution that dictates the ratios of optical depths across the spectrum. Changes in the imaginary index of refraction affect the retrieved optical depth without a significant effect on the size distributions calculated from scattering Ångström exponents. For the range of optical thicknesses retrieved in this study the calculated surface forcing is proportional to optical depth, so for an instrumental uncertainty in ω_o of ± 0.02, from equation 1 the uncertainties in smoke optical depth of 5% and 16% at the SurfRad and ISIS sites, respectively, will yield the same uncertainties in surface

forcing.

The size distribution calculation, however, is affected by variations in both the assumed real index of refraction and the scattering Ångström exponents. Table 2.8 shows the effect of these possible variations at the ISIS site because the smoke loading at SurfRad was too low to show appreciable effects.

Sensitivity to the real part of the index of refraction was tested by shifting values throughout the spectrum equally, so that all comparisons can be referenced to the variation of n at 0.55 μm. As shown in table 2.8 the value for the real index of refraction, n = 1.58, is within an area of stability for variations on the order of 0.04, with lower values leading to significantly higher retrieved forcings. Dropping the index of refraction as low as 1.54 at 0.55 μm (and hence even lower in the UV) without a significant change in radiative effects allows comparison to similar studies [Torres *et al*, 2002] for which the index of refraction varied from the value assumed for this paper.

Separation between scattering exponents has a larger effect than an equal shift in the value of both exponents: the closer together the exponents are, the broader the size distribution. When the size distribution is distorted the variation in TOA flux may not be related to the resulting changes in retrieved optical depth: even if the optical depth at 0.55 μm decreases, the broadband reflected flux may increase (Table 2.8). Once again, a broad distribution results in a more uniform forcing across the spectrum and an increased total forcing.

Combining uncertainties in optical depth and size distribution leads to an estimated uncertainty in surface forcing of ~6% at the SurfRad site (dominated by a fixed

PBL layer), and ~19% at the ISIS site. The surface forcing calculated using the in situ measured optical properties falls within this range, while that calculated using the AERONET retrieved optical properties does not. The TOA flux may be compared across the entire region. Surface effects are highly variable across the spectrum and difficult to quantify. The possible variations due to aerosol alone contribute about 11% to the total uncertainty. As a result most of the TOA fluxes calculated for pixels in the thick part of the plume using the in situ data would fall within the range of the CERES measured TOA flux, while the AERONET based calculations would not.

2.13 Discussion

It is seen that for this particular case, satellite retrievals of optical depth using in situ measurements as inputs are higher than those using AERONET retrievals as inputs. For most cases the discrepancy is within algorithm or instrument uncertainty, but for large optical depths the absorption becomes important and the optical depths diverge substantially. The accuracy of the calculated broadband forcings do not seem correlated to accuracies in optical depth. These discrepancies and inconsistencies are discussed below.

Sensitivity studies demonstrate that for thick aerosol, single scattering albedo is the major factor in satellite retrievals of optical depth; it is also the only optical parameter

for which the difference between the AERONET and in situ data cannot be explained as the result of a column average. The differences between ω_o measured in situ and by AERONET may not be experimentally significant because the radii of error overlap (see also Reid *et al* [1998] or Russell *et al* [2002], both of which compound statistical and instrumental uncertainty), but the effect on radiative calculations based on these measurements are substantial. In order for the in situ ω_o value of 0.93 to match the AERONET value of 0.964, either the absorption must be cut in half or the scattering must be doubled. This halving/doubling trend is also evident in comparison of the AERONET climatological average of 0.975 for the PBL as compared to the in situ measurement of 0.95 [Dubovik *et al*, 2002; Hartley *et al*, 2000]. The case of scattering measurements being largely responsible for the variation in ω_o may be discounted: scattering comprises more than 90% of the optical depth, and many field campaigns with similar instrumentation have verified agreement in optical depth between aircraft in situ measurements and sun photometers using retrievals similar to that currently used by AERONET [Hegg *et al*, 1997; Remer *et al*, 1997; Russell *et al*, 1999; Ross *et al*, 1998; Fiebig *et al*, 2003; Kato *et al*, 2000, Haywood *et al*, 2003, Magi *et al* 2003]. Given the small absorption/scattering ratio, accuracy in scattering almost certainly falls within the maximum relative uncertainty in optical depth found in these comparisons.

Many column closure studies listed above claim success when measurements of optical depth agree within twenty percent and ω_o to within a few percent. With absorption typically a small fraction of scattering, the use of optical depth as an

evaluation of column closure places weak constraints on the absorption, which could vary by a factor of two while only affecting the optical depth and ω_o by a few percent. For use in satellite retrievals of thick plumes a higher confidence in the measurement of ω_o is required. It should be noted that the uncertainty for the MODIS aerosol retrieval is quoted as $\pm(0.2\tau + .05)$, which is 25% or less for optical depths above one. This study suggests that if the typical uncertainty in ω_o is $\pm(.02 \text{ to } .03)$ the uncertainty in optical depth may exceed that quoted for the MODIS retrieval once the optical depth becomes as large as 1.5 (see figure 2.20 or equation 2.4). However, given the differences between the MODIS algorithm and the one used in this paper, such a statement is not definitive (a description of the MODIS collection 4 algorithm is found in Remer *et al*, 2005).

Before turning to the absorption measurements themselves to explain discrepancies in single scattering albedo measurements, another option must be addressed. Perhaps the assumption of fixed inputs may be relaxed to allow variations in optical properties. Past studies have shown that the optical properties of smoke change with optical depth, even within the same plume [Dubovik *et al*, 2002; Wong and Li, 2002; Remer *et al* 1998]. For smoke the trend as the optical depth increases is for the single scattering albedo to increase while the asymmetry parameter decreases [Wong and Li, 2002]. These two parameters reinforce the effects of each other as seen by a satellite at TOA, resulting in a decrease in retrieved optical depth. Unfortunately the relationship between optical depth and optical properties as derived by Wong and Li [2002] is not a firm one, and is likely to vary with aerosol type and

ambient conditions. For this particular plume there is not yet sufficient information to draw relationships between measurements in different locations such as the AERONET sites and aircraft spirals. Further analysis of the aircraft data might determine the extent of changes in optical properties related to particle number density.

In situ absorption measurements remain as the primary factor in disagreements between optical depth retrievals via satellite and AERONET, despite the fact that the PSAP among the better instruments for the measurement of in situ absorption [Reid *et al*, 1999a] The measurements presented here are not likely to be outliers due to instrument operation: several in situ measurements of boundary layer aerosols in this area by systems equivalent to the one used in this paper indicate the same value of ω_o= 0.95 as seen in this paper [Hartley *et al*, 2000; Hegg *et al*, 1997], and since the absorption measurements were performed at ambient temperature no humidity corrections were required [Taubman *et al*, 2004].

The Bond calibration [1999] used for this and most other papers that use the PSAP is based on a single standard aerosol of absorptive hydrocarbon. Different aerosols may be expected to respond differently to heating effects or interaction with the filter. The Bond correction equations account for scattering effects based on the aerosol used for calibration (n = 1.67 at a wavelength of 0.55 microns). Since scattering is typically so much larger than absorption, this is not a negligible correction. The difference between the index of refraction of different aerosols and filter will affect scattering. The shape of the liquid component of many aerosols may also be distorted by contact

with the filter matrix. The calibration used a solid aerosol: aged smoke aerosol is assumed to be a solid core with a liquid sheath [Bundke *et al*, 2002]. LACE-98 recalibrated their PSAP following the Bond procedure but with a different standard aerosol [Bundke *et al*, 2002; Bond *et al*, 1999]; the agreement between their sun photometers and PSAP may have been the result.

Broadband forcing at the surface is mainly the result of scattering of short-wave radiation. Extrapolation of the scattering across the spectrum using the in situ measurements resulted in integrated flux values much closer to those measured by SURFRAD and CERES than did forcings using the AERONET optical properties. Since the forcing is an extrapolated calculation based on a retrieved optical depth, this represents a contradiction to the previous result that the satellite retrieved optical depth based on AERONET derived optical properties was closer to observations than in situ based retrievals. Though the AERONET retrievals should represent a consistent set of optical properties it is possible that the assumption of an equivalent monomodal size distribution instead of the indicated bimodal distribution is responsible for these differences. There is no simple algorithm to find a monomodal size distribution that is optically equivalent to a given bimodal distribution [Tanre and Kaufman, 1996]. Given the multiple measurements, assumptions, and calculational steps necessary for the forcing calculations it is possible that a systematic bias may favor the forcing calculations for higher optical depths. The CERES flux retrievals are based on assumed anisotropies in the radiation field stemming from broad categories of surface type, and the resulting uncertainties are difficult to quantify. A

few measurements are not sufficient to clearly establish a pattern, other than to state that comparisons between optical depth retrievals at a single wavelength may not imply similar results for broadband calculations based on the commonly available data gathering techniques used for this study.

2.14 Conclusions

This chapter investigated the properties and radiative effects of a smoke plume observed by aircraft in situ measurements coupled with a suite of remote sensing instruments. Absorptive heating calculated from these measurements indicate the smoke could have strengthened and maintained the subsidence inversion that sequestered the smoke at the top of the boundary layer.

Optical depth for this thick smoke plume was calculated from satellite reflectances combined with two sets of aerosol optical parameters: a complete set of AERONET retrieved optical properties and a complete set of optical properties derived from in situ measurements by aircraft. Two blended models used mixtures of AERONET and in situ measured optical properties in the smoke layer. The optical depth using AERONET ω_o with in situ derived scattering phase functions were 2% to 16% lower than the direct AERONET observations of optical depth, while retrievals using in situ measured absorption produced optical depths that were 22% to 43% larger than the

observations. Algorithm uncertainties increased with optical depth, although for the observed optical depths of ~2 the total uncertainty for most retrievals overlapped those of the other models.

The larger optical depths retrieved using in situ derived optical properties is due to the lower reflectivity of the assumed aerosol. This low reflection can be traced mainly to the absorption measurement, which is twice as large as that inferred from AERONET. Multiple scattering enhances the effects of variations in absorptivity [Bohren, 1987].

Broadband fluxes calculated from the in situ optical properties matched surface and TOA observations better (21% error) than those calculated from AERONET retrieved optical properties (33% error). In this calculation satellite retrieved optical depth was extrapolated across the solar spectrum based on the measured size distributions. This apparent inconsistency between which optical model best matched the observations for the optical depth versus the forcing retrievals may be due to compounding a larger set of measurements and assumptions into calculation of the forcing retrievals.

Achieving accuracy and consistency between different types of absorption measurement presents a significant challenge to the aerosol community. Satellites present the best way to track aerosol plumes, but unless the retrieval algorithms have accurate single scattering albedos, optical depth measurements (and hence forcing calculations) cannot be done with reasonable accuracy. Forcing calculations require a larger number of measurements (or extrapolation) and hence are even more susceptible to accuracy in optical properties. This situation is demonstrated by this study in which the differences between the optical properties measured in situ and by AERONET were

within instrumental uncertainty but the radiative calculations based upon these measurements varied widely. The sensitivity studies in this paper indicate that the uncertainty in optical depth is roughly proportional to the optical depth itself raised to the 5/2 power, so since most aerosol loading is rather low, this problem has attracted little past attention.

Chapter 3: Satellite Retrieval Biases

3.1 Cloud Drop Effective Radius

3.1.1 Introduction

Satellite studies of cloud microphysics are important for understanding precipitation processes [Rosenfeld and Lensky, 1998] and for climatic studies involving radiation transfer [Stephens, 2005]. Though satellites allow large-scale spatial studies with large data ensembles, they suffer from the limitations of viewing a three dimensional (3D) system from a single point perspective at pixel resolution. All remote sensing operational retrievals of cloud properties assume plane-parallel geometry with pixels that are radiatively independent of their neighbors [e.g., Iwabuchi and Hyasaka, 2002]. Here we examine application of the algorithm of Nakajima and King [1990] to cumulus clouds, allowing retrieval of cloud drop effective radius and optical thickness from reflectance in the visible and near infrared (NIR) spectral regions. Numerous field campaigns and studies in Amazonia [Kaufman and Fraser, 1997; Kaufman et al, 1998a; Kaufman et al, 2002; Koren et al, 2004] provide a well-characterized environment suitable for separating the real from the artificial, so this portion of the study avoids the less well investigated Canadian and Siberian regions in favor of the Amazon valley.

The above technique is best applied to stratus or stratocumulus clouds that are well approximated by plane-parallel geometry. Most cumulus clouds cannot be described as plane-parallel at the 1 km resolution typical of many satellite studies. A number of studies have addressed the effect inaccurate assumptions about cloud geometry have on

the operational retrievals of cloud properties [Loeb and Coakely, 1998; Coakely and Walsh, 2002;Varnai and Marshak, 2002a, 2002b; Marshak et al, 2006; Kato et al, 2007], and others have attempted to create retrievals that are fully 3D [Cornet et al, 2004; Iwabuchi and Hayasaka, 2003]. However, these techniques are not yet developed for use in operational retrievals.

Despite the possible inaccuracies, the plane-parallel approximations are still applied to cumulus clouds. A simple way to reduce 3D biases is to remove cloud edge pixels [Iwabuchi and Hayasaki, 2003] and maintain a view angle near nadir. Kaufman and Fraser [1997] applied this technique with the Nakajima-King algorithm to calculate the aerosol indirect effect of smoke on cloud effective radius in Brazil. In the same region, Feingold et al [2002] used a similar retrieval with a data analysis based on fractional rather than absolute changes in cloud and aerosol properties in order to cancel out systematic retrieval biases. Both studies employed a large data set to suppress random retrieval errors. Yet even if the reflectance variations due to cloud geometry are randomly distributed, the retrieval algorithms are nonlinear, and tend to skew any original symmetry in the data set [Marshak et al, 2006]. To further improve the accuracy of the preceding studies, it is necessary to explore the nature of 3D biases once the retrieval algorithms have been applied. Using a data set similar to those above, this paper investigates the effects that cloud geometry and relative orientations of sun and satellite have on the standard plane parallel retrievals of cloud drop effective radius, shedding light on the size and trend of these biases.

Though cloud optical thickness is retrieved simultaneously with effective radius,

its relationship to the variable illumination of 3D clouds (brighter pixels mimic higher optical thickness) has been the topic of several past studies [Loeb and Coakely, 1998; Varnai and Marshak,2002a, 200b]. Here we focus exclusively on retrievals of effective radius.

3.1.2 Theory: Shadowing, Illumination, and Scattering Angle

In a plane parallel approximation it is assumed that solar radiation uniformly illuminates the tops of the clouds, and that satellites only view this top-reflected radiation. In addition, it is assumed that the radiation emanating from one pixel is independent of its neighbors. As a result, shadowing and illumination are not accounted for. For a non plane parallel cloud the surface will experience varying amounts of shadow and illumination due to local orientation to the sun and/or obstruction by other parts of the cloud. Fig. 3.1a shows two neighboring cloud-filled pixels illuminated from the left. For the left cloud the side facing away from the sun is in shadow; this will be referred to as 'self-shadowing', and the amount of shadow viewed will depend on the location of the sensor relative to the sun. Note that this is a sub-pixel phenomenon stemming from geometrical features not resolved by satellite. A different type of shadowing is illustrated by the pixel on the right that is blocked from illumination by the pixel with higher cloud tops on the left; this will be referred to as 'cross shadowing'. So long as it is not blocked from view, cross shadowing of an individual pixel is independent of the sensor location. The amount of cross shadowing can be predicted from the resolved (pixel resolution) geometry of the clouds [Varni and Marshak,2002b]. In

practical terms, the difference between unresolved and resolved variability means the amount of self(cross) shadowing viewed by the satellite depends strongly(weakly) on the sensor location relative to the sun.

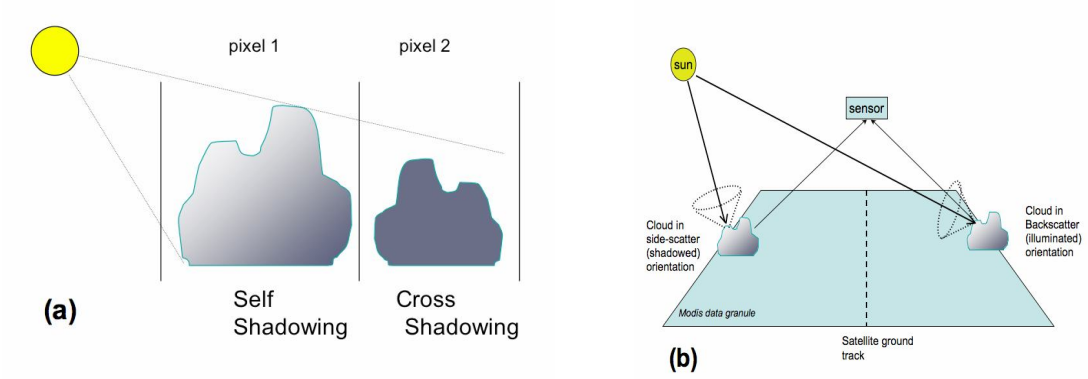

Fig. 3.1 Cloud shadowing. (a). Cartoon demonstrating the difference between self-shadowing and cross shadowing for cumulus clouds. (b). The relationship between sun and sensor locations and the division of data into backscatter and side-scatter geometries. The cones drawn in dotted lines indicate the range of angles within which the sun and satellite are considered to be in the backscatter geometry. If both vectors are not within the cone, the cloud is classified as being in the side-scatter geometry.

This paper is concerned primarily with self-shadowing. The distinction can be important: the only other observational studies we are aware of that investigated the effects of shadowing on cloud drop effective radius retrievals discussed cross shadowing only, and so ignored the sensor location [Varnai and Marshak, 2002b; Marshak et al, 2006]. Yet all pixels containing 3D clouds are subject to self-shadowing, while cross shadowing only occurs if neighboring pixels on the sunward side have higher cloud tops. The effects of self shadowing may be controlled by the scattering angle: if the sensor is in the direct backscatter location, it will view only illuminated portions of the clouds;

away from the backscatter position it will view increasingly shadowed portions. This is shown in Fig. 3.1b, for which the sensor will view shadowed or illuminated portions of clouds depending on the location of the sun and satellite relative to the pixel. For an ensemble of similar clouds the resulting 3D effects will vary smoothly between these positions.

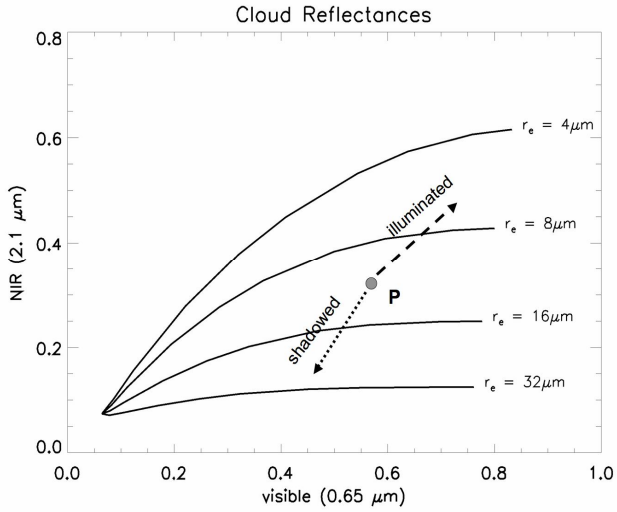

Fig. 3.2. Visible (0.65 μm) and NIR (2.1 μm) reflectance from plane-parallel clouds for various values of effective radius. The satellite is at nadir, the sun at a zenith of 25 degrees. The surface reflectance due to vegetation is assumed to be 0.05 in the visible and 0.08 in the NIR. Adapted from Varnai and Marshak [2002b].

The effects of shadowing and illumination on the effective radius (r_e) retrieval may be understood by reference to Fig.3. 2, which shows the Nakajima-King [1990] lookup table for visible (0.67 μm) and NIR (2.1 μm) reflectance from plane-parallel clouds. To create each contour, radiative transfer calculations were performed for clouds with the labeled values of effective radius over a vegetated surface, and the optical thickness was varied from 1 to 64 to produce the range of reflectances shown. Point P represents the reflectances expected for a plane-parallel cloud of given optical depth and effective

radius. If the local surface is tilted towards the sun, both reflectances will increase as shown by the dashed line (illumination), and the retrieved value of r_e decreases [Varnai and Marshak, 2002b]. If the local surface is tilted away from the sun, the reflectances will decrease (shadowing), and the NIR will decrease more than the visible due to absorption, as shown by the dotted line. This results in an increase of the retrieved value of r_e. Shadowing (illumination) thus causes overestimation (underestimation) of retrieved effective radius relative to the physically correct value.

The retrieval of r_e is non-linear, and for a random distribution of illumination and shadowing there is no reason to expect the errors to cancel out. For optically thick clouds (right side of Fig. 3.2), the values of r_e are nearly independent of the visible reflectance. For the nearly equally spaced values of NIR reflectance shown, the values of r_e form a geometrical sequence, and the average value of r_e across a random set of observations would likely be biased higher than that of the plane parallel case [Marshak et al, 2006]. Satellite viewing geometry is rarely random, so the distribution of scattering angles must be investigated for each ensemble separately.

3D clouds often do not uniformly fill a pixel. Because the vegetated surface is darker at 2.1 μm than a cloud, allowing partial filling of the "cloud pixel" with surface reflectance will increase the retrieved value of r_e [Rosenfeld et al, 2004]. A recent modeling study indicates that for small clouds contamination from a dark surface can dominate scattering angle effects, so that r_e is always overestimated [Kato et al, 2007]. The ensemble average geometry of shadowed and illuminated sets of clouds should be equivalent, so we assume surface contamination introduces a constant positive bias to all

data set averages with the same environmental parameters.

3.1.3 Data and Method

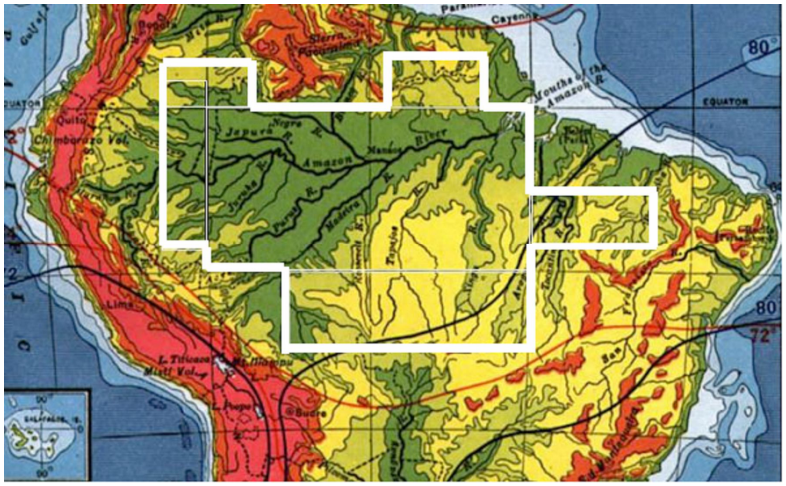

Fig. 3.3. The region used in this study.

An ideal demonstration of the effect of scattering angle on cloud effective radius retrievals would employ a multitude of sensors placed at different scattering angles looking at the same set of clouds. A more feasible alternative is a single sensor making an ensemble of observations of clouds in similar environmental conditions but with different scattering angles. Cloud variability produces noise in the observed data, but large ensembles reduce the signal to noise ratio if the environment is suitably constrained.

The MODIS Aqua satellite was used to observe clouds over the Amazon basin in August through October of 2002, an area of approximately 3 million square kilometers. Regions that border the coast or that correspond to topographical elevations above 500 m

were avoided, as shown in Fig. 3.3. The MODIS level 2 collection 4 operational products were used to retrieve all data used in this study [King et al, 2003; Platnick et al, 2003; Remer et al, 2005]. The 1 km cloud mask (MOD35) at the highest confidence level was employed to define the horizontal geometry of the cloud fields (average cloud size and cloudy fraction) in an 11x11 pixel box centered on each cloudy pixel. An automated selection algorithm based on these parameters was developed to select cloudy pixels corresponding to continental fair weather cumulus. The selection algorithm was tested by visual comparison to mixed cloud scenes.

The selection of cumulus based on horizontal geometry reduces the occurrence of aerosol misclassified as clouds [Brennan et al, 2005]. Cloudy pixels were eliminated with optical thickness below 3 or effective radius below 4 μm, or if they contained ice or mixed phases. Cirrus contamination was eliminated by use of the operational cloud top pressure product based on CO2 slicing. The surviving pixels were sorted into the following environmental bins based on satellite retrievals:

Total Column Precipitable Water - from 3 to 4 cm at 1 km resolution.

Aerosol Optical Depth – from 0.2 to 0.4 at 10 km resolution.

Brightness Temperature – from 298 to 270 K in 2 degree increments based on the 1 km resolution 11 μm emission. This is a proxy for cloud top altitude corresponding to a range of roughly 0.5 to 5 km above the surface.

Solar Zenith Angle – from 20 to 30 degrees with the sun in the west, corresponding to early afternoon.

The data were then subdivided into observations within 45 degrees of backscatter

(illuminated pixels) and more than 45 degrees from backscatter (shadowed pixels), creating roughly equal sample sizes for comparison with the full data set. The 1 km resolution effective radius data were averaged within each 2-degree temperature bin.

3.1.4. Analysis

Aircraft observations in Amazonia demonstrate that cloud drop effective radius is a very stable variable as a function of altitude throughout an ensemble of neighboring cumulus clouds in various stages of development [Freud et al, 2005]. An ensemble of cloud top properties thus reflects the development cycle of cumulus clouds. Since the microphysics of cumulus clouds is strongly correlated with vertical development, the data should be plotted in a manner that exhibits this dependence [Rosenfeld and Lensky, 2005; Koren et al, 2005]. Such a plot appears in Fig. 3.4a, with cloud top brightness temperature on the vertical and average effective radius on the horizontal. The solid line shows the full data set, with the illuminated subset plotted as a dashed line and the shadowed subset as a dotted line. The number of pixels averaged into each point is shown to the right (Fig. 3.4a'). As expected for an ensemble of moderately convective systems (fair weather cumulus), the number of cloud top pixels peaks at low altitude.

It is commonly assumed that the 3D nature of clouds is manifest by their edges, and so removal of edge pixels at 1 km resolution should substantially decrease the 3D biases. This is implemented in newer versions of the cloud product (Collection 5) [King et al, 2006]. Figs. 3.4b and 3.4b' are the same as Figs. 3.4a and 3.4a' with all edge pixels removed. The pattern is essentially the same in both plots, though all effective radius

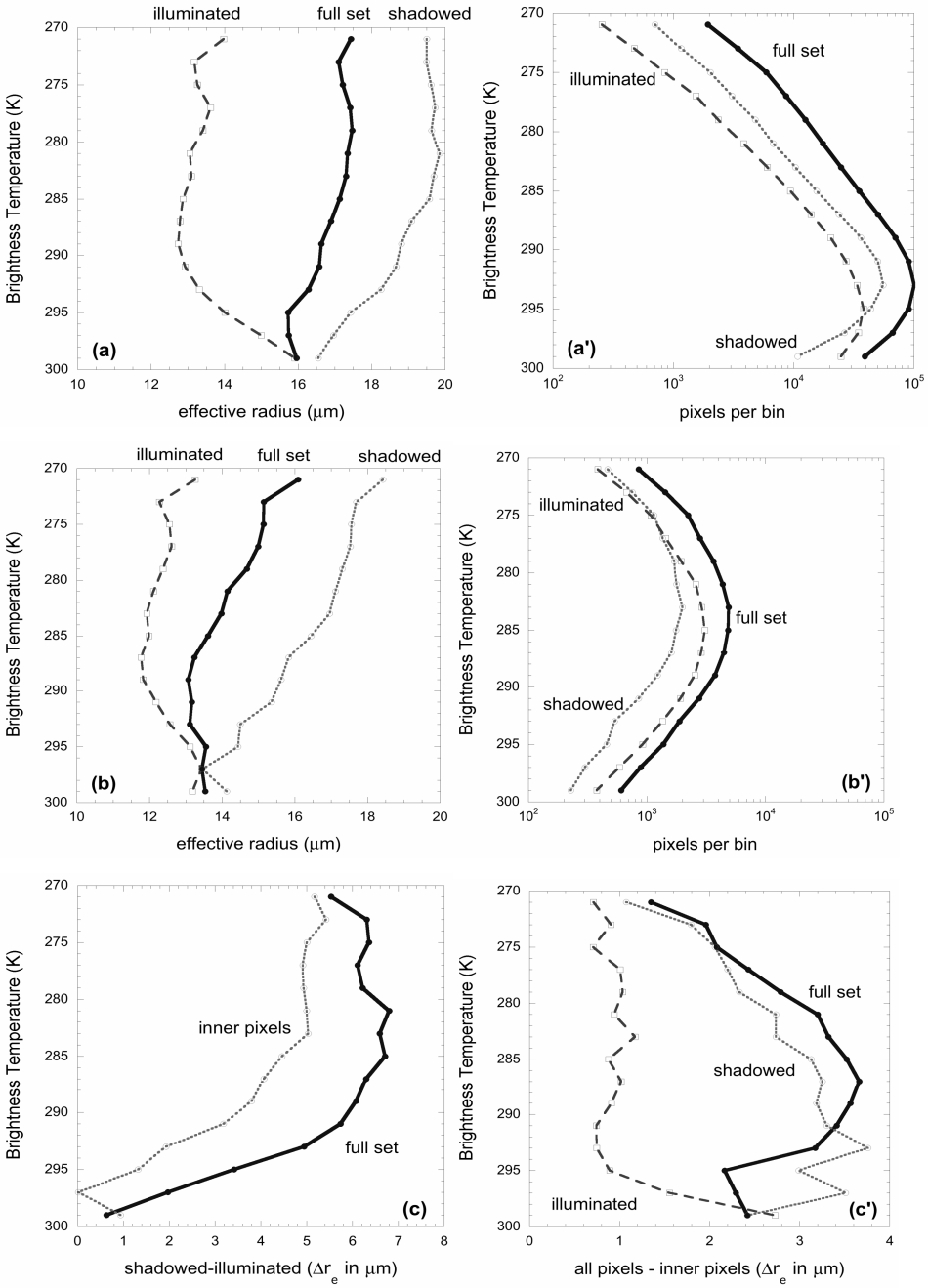

Fig. 3.4. Scattering angle and effective radius retrievals. The full data set of cloudy pixels is divided into backscatter (illuminated) and side-scatter (shadowed) subsets. The backscatter subset includes pixels within 45 degrees of direct backscatter, and the side-scatter subset includes all other pixels. (a) Plots of effective radius as a function of cloud top brightness temperature (left) with the number of pixels averaged into each bin (right). (b) The same as 4a but with edge pixels removed (inner pixel subset). (c) Comparisons between the full data set and the subset with edge pixels removed. Left: the difference between the average values of the shadowed and illuminated pixel subsets. The solid and dotted lines indicate the full and inner data sets. Right: the arithmetic difference between the average values of the two sets. The line styles are the same as in a,b.

values are smaller in Fig. 4b than in 4a. The reasons for the common pattern and the effect when edge pixels are removed will be discussed in turn.

The general pattern of the effective radius plots of 3.4a and 3.4b fit the theory of diagram 3.2. As expected the retrieved r_e is smaller or larger depending on whether it is illuminated or in shadow, and the difference between these two subsets may be taken as a measure of the 3D nature of the cumulus clouds. Plots of this 3D difference appear in Fig. 3.4c for the data sets of Figs. 3.4 a and b. Proceeding upwards from the shallowest clouds at the bottom of the plot, the shadowed and illuminated values of r_e diverge from a common point before saturating at a roughly fixed separation from each other at ~285 K. This saturation is likely due to clouds on average maintaining a constant vertical/horizontal aspect ratio as they grow, so that the directional reflectance function is independent of cloud size.

If this separation between scattering data represents 3D biases of the retrieval, the lower portion indicates a progressive decline of the 3D nature of cumulus clouds as they become shallower. This decline could occur for two reasons. First, clouds of low optical thickness cannot sustain the contrast between shadowed and illuminated portions. This is equivalent to moving point P to the far left of the lookup table of Fig. 3.2. The dotted and dashed lines would simply follow the contours of constant effective radius and there would be no difference between the shadowed and illuminated values of r_e. A second possibility is that 3D effects are expected to be greatest at cloud edges, and shallow clouds may have thin edges compared to the top surfaces. Reduction of the shadowing/illumination contrast does not necessarily mean the retrieved data is closer to

physical reality, for surface contamination becomes an important issue for shallow clouds [Rosenfeld et al, 2004].

The convergence of retrieved r_e with decreasing altitude for the shallow clouds of Figs. 3.4a and 3.4b represents variation in retrieval bias, but taken out of context the different slopes of the right and left branches may be mistaken for physical reality. Between the unstable retrieval and surface contamination issues, such shallow clouds should be treated with caution and may not be usable. On the other hand, if the saturation of the 3D biases for well-developed clouds is a universal tendency, these higher cloud tops may be used despite the bias if a consistent scattering geometry is maintained. The average retrieved effective radius would have an unknown but constant offset from the physically correct value.

Removal of cloud edge pixels is meant to reduce 3D bias on the pixel scale and surface contamination from partially filled pixels [Kato et al, 2007]. Their presence can be detected by the differing influence on retrieved r_e: 3D scattering effects cause over-estimation or underestimation depending on the scattering angle, while for all but the thinnest clouds surface contamination *always* causes overestimation for the 2.1 μm retrieval over vegetation [Rosenfeld et al, 2004]. Fig. 3.4c shows that the difference between shadowing and illumination retrievals in the saturated region decreases from 7 to 5 μm when edge pixels are removed. This reduction in bias may not be entirely due to 3D cloud scattering effects, for surface contamination is reduced as well. This can be seen by the fact that averages for both shadowed *and* illuminated subsets decrease when the edge pixels are removed.

Finally, Fig. 3.4c' shows the difference between averages of the full set and the interior subset of pixels for the various scattering geometries. Removal of edges has a much larger effect for the shadowing geometry, as might be predicted from the non-linear response discussed for Fig. 3.2. It is also possible that though cloud edges should always be darker than interior points in the shadowing geometry, they may not always be brighter in the illuminated geometry. As before, the different response of illuminated and shadowed data should not be interpreted purely as a cloud scattering effect, for the contribution from surface effects is a purely positive bias that will augment the shadowing bias while partially canceling out the negative bias from illumination. Even with a modeling study [Kato et al, 2007] it is not easy to say, when edge pixels are removed, what proportion of the changes in retrieval values are due to surface contamination versus 3D scattering effects. What we can say is that most of the difference between shadowed and illuminated retrievals remains when edge pixels are removed, and so is likely attributed to sub-pixel structure.

The saturation of the 3D biases for well developed clouds (Figs. 3.4 a and b) opens the possibility of a new analysis tool: data sets with the same amount of separation between shadowed and illuminated pixels might be assumed to have equivalent geometry, so may be compared because they are biased equally. It should be possible to develop theoretical correction factors based on scattering geometry for cloud ensembles that exhibit this saturation. A weighted average based on these correction factors would allow nearly all the data to be used instead of being limited to ensembles of fixed scattering geometry.

Cloud variability prevents a similar solution for individual scenes because such cloud ensembles are not large enough for statistical correction to work. Yet an understanding of 3D effects provides some guidance for experiment geometries that may minimize the bias. The goal is to find a viewing arrangement by which the visible and NIR reflectances from an actual cloud are the same as the theoretical reflectances from a plane parallel cloud with the same effective radius and optical thickness. For plane parallel clouds the brightest illumination occurs when the sun is directly overhead. The reflectance of 3D clouds will be reduced in this geometry due to light leakage through the sides. But for these clouds a bright spot will appear in the backscatter as the sun moves away from directly overhead. If the cloud is sufficiently thick it is possible that this bright spot could meet or exceed the reflectance of the equivalent plane parallel cloud despite light leakage. This means that so long as the solar zenith angle is sufficiently large and the clouds sufficiently thick, a correctly positioned satellite could measure reflectances that match the plane parallel equivalent. This position would be at or near backscatter, but the exact placement depends critically on the cloud geometry, optical thickness, and even the surface properties. Without knowledge of these quantities the biases cannot be removed, but may be standardized by requiring consistent experimental conditions across the various scenes in a study.

3.1.5 Conclusions for Section 1: Biases in Effective Radius from Cloud Geometry

Retrieval biases due to 3D geometry of clouds were investigated by reference to shadowing and illumination. When the satellite is in the backscatter position relative to

the sun it will only view illuminated portions of the cloud, and the effective radius retrieval will be smaller than the physically correct value. As the satellite moves away from the backscatter position the shadowed portions will dominate the field of view, and the retrieved effective radius will increase. For this study of cumulus clouds in Amazonia, a dividing line between shadowed and illuminated clouds was set at 45 degrees from backscatter to create roughly equal sized subsets. The difference between the averages of shadowed and illuminated subsets for developed clouds was roughly 7 μm.

The elimination of edge pixels at 1 km resolution only partially reduced 3D effects to a difference of 5 microns, indicating that sub pixel structure plays a dominant role in the contrast between shadowed and illuminated pixel retrievals. There is an additional effect: all effective radius averages decrease regardless of scattering angle, suggesting that surface contamination influences edge pixel retrievals nearly as strongly as 3D scattering effects.

For shallow clouds the retrieval averages between shadowed and illuminated pixels converged, representing a loss of 3D characteristics. This change in effective radius bias with vertical development could be mistaken for a physical trend. Such false trends might contaminate single scene studies as well as the type of ensemble study presented here. For well-developed clouds the difference between shadowed and illuminated data tends to saturate at a roughly constant value regardless of cloud top height.

It is recommended that the scattering geometry be explicitly controlled in future

studies. In general, comparisons should only be made between data ensembles that have similar cloud morphology and scattering geometry. Caution is warranted, therefore, when applying MODIS level 3 products to cumulus studies. If the saturation for well-developed clouds observed in this data set holds for other data sets, cloud morphology may prove to be less of a concern than scattering geometry. For such cases cumulus clouds have enough scale similarity that theoretical correction factors might be devised based on scattering angle alone. Such correction factors would only apply to large-scale statistics, not individual scenes.

The current cloud retrieval algorithms are best suited for stratocumulus studies, making collocated retrievals of environmental variables (such as aerosol and precipitable water, which require cloud-free pixels) problematic. This severely limits satellite studies of interactions between clouds and the environment. Further development along the lines indicated in this chapter is needed to adapt current data sets to the study of scattered cumulus.

3.2 Retrieval Biases due to Cloud-Aerosol Interactions

3.2.1 Introduction

In the previous section the aerosol optical depth (AOD) was held constant so that the effects of cloud shape on cloud retrievals could be isolated. But clouds can also have 3D

effects on aerosols retrievals, and aerosols may affect retrievals of 3D clouds. If the final goal is to understand the true physical nature of cloud-aerosol interactions, these retrieval biases must be studied and the consequences addressed.

To visualize these effects, aerosol loading must be exhibited in tandem with the r_e versus BT plots of Figure 3.4. For this the full data set is ordered according to aerosol loading, and split into 3 levels ('clean', 'normal', 'dirty') with equal numbers of points in each to ease statistical comparison. The colors blue, green and red are assigned to each level respectively, and plots of cloud properties or AOD as a function of BT (on the vertical) are created with the levels superimposed. This 3-color, 3-level in AOD plotting scheme will be used for the rest of this thesis.

3.2.2 Effects of 3D Cloud Structure on Aerosol Retrievals

Clouds scatter light through their sides, creating a 'light box' in which the atmosphere between them is exposed to greater illumination than if the clouds were not present. By use of 3D radiation transfer modeling, Wen et al [2007] showed that the apparent aerosol optical depth can be increased by this effect by up to 40% under typical conditions. For realistic aerosol amounts, approximately 80% of the extra reflectance came from Rayleigh scattering off the atmosphere in between the clouds, so the actual vertical location of the aerosol is not important.

Cloud geometry contributes to retrieval biases. Figure 3.5 plots cloud fraction and average cloudy pixel connectivity (see section 3.1.2) for the 3 aerosol levels. Illuminated and shadowed data are combined for this figure. Edge pixels have a lower

connectivity than inner pixels, so for fair weather cumulus with a size varying proportion of edge to inner pixels, average connectivity is a fair proxy for average cloud size.

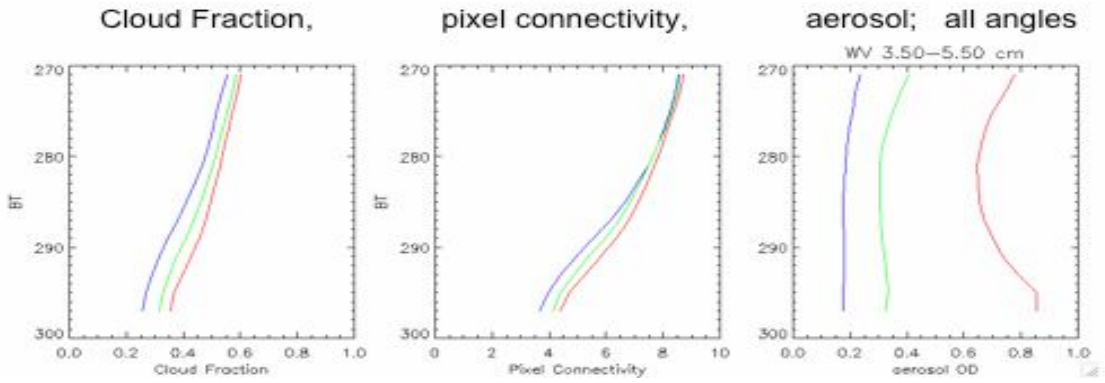

Figure 3.5: Average cloud fraction and connected cloudy pixels as a function of cloud top BT for a range of aerosol levels.

In figure 3.5 the local cloud fraction increases with local aerosol loading, contradicting the study of Koren et al [2004] showing that in the same region the overall cloud fraction decreases with aerosol loading. Though this may demonstrate different smoke/cloud interactions depending on meteorology [Yu et al, 2007], it may also represent retrieval bias. A possible demonstration that the retrieved AOD is being enhanced by the presence of clouds is portrayed in Figure 3.6. The AOD on the right is clearly lower where the clouds are missing in the visible image to the left. At each level an increase in AOD is associated with an increase in cloud fraction.

If the cloud illumination effect is in play, the retrieved AOD should respond to the amount of cloud development. Figure 3.7 has six pairs of plots; each pair has r_e on the left and AOD on the right. The AOD plot does not represent the vertical distribution of aerosol, but the amount of aerosol retrieved in the presence of clouds with the given

cloud top temperature. The top row is the full data set, for which the AOD exhibits a 'bow' shape with AOD higher for low and high cloud tops than for mid level cloud tops. The AOD increase in the vicinity of low-level clouds will be shown to be an artifact in

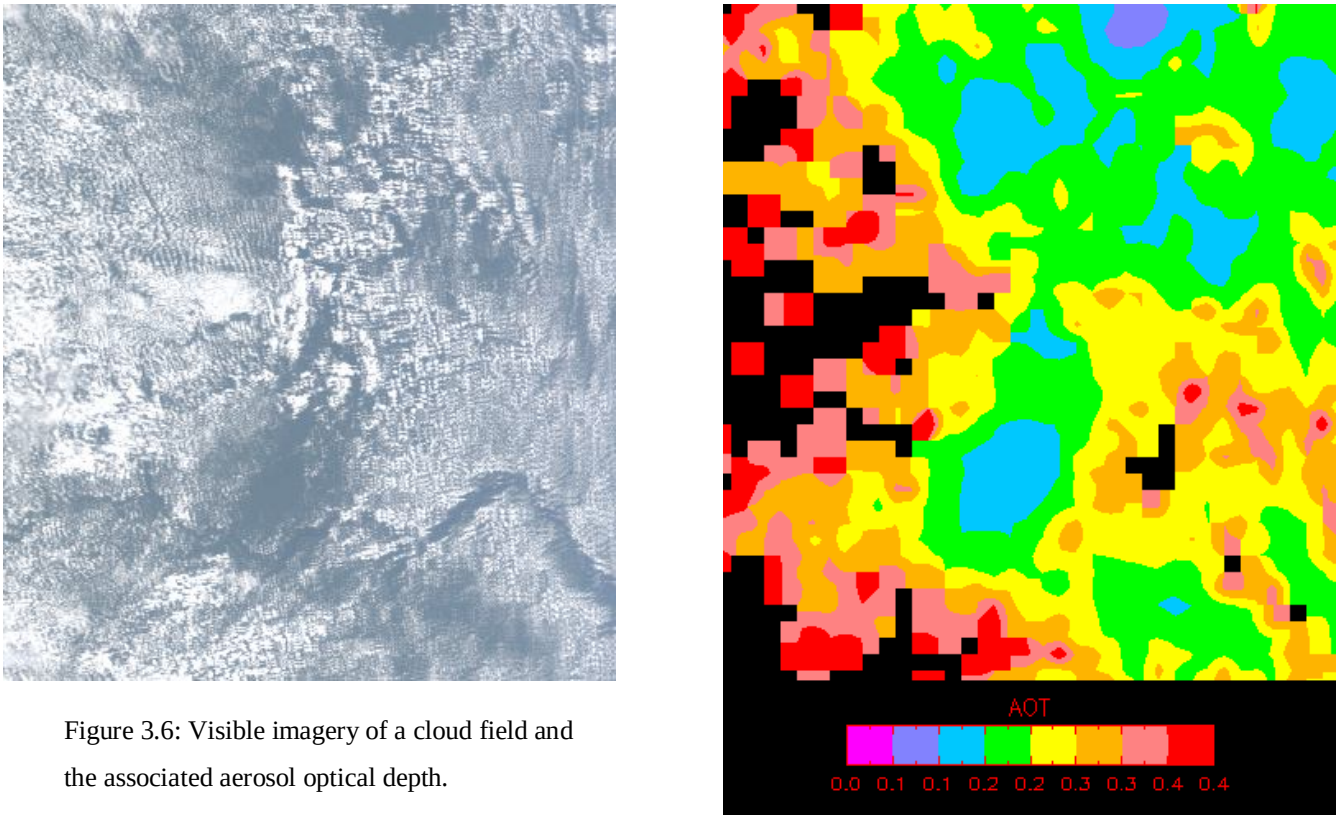

Figure 3.6: Visible imagery of a cloud field and the associated aerosol optical depth.

the next section; it can be removed by removing clouds with low optical thickness (COT). This is done in the middle row, for which all clouds have COT > 12. The bottom of the bow is reduced for the shadowed geometry, but average AOD still increases as clouds develop (top half). This is predicted by the illumination theory: as clouds develop the sides expand vertically, and the cloud fraction increases as well, filling in the sides of the 'light box' and increasing illumination. Though other explanations for the AOD behavior are possible (such as humidification), the agreement with this light-box theory is compelling.

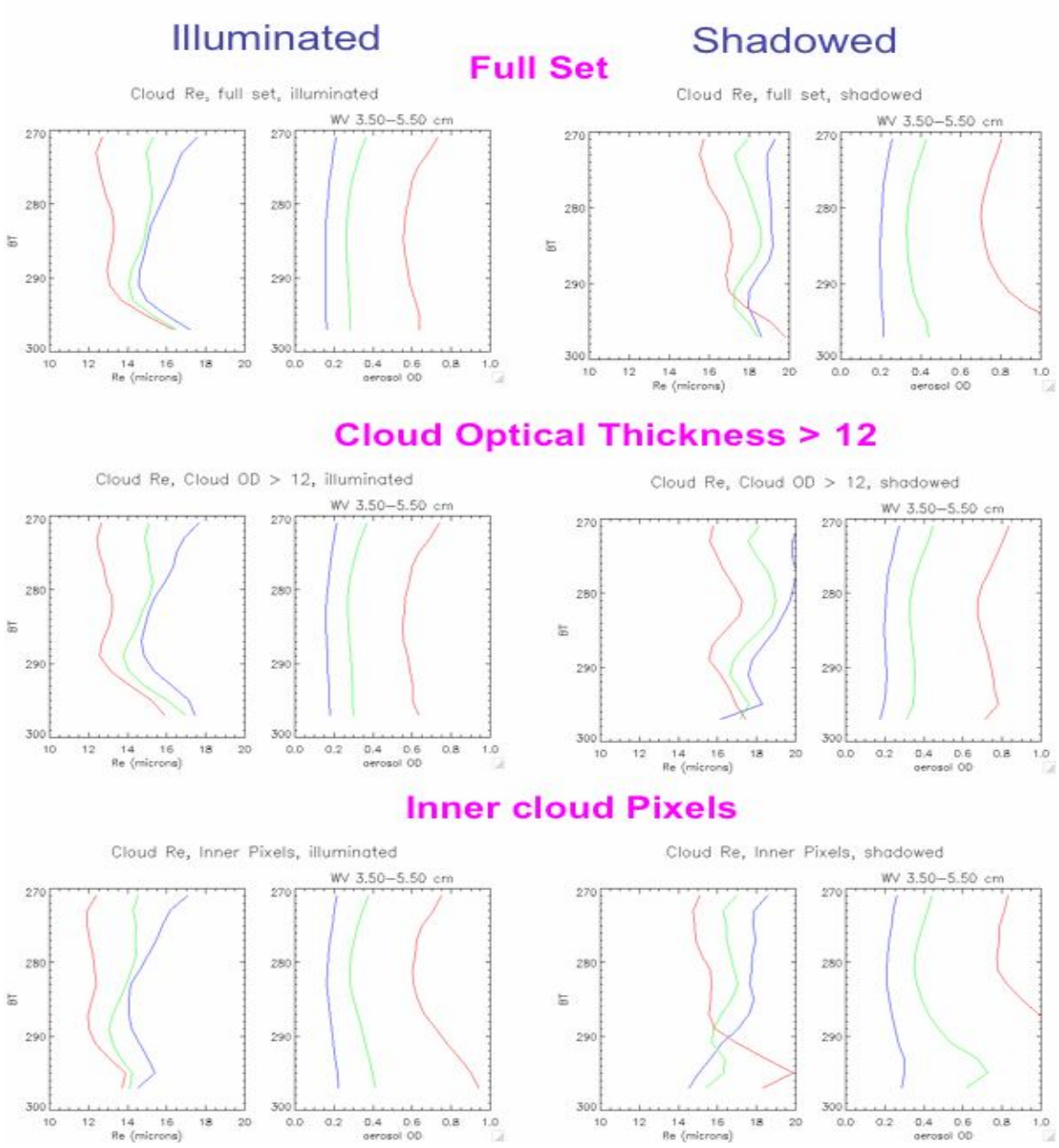

Figure 3.7: Retrieval averages grouped by aerosol terciles. Illuminated geometry on the left column refers to backscatter, shadowed to side scatter. Each row is a different filtering scheme.

3.2.3 *Aerosol Effects on Cloud Drop Effective Radius Retrieval Bias*

Rosenfeld et al [2004] offered demonstrations that surface contamination of cloudy pixels increases the retrieved effective radius. Brennan et al [2005] demonstrated

that aerosol could be mistaken for cloud, again increasing the retrieved effective radius. In this section radiative transfer calculations will demonstrate that both pure cases (cloud only versus aerosol only) tend to have a smaller effect than a mixture of aerosol and cloud together in a pixel. It must be emphasized that because cloud droplets favor forward scattering while the smaller aerosol particles produce more side and backscattering, when a cloud and an aerosol plume of equal optical depths are viewed by satellite, the aerosol plume will appear brighter. In this sense a small amount of aerosol can go a long way to confound remote sensing of clouds.

A qualitative understanding of how sub pixel cloud/aerosol mixing will affect the retrievals can be gained by returning to the lookup table plots for effective radius. Figure 3.8 has visible/NIR lookup tables for the shadowed and illuminated geometries. The green dots represent reflectances expected from a plane parallel cloud with r_e = 10 microns and COT of 4 for a solar zenith angle of 25 degrees. The point of zero optical thickness represents the surface reflectance. Cloud reflectances are greater for the shadowed geometry because the viewing angle cuts more diagonally through the cloud, increasing the apparent optical thickness. If the cloud only halfway fills the pixel, the reflectances will be reduced proportionally towards the surface reflectance point (green arrows). The addition of aerosol increases the visible reflectance but is transparent to the NIR (red arrows). Both result in an increase in retrieved effective radius, though due to the shape of the curves the bias is greater in the shadowed geometry. The 3D shape of clouds would augment this difference: brightening the reflectances and reducing the length of the green arrow in the illuminated geometry, while darkening and lengthening

the green arrow in the shadowed geometry.

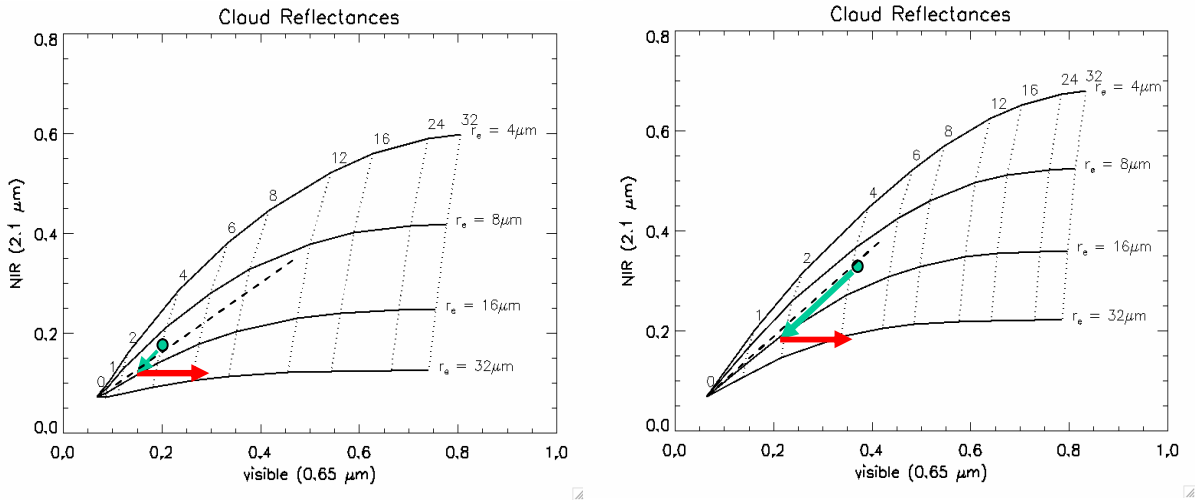

Back-scatter (illuminated) Side-scatter (shadowed)

Figure 3.8: Lookup tables to retrieve cloud optical thickness and effective radius from visible and NIR reflectances. The green arrows represent changes in pixel reflectance due to partial cloud filling; the red arrows represent how the addition of aerosol increases the reflectance of partially filled pixels.

It should be noted that for the thin clouds portrayed here, changing the cloud fraction (green arrows) has little effect unless coupled with aerosol brightening.

For plane parallel clouds quantitative calculations may be performed. A pixel is fractionally filled with cloud of a given optical thickness with droplet effective radius of 10 microns, and the remainder of the pixel is filled with aerosol with optical properties corresponding to the smoke encountered in chapter 2. For these calculations the matrix of combinations consists of AOD ranging from 0 to 2 in steps of 0.5, COT of 4 and 10, and cloud fraction ranging from 0 to 1 in steps of 0.1. Reflectances are calculated for 0.55 and 2.1 microns, then are used to simulate retrievals of cloud optical thickness and

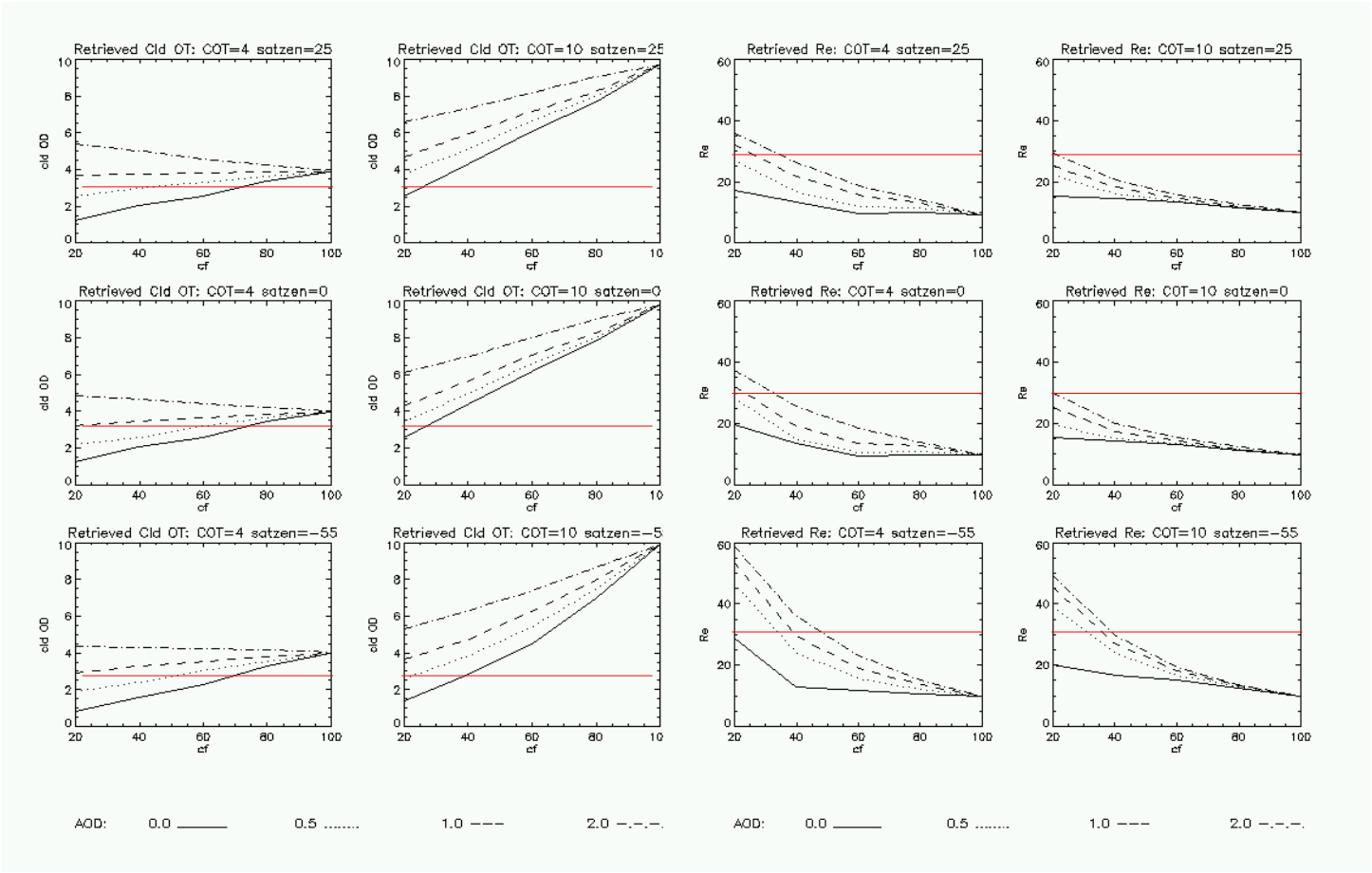

mixed retrievals of cloud OD mixed retrievals of effective radius

Figure 3.9: radiation transfer calculations to model retrievals of sub pixel aerosol/cloud mixtures.

Calculated cloud optical thickness appears on the left side of Figure 3.9, effective radius on the right. For each variable the left side corresponds to an actual COT of 4, the right to actual COT of 10, with r_e = 10 µm as above. The rows indicate viewing angle: the top row 25 degrees (backscatter or illuminated), the middle row 0 degrees, and the bottom row 55 degrees (shadowed). Within each axes the variable is plotted as a function of cloud fraction, with overlays for each aerosol level.

With no aerosol present the retrieved COT increases with pixel cloud fraction. The addition of aerosol brightens the scene and increases the apparent optical thickness. Depending on the view angle the addition of AOD ranging from 1 to 2 can mimic the visible reflectance of the cloud and make it appear as though it completely fills the pixel. A threshold of COT > 3 was used for this data set as an initial filter for small clouds, as shown by the red line. For an actual cloud optical thickness of 4, this is clearly too low a threshold: for AOD $\geq$ 1 the entire range of cloud pixel fractions are retained. For this range of AOD a higher threshold such as COT > 8 would be appropriate, as can be seen from the plots with actual COD =10.

Calculations for effective radius show that the presence of aerosol makes a large contribution to retrieval bias from partially filled pixels. For low optical depth clouds and high cloud pixel fractions the bias is nearly non-existent until aerosol is added to brighten the pixel, as demonstrated by the red arrows in Fig. 3.8. An upper retrieval threshold of 30 microns only serves to filter out low cloud pixel fractions in the shadowed geometry (bottom row).

If the cloud optical thickness threshold is set too low the effects on real data (which incorporates 3D shadowing) can be severe. Fig. 3.5 shows that the average cloud size (indicated by connectivity) drops for low altitude cloud tops, as would be expected based on cloud growth. Small clouds are primarily composed of edge pixels, so if the common filter of removing cloud edge pixels is applied, the low altitude cloud-top pixels that survive are likely from clouds whose apparent size has been enhanced by the

addition of aerosol masquerading as cloud.

The bottom row of Fig. 3.7 shows the results of edge pixel removal. The attention here is on the low clouds. As predicted for aerosol/cloud mixtures, retrieved r_e increases with aerosol loading; and the effect is larger in the shadowing geometry. The aerosol loading is also seen to increase dramatically, especially when shadowed. This is probably not an error in aerosol retrieval, but in the selection process. Small clouds surrounded by low AOD will likely not pass the COT threshold, so only those brightened enough by aerosol will be retained, and the AOD values with them. Note that when the COT threshold was set to 12 in the middle row, the low level increase in AOD largely disappears in the shadowed geometry where the aerosol brightening and retention of small clouds has the largest effect.

3.2.4 Conclusions for Section 2: Retrieval Bias involving Aerosol

Evidence has been presented that clouds affect aerosol retrievals through enhanced illumination. Conversely, aerosols affect cloud retrievals by sub-pixel mixing, simulating higher effective radius and optical thickness than would otherwise be seen. The selection of a high threshold for cloud optical thickness as a filtering mechanism serves a dual purpose. It reduces the effective radius retrieval bias due to sub-pixel cloud/aerosol mixtures. It also reduces the chances of low COT clouds in high AOD regions being retained while those in low AOD regions are rejected, thus biasing the AOD statistics.

Chapter 4: Comparisons between the Effects of Canadian and Siberian Forest Fire Smoke on Cloud Microphysics

4.1 Experiment Rationale

Cloud-aerosol interactions have been a topic of study ever since the classic paper of Twomey [1977] established a theoretical connection between cloud albedo and the cloud condensation nuclei (CCN) provided by aerosol. Traditionally clouds have been investigated by aircraft, but clouds vary so widely that individual case studies may not be representative of the regional system. Satellite retrievals of aerosol and cloud properties provide enough data that averaging may be applied to tame the inherent variability of cloud populations.

Approximately half of aerosolized black carbon in the global system is released as biomass burning [Ramanathan et al, 2001], so the climatic effects of smoke may be significant. Several previous studies have investigated the effects of Amazonian forest fire smoke on clouds in a statistical manner [Kaufman and Nakajima, 1993; Kaufman and Fraser, 1997; Feingold et al, 2001], all of which found a dependence between AOD and cloud drop effective radius that indicates a non-linear dependence between AOD and CCN. In the original paper on cloud-aerosol interactions, Twomey [1977] assumed a relation of the form $ccn \propto \tau_a^x$ between drop number (CCN) and aerosol optical depth τ_a. Feingold et al [2001] extended this analysis to include details of the aerosol size distribution and updraft velocity, though neither is retrievable by satellite. It has been

suggested that as the aerosol loading increases, competition for water vapor lowers the supersaturation level and fewer aerosol particles activate [Peng et al, 2002; Feingold et al, 2001], but a change in composition would also affect the CCN ratio [Rissman et al, 2004].

To our knowledge there have been no systematic satellite-based statistical studies of smoke/cloud interactions outside the Amazon basin, and no rigorously controlled comparison experiments between regions of differing aerosol but otherwise similar environments. By their very nature global satellite studies [Han et al, 2002] cannot control experiment geometry or the details of the environment; this must be done by a judicious selection of experiment locations. The MODIS land aerosol retrieval used in this study is designed to work best over dense vegetation. The vegetation map of Fig. 4.1 shows only two pairs of extra-tropical forested regions at the same latitudes: broadleaf forests in the Eastern U.S. versus Western Europe, and coniferous forest in Canada versus Russia/Siberia. The broadleaf forest regions are comparatively small and populated, so that forest fires are seldom allowed to burn unchecked. This study will therefore focus on the comparison between smoke/cloud interactions in the northern coniferous forests. Specifically, the Aerosol Indirect Effect (AIE) is defined here as the ratio of the fractional change of average cloud drop effective radius to the fractional change in aerosol optical depth, both accessible by satellite.

The preceding chapter demonstrated the need to keep the experiment geometry consistent across a series of measurements when studying cloud microphysics via satellite [Vant-Hull et al, 2007]. This helps ensure that measurement biases are

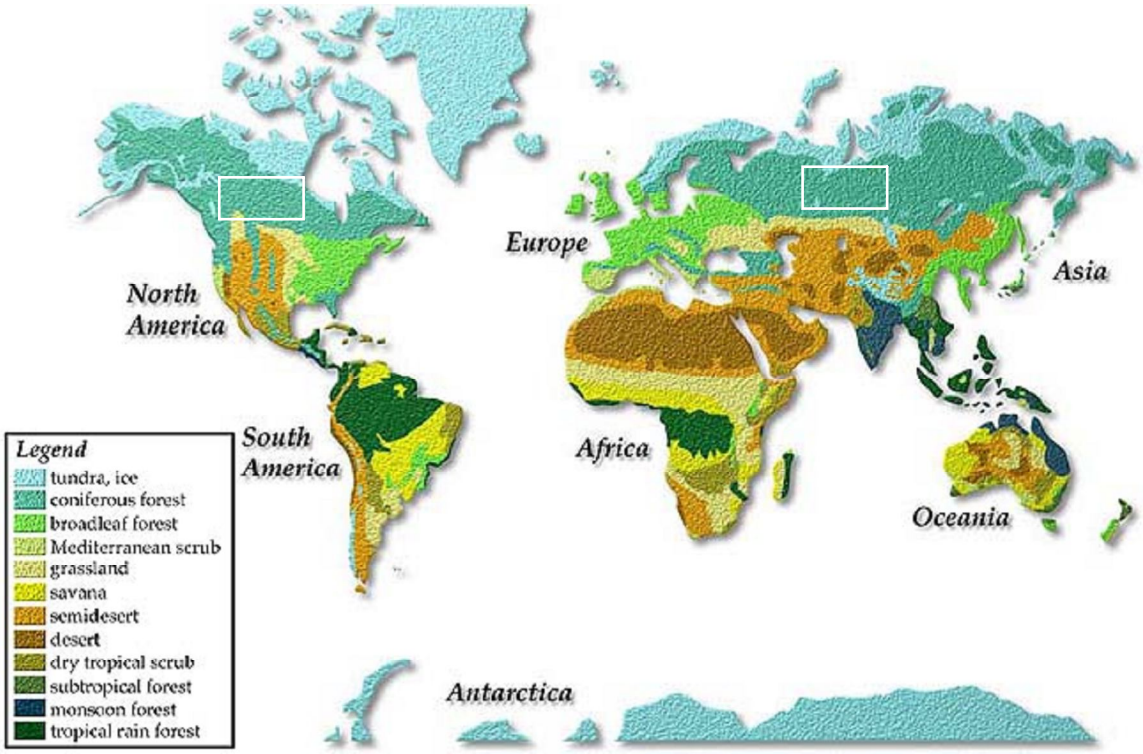

Figure 4.1: Global Biospheres and the selected regions.

consistent, but does not necessarily eliminate such biases. Under these conditions even if the values of *individual* measurements are questionable, comparisons *between* measurements remain meaningful. If two different regions are being compared, the only way to maintain constant angles for sun, cloud and satellite is if the regions are at the same latitude with the experiment conducted at the same local solar time. Cloud

geometry will vary with meteorology, but if the time period is long enough to allow sufficient variation, equivalent cloud sets can be formed by the selection of clouds that fall within pre-defined shape parameters. Finally, the ground cover in each region should be similar so that surface effects are comparable. The selection of Canadian and Siberian coniferous forest satisfies all these requirements.

Section 4.2 details how environmental variables are constrained so that the clouds in each region are forming under similar meteorological environments. Section 4.3 is a comparison of the aerosol in the two regions. The experiment methodology is outlined in section 4.4, and the results presented in section 4.5. This is followed by a discussion of the results with possible physical interpretations (section 4.6). The chapter ends with a summary of the first carefully controlled statistical comparison of the effects of smoke aerosol on cloud microphysics.

4.2 Regional Comparison of Environmental Factors that could Affect AIE

Both selected regions range from 54 to 64 degrees north latitude, with the southern limit chosen to correspond to the forest boundary of the sites. The Canadian region stretches from 115 to 95 degrees west longitude between the Rocky Mountains and the Hudson Bay, while the Siberian region stretches from 65 to 85 degrees east longitude across the lowlands east of the Ural Mountains. The surface altitudes in the Siberian

region vary from 10 to 250 m above sea level, with a mean of 100 m. The Canadian altitudes range from 20 to 1040 m above sea level, with a mean of 350 m.

Regional comparisons of other gridded variables that may affect the aerosol-microphysics relationship are shown in Fig. 4.2, in which Canadian values are plotted in green and Siberian values in red. These correspond to the locations of cloudy pixels selected for analysis, and are taken or calculated from MODIS Collection 5 level 2 products [Platnick et al, 2003] for cloud (MOD06) and water vapor (MOD05). Included in the cloud product are surface values of pressure and temperature re-gridded from NCEP analysis data. Further details on smoothing and co-location of satellite data appear in section 4.4. Dotted lines mark the constraints placed on each variable so that the experimental scenarios for each region are similar. The choice for the constraint on each variable is discussed in turn.

The plots on the left of Fig 4.2 represent some environmental variables that affect cloud development. Surface pressure (top left) depends both on meteorology and altitude. The distribution is quasi Gaussian in both regions, but the Canadian distribution is broadened by the wider range of surface altitudes and shifted to a lower average value. Under the assumption that the range of meteorology is similar in both regions, selection of similar sections of each pressure distribution should include roughly similar meteorological regimes. To preserve a large data set while avoiding the extremes in both cases, the feet were removed from both distributions at values approximately ¼ the full height. Surface temperature (middle left) was not broadened the same way as pressure, but the same rationale was applied to remove the feet of each distribution. Under this

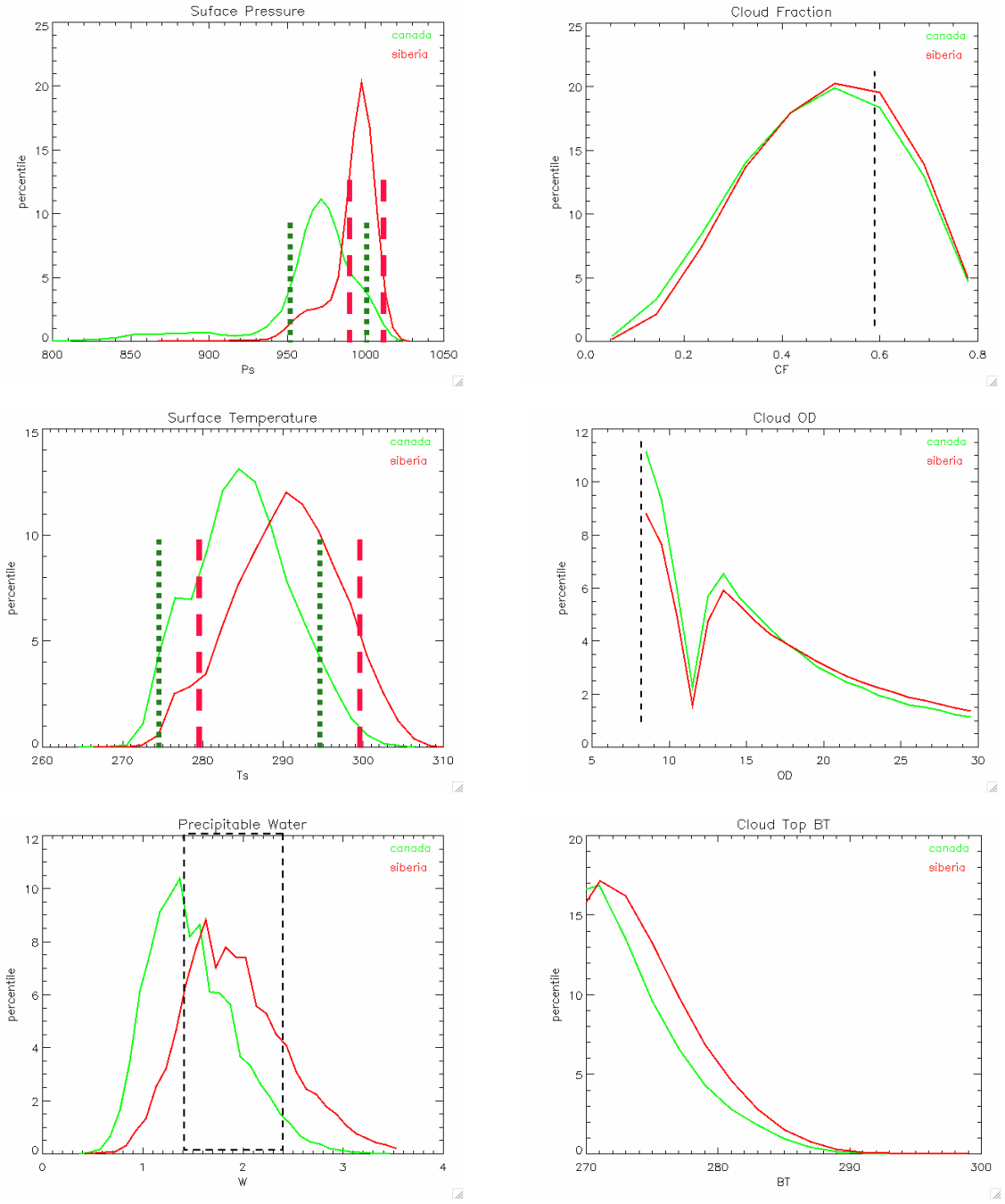

Figure 4.2: Histograms of variables that may influence the experiment. Constraints indicated by dotted lines.

assumption, selecting the middle ranges of surface pressure and temperature in each region should eliminate rare or extreme meteorological events that may skew the comparison. The selection of equivalent cloud geometries as described below should also serve to constrain the two data sets to similar meteorology.

The distribution of total precipitable water in Canada is shifted about 4 mm lower than in Siberia (lower left). This number is close to that expected from the average 250 m altitude change in the standard atmosphere, but the prevailing flow of air over the Rocky Mountains also plays a role in drying out the air mass from the Atlantic. Clouds arise from the water vapor supply, so total precipitable water places a strong constraint on the cloud lifecycle. Though TPW could be used to indicate meteorological regime in the same way as surface pressure and temperature, trials with varying TPW indicate that the clouds in the two regions tend to be similar only if the TPW has the same range in both regions. When the analysis was confined to low TPW, clouds with high tops tended to have droplets with smaller effective radius than lower cloud tops. This suggests that either the higher clouds are drying out or that they have rained out (using up TPW) and so are dissipating. In either case they are not in the development part of the cycle and the interpretation is not straightforward. To avoid this issue the TPW in both regions is confined to a single range that falls near the middle of the Siberian distribution but at the high end of the Canadian distribution. The number of cloudy pixels analyzed for Canada is thus smaller than for Siberia.

The plots to the right of Fig. 4.2 indicate cloud geometry. As shown in the previous

chapter, cloud geometry could affect cloud and aerosol retrievals. The cloud geometry also indicates cloud development and so may reflect environmental influences on the cloud system. The cloud fraction (top right) and optical thickness (middle right) distributions for the two regions are nearly identical (this dip in optical thickness at 10.5 is a retrieval artifact the cloud team is now working to correct). Note that the only constraint placed on optical thickness is the lower limit of 8. As part of the cumulus selection algorithm (described in the last chapter) applied to this data set the cloud fraction is directly limited to below 0.8, but indirect limits arise when the average cloud connectivity in a 11 pixel box surrounding each pixel is limited to 8 or below. These constraints are light enough that the strong similarity in cloud geometry between the two data sets implies equivalent cloud development processes. To further reduce the influence of clouds on the aerosol retrieval the cloud fraction is limited to below 0.6. The cloud top brightness temperatures (bottom right) for Canada are colder than for Siberia. Since Canada has lower precipitable water we might expect that on average the surface humidity is lower as well. This would lead to higher cloud bases, and if on average the clouds in Canada develop as much as in Siberia, the cloud tops would be higher and colder as well. The 270 K limit is the only constraint placed on BT.

The experiment geometry is most succinctly portrayed by the scattering angle of Fig. 4.3. Since sun and satellite are always on the same side of the clouds the scattering angle has been replaced by the sun-satellite angle defined as the angle between the satellite-pixel vector and direct backscatter. The small variation in sun-satellite angle between the two regions is due to variations of cloud distribution within the 10-degree latitude bins.

The solar zenith angle was fixed to between 33 and 48 degrees (afternoon only) and the satellite zenith angle constrained to less than 50 degrees. Since the sun-satellite angle was constrained to a range of 25 to 55 degrees, the view of clouds would range over the mostly sunlit portions while avoiding the direct backscatter geometry.

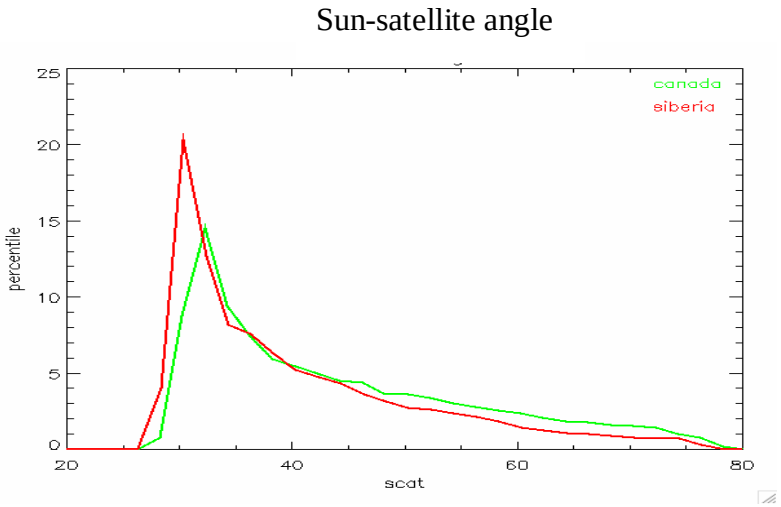

Figure 4.3: Histograms of sun-satellite angle for clouds in the two regions.

4.3 Regional Comparison of Aerosol

The aerosol in each of these sparsely populated regions is made up primarily of locally produced forest fire smoke mixed with smaller amounts of local anthropogenic emissions, biogenic aerosols, plus aerosol transported from outside the region. Most transport will come from the prevailing westerly winds, as the regions lay on the average boundary between the mid-latitude Ferrell cell and the Polar Hadley cell. Europe is roughly 60 degrees west and somewhat south of the Siberia region, while the same

distance to the west of the Canadian region is the northern Pacific. From this simple analysis we expect a stronger anthropogenic component in the Siberia Aerosol compared to Canada.

Results of the GOCART (GOddard Community Aerosol and Radiation Transfer [Chin et al, 2002]) model bear out the trend inferred above. In this model global circulation is calculated on a horizontal grid of 2.5x2 degrees with 30 vertical layers.

Aerosol sources for each grid cell are produced based on type: anthropogenic (sulfates, soot) according to estimated emissions; smoke from observed monthly hotspot count and intensity; dust and sea salt from the source region, wind speed, and soil moisture. Sedimentation and rainout is parameterized.

Fig. 4.4 shows histograms of modeled AOD for sulfates and smoke: indicated primarily by a combination of black and organic carbon. It should be noted that since the model distributes smoke evenly throughout each month the AOD will not exhibit the true

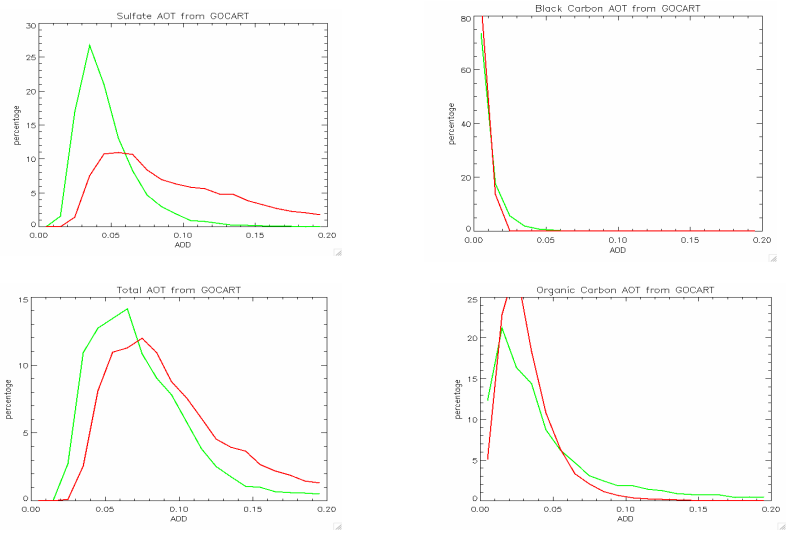

Figure 4.4: Histograms of aerosol components from the GOCART model. Canadian values are in green, Siberian in red. The left side shows sulfates and total AOD, the right side shows black and organic carbon, associated primarily with smoke.

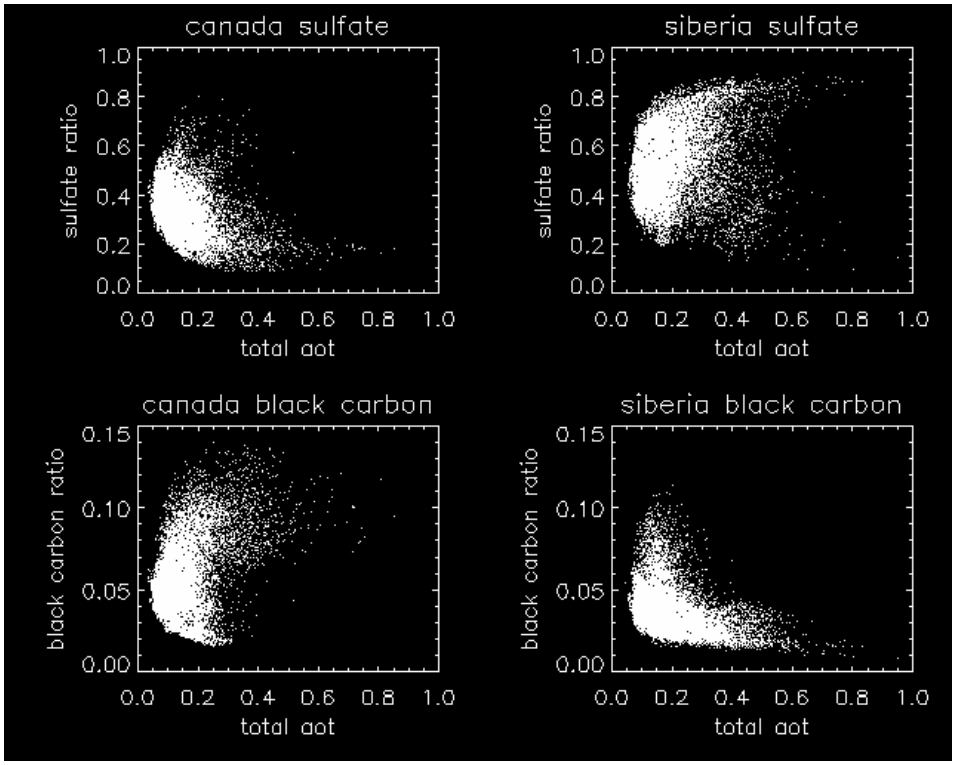

Figure 4.5: Scatter plots of component fractions versus total AOD.

range produced by the punctuated occurrence of actual fire hotspots. As expected the (primarily) anthropogenic sulfate distribution in Siberia peaks at a higher AOD and exhibits a more pronounced high AOD tail than that of Canada.

If the aerosol indirect effect depends on aerosol type, the variation of composition with aerosol loading is of interest. This can be indicated by a 'composition ratio' of the AOD due to one component divided by the total AOD. Such a plot is shown in Fig. 4.5 with composition ratios of sulfate and black carbon plotted as a function of the total AOD for each region. The model predicts that as AOD increases, the sulfate ratio in Siberia increases at the expense of black carbon; while in Canada the reverse is true. We should

thus expect an AIE response that varies differently with AOD in each region.

There are AERONET stations located near but not inside both regions that are capable of performing the Dubovik almancantur retrievals [Dubovik and King, 2000]. The Bratt's Lake station is 4 degrees south of the center of the Canadian region, while the Tomsk station is located right outside the southeast corner of the Siberian region. In light of the compositional variation predicted by GOCART, the retrieved properties are grouped by AOD. Figure 4.6 shows the size distributions as a function of AOD bin for the two regions during the 2003-2005 summer seasons, with slightly over 300 retrievals for Canada and over 200 for Siberia. To ease the comparison of shapes the graph is normalized by amplitude. There is no apparent variation of size distribution with AOD in Canada, consistent with fairly uniform smoke aerosol. The size increase with AOD in Siberia is expected from previous studies [Dubovik et al, 2002; Wong and Li, 2005; Eck et al 2002, 2003].

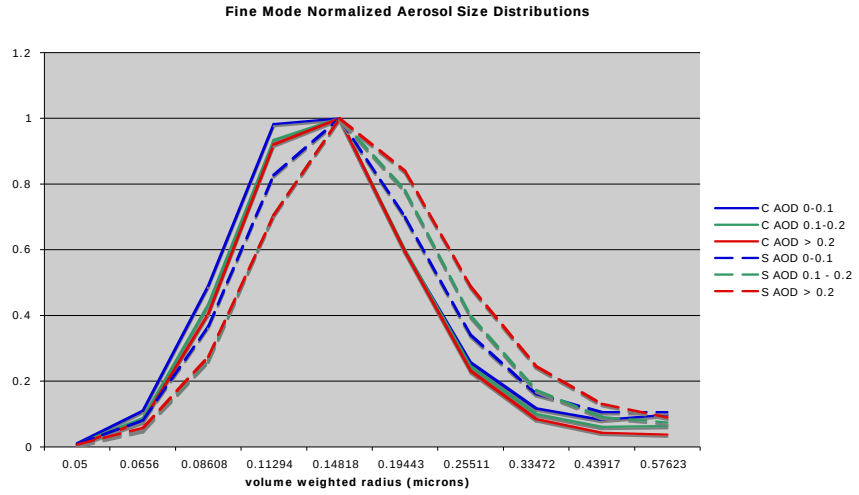

Figure 4.6: Fine mode size distributions from AERONET. Canadian values are solid lines, Siberian are dotted lines. The vertical axis is normalized to an amplitude of 1.

There were too few retrievals of single scattering albedo in Siberia to draw useful conclusions. Instead, in Figure 4.7 the optical depth absorption ratio (absorption/extinction) is plotted as a function of optical depth to indicate the aerosol composition [Koren and Kaufman, 2006]. Almucantar retrievals are known to become less accurate as optical depth increases [Dubovik et al, 2002], so the axis does not start at zero. The two aerosol look much the same as expected for smoke from similar forests, but at low AOD Siberia shows a cluster of low absorption, perhaps indicating the higher sulfate loading of Figs. 4.4 and 4.5.

The admittedly limited data and models available for these regions and time period do not produce a complete and consistent picture of the aerosol in each region, except for the much greater amount of sulfate in Siberia. We must trust the results of numerous field campaigns [Eck et al, 2002,2003; Reid and Hobbes, 1998] to fill in the details of aging smoke and possible compositional changes of aerosol with AOD.

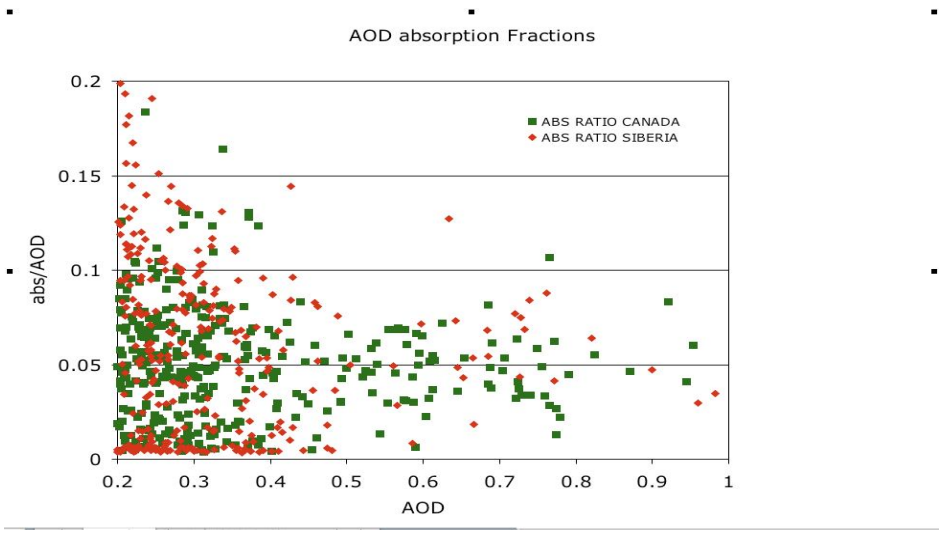

Figure 4.7: AERONET AOD absorption fraction (tau absorption)/(tau extinction) as a function of AOD for the two regions.

4.4 Experiment Methodology

All data here used for the calculation of Aerosol Indirect Effect (AIE) comes from the MODIS/Terra collection 5 atmosphere products [Platnick et al, 2003; Levy et al, 2007] with cloud top brightness temperatures (BT) calculated from the level 2 radiance product. Cloud drop effective radius (Re) and optical thickness (COT) are used at 1 km resolution, as is total column water vapor (TPW). The water vapor retrieved above cloudy pixels is removed, and the gaps filled by a 21-point running average that replaces cloudy pixel retrievals with surrounding clear air retrievals. AOD is rebinned from 10 km to 1 km resolution, then smoothed by an 11 point running average to fill gaps. Each cloudy pixel used in the analysis should thus have coincident values of Re, COT, BT, AOD, and TPW. Those that do not (from gaps due to large clouds, sunglint, etc) are deleted from the data ensemble. To be selected as a cloudy pixel the effective radius must fall between 4 and 29 microns with a minimum cloud optical thickness of 8. The brightness temperature must be greater than 270 K and identified as a water cloud by the quality assurance flag.

Only fair weather cumulus water clouds are used in the analysis. An automated algorithm selects cumulus clouds based on horizontal cloud geometry in an 11x11-pixel box centered on each cloudy pixel. A pixel is identified as cumulus if the local (inside the box) cloud fraction is less than 80% and on average each cloudy pixel has less than 7 cloudy neighbors. These numbers were inferred by visual inspection of the results of the algorithm, as shown by the examples in Fig. 4.8. For the remainder of this chapter the word ‘cloud’ shall imply ‘cumulus cloud’.

Cloud base cannot be located directly by passive satellite measurement. Since cloud top properties develop as the cloud grows, clouds in similar stages of development should be grouped for comparison. For a single scene this is easily done if the region is small enough for the lifting condensation level to be nearly constant. In such a case cloud tops may be grouped by their brightness temperature [Rosenfeld and Lensky,1997]. To create a larger ensemble by automated selection a proxy for cloud base must be employed. Each satellite image was divided into squares of 50 pixels on a side to model the local environment of a single-scene study. Within each square the cloudy pixel with the warmest brightness temperature and with $8 < COT < 13$ was selected as the 'base cloud', and all brightness temperatures were subtracted from this base temperature. If no cloud fell within this range of optical thickness, or if the total number of cloudy pixels in the square was less than 5, all values were rejected.

Rain is not likely to occur in developing cumulus water clouds with cloud drop effective radius below 14 microns where coalescence is hydrodynamically unfavorable [Ramanathan et al, 2001]. As shown below the average values of this data set were nearly always below this value, but given the uncertainties in the retrieval this is not a strong test. Additional screening is provided by the difference between the 2.1 and 3.7 μm retrievals. Photons of 3.7 μm wavelength are less penetrating than those of 2.1 μm wavelength. Developing clouds should thus have a positive difference between the two retrievals (3.7 – 2.1), while a negative difference may indicate either decaying clouds or the effects of raindrops falling deeper into the cloud [Chen and Chang, 2007]. Clouds with a negative difference between retrievals at these two wavelengths were screened out.

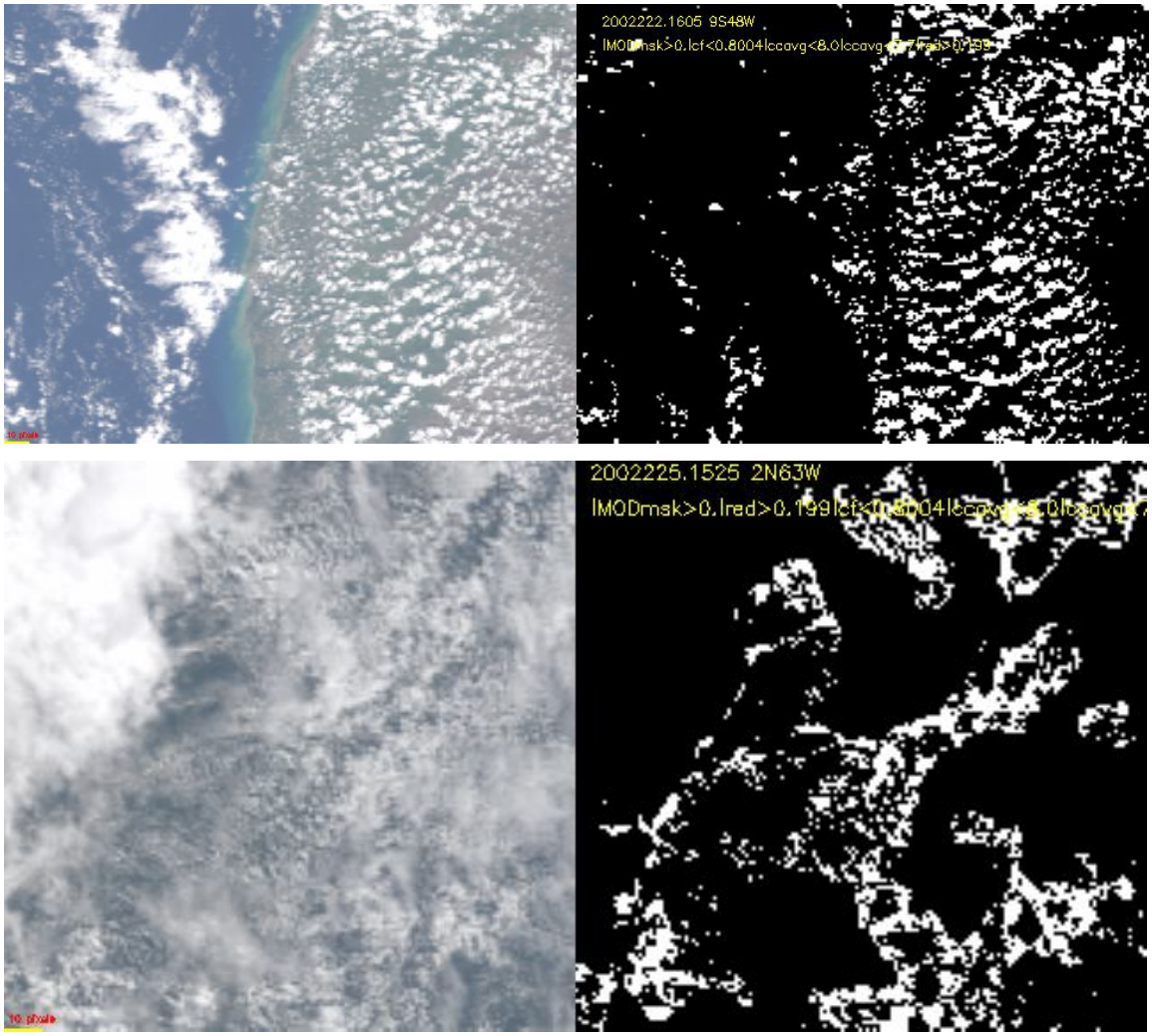

Figure 4.8: Two examples of cumulus selection based on cloud geometry, from Amazonia. The left side is the visible imagery, the right side shows cloud features that were identified as cumulus.

Pixels that survive the screening described above are binned into 2-degree increments of base cloud temperature difference. Within each temperature bin the data is sorted by ascending AOD, then split into three equal sized terciles so that the number statistics for

each tercile is the same (see section 3.2). Within each temperature/aerosol bin, averages and standard deviations are calculated for cloud drop effective radius, cloud optical thickness, cloudy pixel connectivity and cloud fraction.

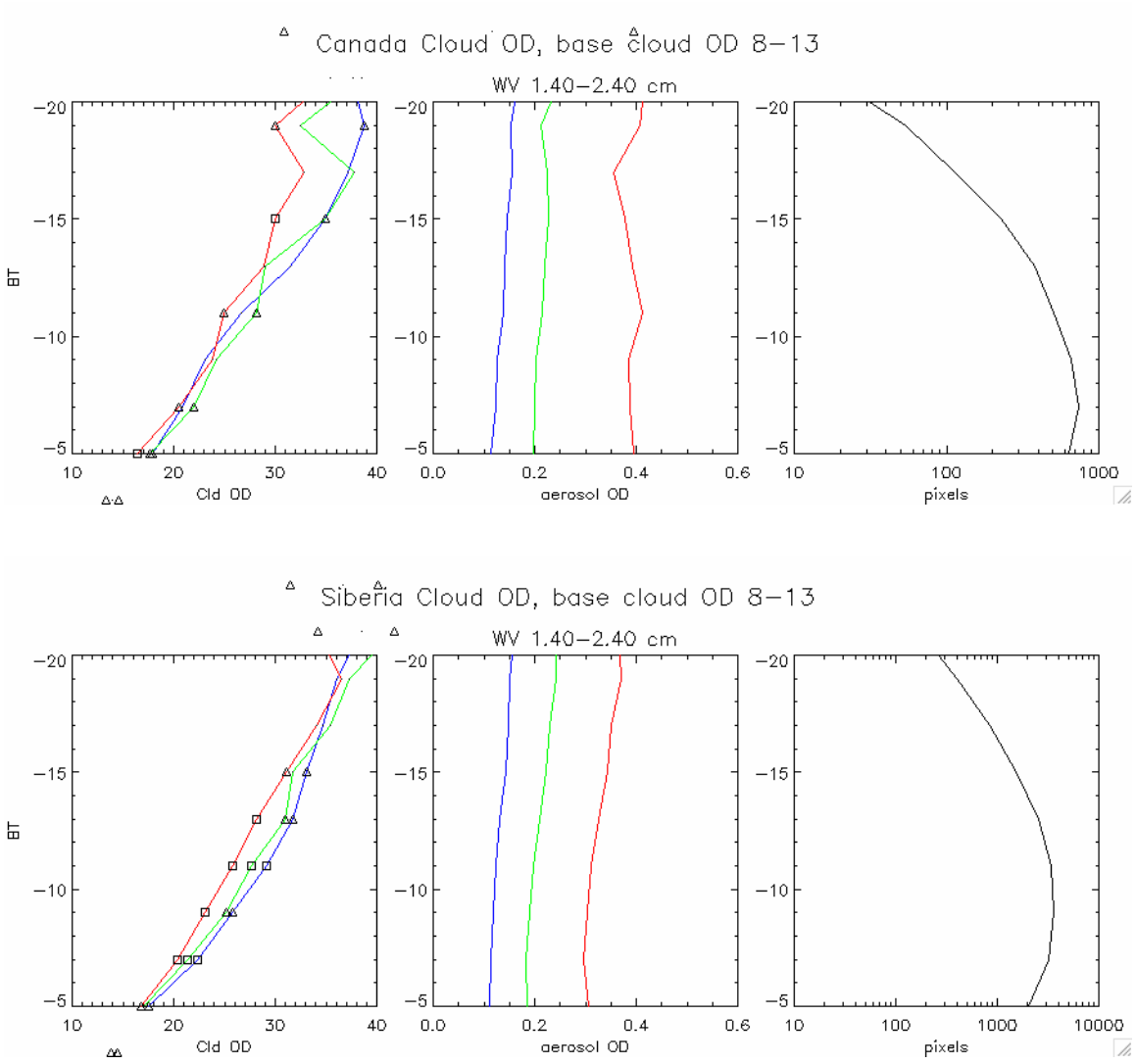

Figure 4.9: Cloud optical thickness, regional aerosol, and pixel counts for Canada and Siberia. Blue represents the lowest or 'clean' aerosol tercile, green the middle or 'normal' aerosol tercile, and red the highest or 'dirty' tercile.

4.5 Results

Figure 4.9 displays averaged cloud optical thickness as a function of cloud top brightness temperature for the three aerosol bins. On the left plot cloud top BT is plotted on the vertical to represent altitude, with optical thickness increasing with altitude. Each aerosol tercile is represented by a different color; with 'clean' in blue, 'normal' in green, and 'dirty' in red. The averaged value of the aerosol surrounding the clouds in each tercile and cloud top BT bin is plotted in the middle. The number of pixels in each bin is plotted to the right.

A Student 'T' test is applied to the data in the aerosol bins at each temperature level to determine if the differences between the averages are significant or not. A square is plotted if an average is significantly different from both the other aerosol levels at the 95% confidence level. A triangle is plotted if the difference is only significant from one other bin, and there is no mark if the averages cannot be statistically distinguished.

The smooth increase of average optical thickness with altitude above the base clouds is an indication that the cloud development cycle has been correctly captured by this technique. The cloud drop effective radius is not as strongly coupled to altitude, and so is more sensitive to sample size. The effective radius plots behaved erratically for low and high values of BT temperature difference, where the number of samples per bin is low. For this reason the effective radius plots were trimmed to between 5 and 20 degrees below the base cloud brightness temperatures as shown by the dotted lines.

Figure 4.10 displays a plot of cloud drop effective radius on the left according to the same scheme as Fig. 4.9, except that a measure of aerosol indirect effect (AIE) is shown to the right. AIE is calculated according to the following formula [Feingold et al, 2002]:

$$AIE = -\frac{d\ln(r_e)}{d\ln(\tau_a)} \Rightarrow -\frac{(\Delta r_e / \bar{r}_e)}{(\Delta \tau_a / \bar{\tau}_a)} \qquad r_e = \text{effective radius; } \tau_a = \text{AOD} \qquad (4.1)$$

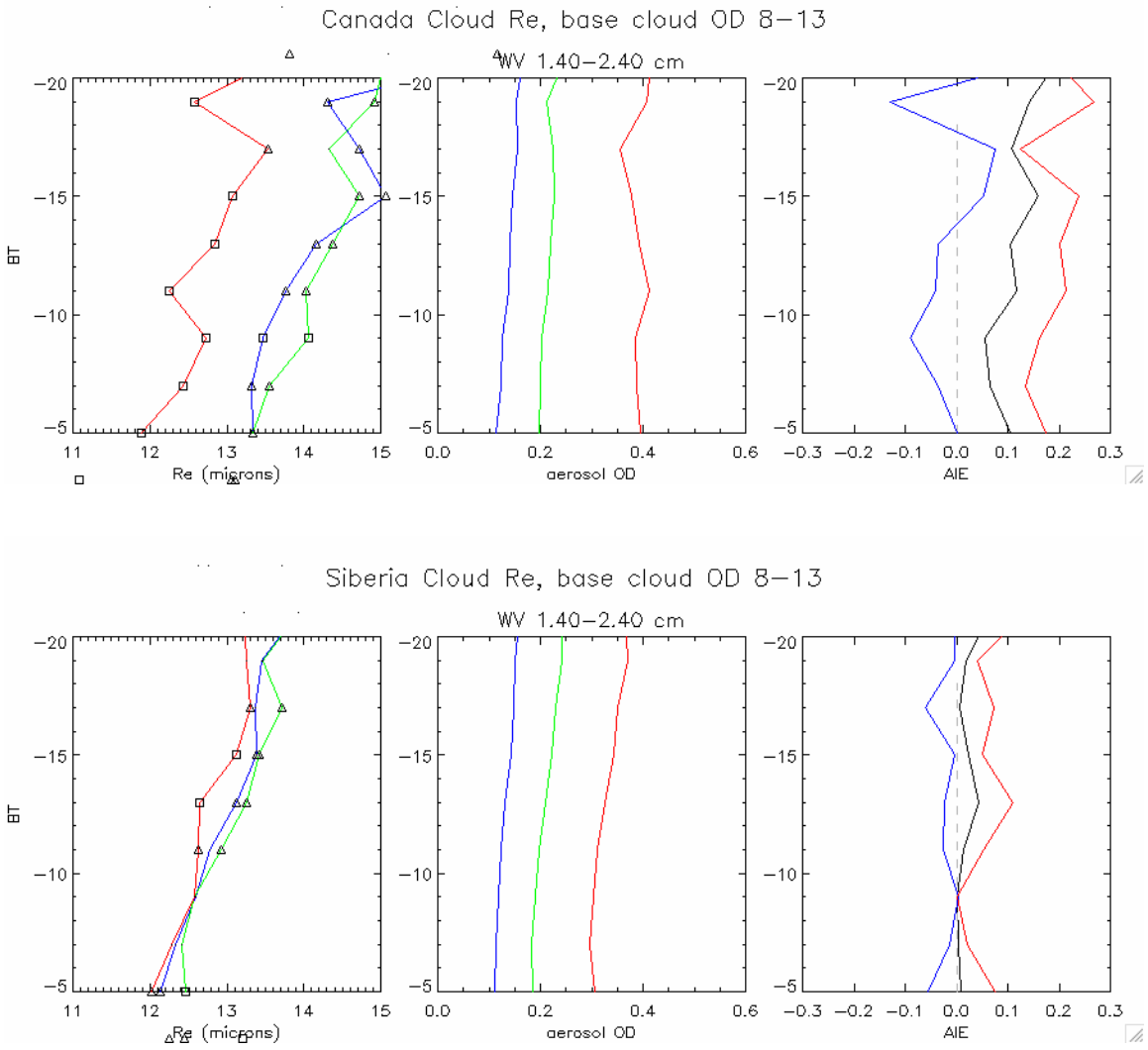

Figure 4.10: Cloud droplet effective radius, local aerosol, and AIE. The color scheme represents aerosol levels (terciles) as in Fig. 4.9.

The deltas represent a difference between two aerosol terciles, and the overbars indicate the average of the two terciles. The AIE calculated between the clean and dirty bins is shown in black, with that between the clean and normal bins indicated by blue and between the normal and dirty bin in red. The negative sign is meant to produce a positive AIE if r_e decreases with AOD as expected on physical grounds. As shown below the separation between the blue and red AIE lines is an indication of how the aerosol CCN activity changes with AOD.

4.6 Discussion and Interpretation

The plots of the preceding section give rise to one question concerning cloud optical thickness and aerosols, and three concerning cloud drop effective radius and aerosol loading:

Aerosols and cloud optical thickness:

Why does the average cloud optical thickness decrease with aerosol loading?

Aerosols and cloud drop effective radius:

1. Why for each aerosol level is the effective radius always lower in Canada than in

Siberia?

2. Why is AIE greater in Canada than in Siberia?
3. Why does the AIE tend to increase with AOD in both regions, and why should this tendency be so much smaller in Siberia?

Each of the above questions will be discussed in turn.

4.6.1 Aerosols and cloud optical thickness

If the total liquid water in a cloud remained constant and the number of CCN increased with AOD, we could expect the cloud optical depth to increase with AOD [Twomey, 1977]. In practice total liquid water is difficult to measure accurately by satellite because it depends on the product of two other derived quantities: optical thickness and effective radius (and the cloud top effective radius is not representative of the entire cloud). Multiplication would compound the errors of each, so such calculations are best avoided.

Yet the observed decrease of optical depth with AOD suggests that the liquid water *must* be decreasing as well [Brenguier et al, 2003]. A grudging calculation of the total liquid water will demonstrate this point. We start by assuming the effective radius varies linearly from near zero at cloud base (2 to 4 μm would be better [Peng et al, 2002], but complicates the algebra) to its value at cloud top: the average is just half the cloud top

value. For all except the smallest drops we have geometrical scattering, so the optical depth is just equal to the total cross sectional area, doubled to account for diffraction by Babinet's principle. Multiplication yields:

$$(\bar{r}_e) \bullet (\tau_c) = \left(\frac{1}{2} \frac{\sum r_i^3}{\sum r_i^2} \right) \bullet \left(2\pi \sum r_i^2 \right) = \pi \sum r_i^3 \qquad (4.2)$$

Multiplying this expression by 4/3 will convert it to a sum of drop volumes, or total liquid water. Note that this equation differs from most derivations that assume the cloud top radius is the average radius for the cloud.

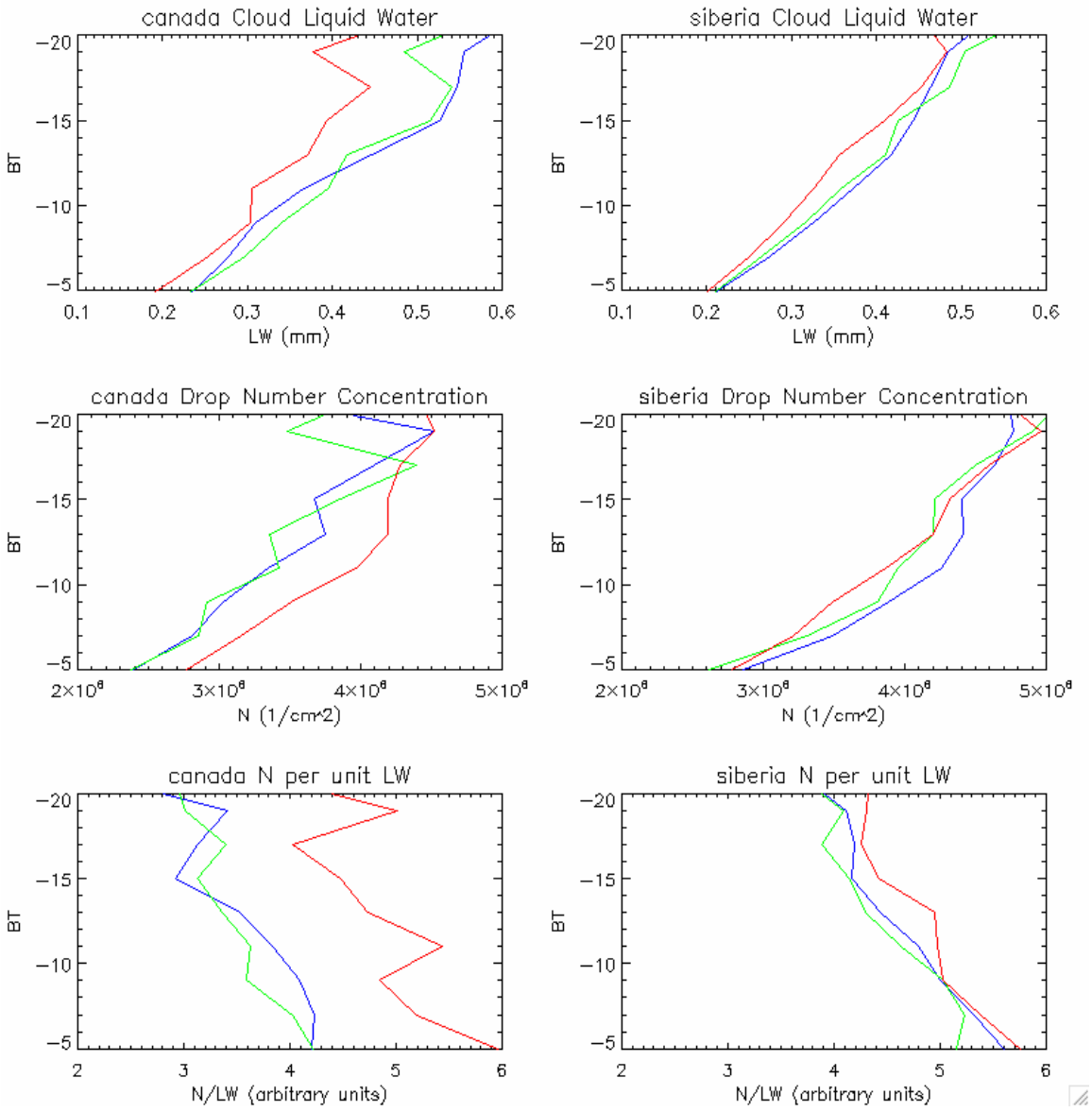

Figure 4.11: calculations of cloud liquid water (LW) and droplet concentration (N) for the three aerosol levels:.blue='clean', green='normal', red='dirty'.

Figure 4.11 shows the calculated liquid water (LW, top row) and drop number concentration (N, middle row) for the 3 aerosol bins as a function of BT difference from

local base clouds. These were calculated according to the following formulas:

$$LW = \tfrac{4}{3} r_e \bullet \tau_c \qquad \text{and} \qquad N \approx \frac{LW}{\tfrac{4}{3}\pi \cdot r_e^3} = \frac{\tau_c}{\pi \cdot r_e^2} \tag{4.3}$$

Even if the cloud property measurements were exact, the number density calculation would be only an estimate: effective radius is an area-weighted radius, and cubing it will not reproduce the average volume per drop. Yet in the spirit of comparing equally biased retrievals between regions the number density is retained. The bottom row of Fig. 4.11 normalizes N by dividing by the LW.

In both regions the cloud LW decreases for the highest level of aerosol loading, thus decreasing optical depth. There are three possible explanations for the LW variation with AOD: the same meteorology or transport mechanism causes both to vary in opposite directions with no direct connection between them; the aerosol affects the liquid water of the cloud; or the cloud liquid water affects the aerosol.

For the first case an unstable atmosphere promotes cloud growth as well as aerosol ventilation. Haze is most likely in a stable environment often found in high-pressure systems. Scatter plots of surface pressure and AOD for Siberia (which has little variation in topography) have indicated very little correlation between the two variables, weakening this argument. Even if this mechanism occurs, other transport scenarios would do the opposite: moisture convergence may be accompanied by aerosol convergence; increased water vapor could increase AOD by humidification. Figure 4.12 shows a

positive correlation between total column water vapor (TPW) and AOD, yet a similar plot between TPW and cloud optical depth showed no relationship, and the eventual connection between sources of AOD and cloud LW is therefore unlikely.

Aerosol could affect the cloud liquid water in two ways. Absorbing aerosol warms the atmosphere while cooling the surface, thus stabilizing the column and inhibiting cloud growth [Taubman et al, 2004; Koren et al, 2004]. The tendency of cloud fraction to decrease with smoke in Amazonia supports this mechanism [Koren] though there have been no comparable studies in the boreal regions. Such studies are difficult because satellites cannot retrieve aerosol simultaneously with cloud, so will not be reproduced here. Aerosol could also inhibit transpiration by decreasing insolation of the surface [Koren et al, 2004]. Scatter plots of AOD and total precipitable water instead show a weak positive correlation (Fig. 4.12). Though this may be due to aerosol humidification the relationship still contradicts the aerosol/transpiration effect.

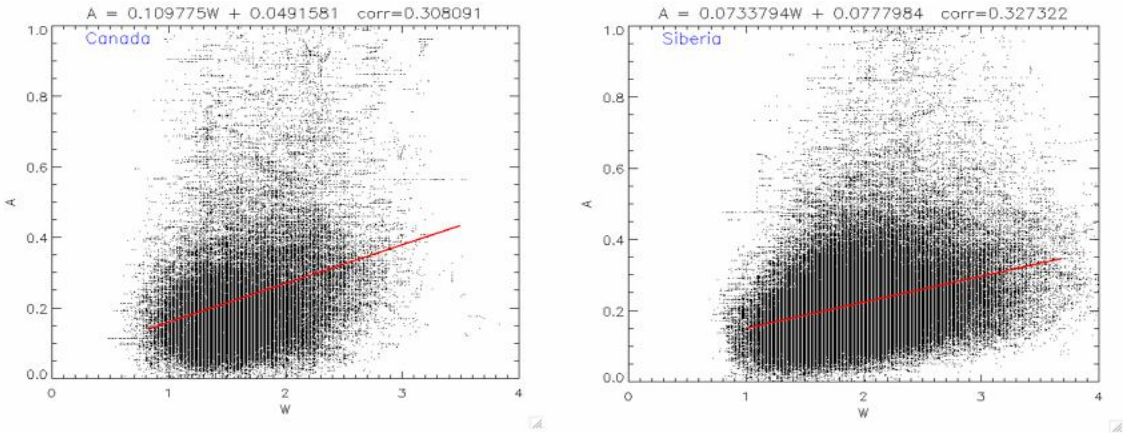

Figure 12: Scatter plots of AOD (vertical) versus Total Precipitable Water (horizontal) for each region.

The last possibility is that cloud LW affects the aerosol. But all physical mechanisms that relate cloud development (LW) to AOD result in positive correlations : cloud processing would humidify and increase AOD [Andreae et al, 2004], cloud illumination of aerosol would increase the retrieved amount, and precipitation would decrease AOD and LW together. In summary, it is most likely that the smoke decreases the cloud LW (and hence the optical depth) by creating more dynamically stable temperature profiles.

The middle row of Fig. 4.11 shows number concentration (N) for entire clouds, so the plots naturally decrease with altitude above the base cloud temperature. N increases for the dirty aerosol case in Canada, but seems to decrease slightly if at all for an increase in aerosol loading in Siberia. The variation in N is not proportional to AOD. For Canada only the dirty aerosol bin exhibits an increase in N, and it's only ~10% as compared to a 2 to 4 times increase in aerosol loading for the lower bins. For clarity the effects of variable liquid water can be divided out, as done in the bottom of Fig. 4.11. The Canadian droplet concentration now exhibits an even more dramatic increase in droplet concentration for the highest aerosol tercile, underlining the change in aerosol character with AOD. In Siberia the drop number concentration is now seen to increase slightly with aerosol loading as expected. For both regions the difference between the lower AOD terciles may be viewed as insignificant (see Fig. 4.10), and for Siberia there may be no significant difference even if the dirty tercile is included.

4.6.2 A Regional Aerosol/CCN Model

Rather than attempt to fit the patterns of the preceding section to an equation such as those suggested by Twomey [1977] or Feingold [2001], the number concentration behavior will be used to create a qualitative model for the regional aerosol as described in section 4.3. This model will be applied to all sections that follow. Anthropogenic emissions are fairly consistent, so sulfates may be viewed as part of the steady state background aerosol. The larger excursions in AOD will be due to intermittent smoke events [Roberts et al, 2003; Eck et al, 2003], modeled as being relatively inactive CCN compared to sulfates. Though laboratory and in situ experiments suggest smoke may be highly effective CCN [Navakov and Corrigan, 1996; Roberts et al, 2002], the relevant quantity is CCN per unit AOD; and the measurements of chapter 2 demonstrated that the effective radius of the particles in an aged Canadian smoke plume may be 3 times larger than the ambient aerosol. This may be an extreme case, but surveys generally show smoke particles to be somewhat larger than sulfate aerosol [Dubovik et al, 2002]. Since AOD is proportional to the optical cross sectional area, even if smoke particles have the same CCN activity as sulfate, the ratio of CCN to AOD will be many times smaller (the size difference is amplified as the radius/wavelength ratio moves into the Rayleigh regime).

In the simplest version of the model the CCN activity of smoke does not change with AOD. For Canada the background sulfate component is so low that the addition of the relatively inactive smoke (in terms of CCN per unit AOD) can still make a substantial change in the amount of CCN, while in Siberia the background CCN is so high that

smoke has a lesser effect. In a more sophisticated model the smoke characteristics vary with AOD, changing both its CCN activity and optical depth as the particles aggregate [O'Neill et al, 2005]. The solute concentration therefore changes very little while the curvature becomes less, increasing the CCN activity. This simple active/inactive two-component model with concentration-dependant growth will now be applied to explain interactions between aerosol and cloud drop effective radius.

4.6.3 Aerosols and Cloud Drop Effective Radius

The three observations about the effects of aerosols on cloud microstructure arising from Fig. 4.10 can be addressed in order of increasing complexity. The first is the general observation that for all aerosol levels the cloud drop effective radius is smaller in Siberia than in Canada. This may be explained two different ways. The first refers to the greater sulfate presence in Siberia: a higher concentration of CCN at all AOD levels means smaller droplets. Note that this explanation requires fresh smoke particles to be relatively inefficient CCN, despite laboratory evidence to the contrary [Navakov and Corrigan, 1996]. These experiments, however, did not make direct comparison to sulfate aerosols. The second explanation for smaller effective radius in Siberia refers to the size distributions of Fig. 4.6: since in Siberia the aerosol are generally larger, the increase in CCN activity due to the curvature effect (see Appendix C) accounts for more numerous, smaller drops.

4.6.4 Models for Variation in AIE

The second observation is that AIE is generally higher in Canada, despite a lower level of CCN. The meaning of AIE must be explored before its response to aerosol can be explained. For each altitude in Fig. 4.12 the liquid water is seen to vary by 20% or less across the aerosol bins, which would result in a change in r_e of only about 6%. To get a rough idea of what is happening we will take LW to be constant at each altitude, so that by setting the drop number equal to the number of CCN we get by combination with equation 4.1:

$$CCN = \frac{LW}{\frac{4\pi}{3} r_e^3} \quad \text{so that} \quad \frac{d\ln(CCN)}{d\ln(\tau_a)} = -3\frac{d\ln(r_e)}{d\ln(\tau_a)} = 3AIE \qquad (4.4)$$

Because of the logarithmic derivatives, AIE represents the fractional change of CCN per change in AOD. The actual ratio of CCN to AOD will cancel, and all linear proportionalities between the two variables will produce the same AIE. Only relationships that are not simple proportionalities (such as Twomey's $ccn \propto \tau_a^x$ model) will produce changes in AIE. If Twomey's power law is inserted into equation 4.4, AIE = x/3, which equals 1/3 for a simple CCN/AOD ratio regardless of the proportionality constant.

The first model to explain the variation of AIE with AOD is based on the change

of the aerosol size distribution with optical depth, due most likely to aggregation of smoke particles [O'Neill et al, 2004]. As the average particle size increases, the CCN activity increases (appendix C). Twomey's power law accommodates a change in CCN activity. The ratio of CCN per unit optical depth may change with AOD:

$$\frac{CCN}{\tau_a} = \frac{C(\tau_a)^x}{\tau_a} = C(\tau_a)^{x-1} \qquad (4.5)$$

For a direct proportionality (x=1) the ratio is a constant value of C, indicating no change in the CCN activity. Values other than x=1 represents a change in aerosol character with AOD. The current observation, that AIE increases with AOD, means x does as well, demonstrating that Twomey's phenomenological model with a constant exponent does not match the smoke aerosol. This is hardly surprising. But there is a difficulty with assigning changing CCN activity purely to changes in size of the aerosol particles: this change in aerosol size with AOD is more pronounced in Siberia (Figure 4.6), whereas we see a greater change in AIE with AOD in Canada.

In the two-component model for Siberia the number of CCN depends primarily on the sulfate supply, which is assumed to be relatively constant compared to the large variations in smoke. If this Siberian aerosol model is correct, CCN will not change much with AOD, and a low AIE is expected. In Canada the base number of CCN is lower, allowing smoke to make a larger contribution to percentage change in total CCN. The resulting Canadian AIE is higher than in Siberia even though the average CCN/AOD ratio is lower.

A simple mathematical model will demonstrate these concepts. The sulfate

component of AOD is assumed to be constant for each region, with a high CCN activity (represented by the proportionality constants). Variation in total AOD is due to the addition of smoke, which has a low CCN activity per unit AOD. The total AOD is the sum of the two components, as is the total CCN.

Sulfates: $CCN = k_a \tau_a$ Smoke: $CCN = k_s \tau_s$

Total: $CCN = k_a \tau_a + k_s \tau_s = k_a \tau_a + k_s(\tau_{total} - \tau_a)$

Where the subscripts 'a' and 's' stand for anthropogenic and smoke aerosol, k represents the ratio between CCN and AOD, and τ is the AOD. Given the particle size distributions for smoke and ambient aerosol found in Canada (Table 2.3), Mie calculations show that the contribution to optical depth per particle is about 200 times greater for smoke, providing a very low CCN/AOD ratio. But since smoke particles are larger, they should have a greater CCN activity. This particular smoke plume/ambient combination may not be representative of those further north, where the sizes of the two aerosol components are likely to be closer together [Dubovik et al, 2002]. For demonstration purposes we assign $k_a = 1$, $k_s = 0.2$. Based on GOCART model results (Fig. 4.4) we assume constant sulfate AOD values of 0.045 for Canada and 0.09 for Siberia. Upon assuming [clean, normal, dirty] AOD values of [0.1, 0.2, 0.3] and using the difference form of equation 4.1 to reproduce the AIE of Fig. 4.10, the following table results:

AOD	Canada	Siberia
low	0.15	0.10
middle	0.17	0.12
high	0.19	0.14

Table 4.1 Simple 2-Component Model for AIE

As intended this model produces an AIE that is larger for Canada than for Siberia. AIE also increases with AOD, an attribute seen in the data of Fig. 4.10 that prompted the final question at the beginning of this discussion section. This variation indicates that the dependence of CCN on AOD is not a simple proportionality; a relationship broken by the addition of a constant sulfate term to the smoke CCN.

But this model has not reproduced a key observation of Fig. 4.10. For both Canada and Siberia, the AIE for low AOD is effectively zero. This indicates no change in CCN for variations on the low end of AOD. (In fact a decrease is indicated, and though it's not statistically significant, such behavior could be supported by the organic surfactant model of Rissman et al [2004]). But increased AOD represents greater particle concentration accompanied by greater chances of aggregation [O'Neill et al, 2005], and as noted previously this will increase the CCN activity of smoke.

For this study smoke aggregation is modeled by assuming a logistic curve for the dependence of CCN on AOD. For low AOD the CCN activity is zero, but rises semi-exponentially before saturating at the constant value assumed for smoke in the previous

model. Except for the tendency of smoke CCN activity to approach its limiting value, all other parameters are kept the same as before to produce the following table:

	Canada	Siberia
Low AOD	**0.03**	**0.008**
Middle AOD	**0.09**	**0.030**
High AOD	**0.18**	**0.060**

Table 4.2: Aggregation/Aging + 2-Component Model for AIE.

For low AOD the AIE is now close to zero. When the smoke CCN/AOD ratio was set to the previously measured value of 0.13 (relative to sulfate), the AIE is about 2/3 that seen in Fig. 4.10. But this represents well aged-smoke, and on average this ratio may increase for smaller, fresher particles. It is also likely that the optical properties measured in the mid Atlantic are not representative of aerosol in less developed northern regions. An adjustment that makes the CCN/AOD ratio of smoke equal to 0.2 produces AIE that varies with AOD and region almost exactly like Fig. 4.10. This simple model thus explains all qualitative details of the observations.

4.7 Conclusions

A comparison between the effects of forest fire smoke on cloud microstructure in

Canada and Siberia was performed with rigorous control of observation and cloud geometry to minimize variations in satellite retrieval bias. For this study the Aerosol Indirect Effect (AIE) was defined to be the ratio of the fractional change in cloud drop effective radius (r_e) to the fractional change in Aerosol Optical Depth (AOD). For constant cloud Liquid Water (LW), AIE calculated with r_e is proportional to AIE calculated with cloud condensation nuclei (CCN). The AIE in Canada was observed to be much larger than in Siberia, and in both regions AIE increased with AOD.

According to satellite observations the LW decreases slightly with AOD, a trend that has been observed by aircraft [Brengeuir, 2003]. When clouds at the same stage of development are normalized for LW, the drop number concentration (N/LW) always increases with AOD, though not uniformly. In Canada N/LW changes very little for low AOD before increasing dramatically for high AOD. In Siberia N/LW increases very slightly with AOD, maintaining a value close to that seen for high AOD in Canada.

In the absence of comprehensive in situ aerosol/CCN data, a conceptual two-component cloud nucleation model is proposed to explain regional differences in the response of cloud droplet concentration to aerosol loading. Sulfates capable of producing high CCN per unit AOD are assumed to form a uniform background aerosol, with large variations of AOD attributed to smoke with low CCN per unit AOD. With Europe upwind of the prevailing wind direction, Siberia has a much higher level of CCN in the background, so smoke makes little difference to the total number of CCN. The AIE in Siberia is thus low and changes little with AOD. In Canada sulfates make up a small proportion of the background aerosol, so even though smoke has a low CCN/AOD ratio it

will have a large effect on the percentage of CCN in the region. AIE thus is large in Canada and changes dramatically with AOD. Details of the relationship between AIE and AOD can be modeled by the particle growth of smoke with AOD, increasing the CCN activity.

Chapter 5: Summary

A satellite study of the radiative and cumulus cloud microphyscial effects of smoke may be broken into three component parts: an intensive study of the properties of smoke, an analysis of the biases inherent in satellite retrievals involving cumulus clouds, and a carefully controlled study of the effects of smoke on cumulus clouds. The preceding chapters represent each step in this program.

Chapter 1 presented a study of a smoke plume produced by Quebec forest fires in early July of 2002 that blanketed the eastern seaboard [Taubman et al, 2003]. On July 8th a research aircraft performed 5 spirals from ground level to 3 km MSL; 3 in western Maryland and Virginia in the morning, 2 in eastern Maryland in the afternoon. All but one spiral indicated the same pattern: boundary layer sulfate aerosol up to 2 km, and a comparatively heavy smoke layer from 2 to 3 km.

The primary instruments of interest on the aircraft were a nephalometer that measured scattering coefficients at 450, 550, and 700 nm; and a particle soot absorption photometer (PSAP) that measured the absorption coefficient at 565 nm. These instruments measured an average single scattering albedo of 0.95 in the boundary layer, and 0.93 in the smoke layer. This should be contrasted to the column averaged single scattering albedo of 0.96 retrieved by the GSFC AERONET site. AERONET also retrieved a column-averaged index of refraction of 1.56. By assuming the climatological value of n=1.43 for the boundary layer aerosol and a smoke/BL optical depth ratio of 5/1, a value of n=1.58 was inferred for smoke. When combined with the scattering Ångstrom exponents, a single

mode size distribution could be deduced for each layer. By this method the smoke particle effective radius was calculated to be 0.22 μm; 0.08 μm for the boundary layer aerosol, which also had a much broader distribution than that of smoke.

Given the size distribution and the real index of refraction, the imaginary index of refraction was adjusted so that Mie calculations matched the average value of single scattering albedo measured in situ at 550 nm, and adjusted with wavelength to be proportional to that of black carbon. The real index of refraction was extrapolated from AERONET retrievals assuming the value was dominated by smoke. The resulting physical model could be used to calculated optical properties at any wavelength.

The wideband properties were used to calculate absorptive heating in the smoke layer, demonstrating that the temperature increase from the heating integrated throughout the day was comparable to the subsidence temperature inversion. Absorptive heating could have maintained or strengthened this inversion, reducing convective mixing that would otherwise have dispersed the plume.

When combined with MODIS surface reflectance, this optical model was used to generate satellite retrievals of smoke optical depth throughout the region. Several optical models were tested and the retrieved optical depth compared to AERONET measurements. The optical model based on AERONET total column retrievals compared favorably with the measurements, while those based on in situ measurements were as much as 60% higher. This was attributed mainly to the lower value of single scattering albedo measured in situ.

Broadband forcing calculations at the surface and TOA were compared to broadband

surface radiometers and CERES retrievals, respectively. The optical model based on AERONET retrievals produced higher than measured radiance at TOA but a smaller decrease in radiance at the surface, compared to the in situ model that had similar trends but was much closer to the measurement. The difference is attributed to the smaller particle size in the aeronet model. The differing comparisons to measurements depending on single or broadband calculations indicate the difficulty in aerosol characterization. It is possible that these disagreements between model and observation could be due to the use of a single mode distribution to represent the bimodal distribution rerieved by AERONET for smoke dominated aerosol.

The effects of the three dimensional nature of cumulus clouds on satellite retrievals was explored in Chapter 2 [Vant-Hull et al, 2006]. The relative positions of sun and satellite result in viewing of portions of cloud with varying amounts of shadow. For thick clouds, increasing shadow results in a decrease in retrieved optical depth, and an increase in retrieved droplet effective radius.

To explore this effect, cloud, aerosol, and water vapor data retrieved by MODIS over Amazonia is chosen to allow comparison to several previous studies in the region. Aerosol is constrained to optical depths between 0.2 and 0.4, precipitable water to between 3.5 and 4.5 cm, and solar zenith angle to 20 to 30 degrees. The remaining data is divided into subsets for scattering angles within 45 degrees of backscatter (illuminated) and more than 45 degrees from backscatter (shadowed). The data is further subdivided by cloud top temperature so that cloud vertical development may be plotted on the vertical axis.

The results show a roughly 7 μm separation between the effective radius of shadowed and illuminated clouds (according to the rather arbitrary definition above). This difference may be taken as a measure of the 3D bias, which is seen to decrease as the clouds become shallower. Removal of edge pixels reduces the 3D bias to 5 microns. The fact that the 3D bias is not eliminated for inner pixels indicates that it is largely a sub pixel effect. Not only does the pattern narrow when edge pixels are removed, but it shifts towards smaller effective radius. This indicates that a bias independent of scattering angle, such as surface contamination, is being reduced as well.

Though pure sub-pixel surface contamination can increase the retrieved effective radius, theoretical calculations and arguments show that a mixture of aerosol and cloud exhibits a larger effect. Such mixing would cause a field of small clouds mixed in moderate to heavy aerosol to be retrieved as horizontally large clouds with large effective radius. Due to differing phase functions between aerosol and cloud, the retrieved effective radius would increase in the shadowed geometry. Similar effects are indeed observed in the data.

Illumination from the sides of clouds can increase the apparent aerosol reflectance, thus increasing the retrieved optical depth. In this case the aerosol would be seen to increase systematically with thicker clouds, an effect observed in the data.

Given the number and nature of biases documented in Chapter 3, an attempt to eliminate them for cumulus clouds is untenable. The alternative is to compare regions with very similar experiment geometry but varying aerosol composition. This was done in chapter 4, with the selection of forested regions in Canada and Siberia at the same

latitude.

Both regions are subject to smoke aerosol from primarily coniferous forests. But with prevailing westerly winds, western Siberia is downwind from Europe, while Canada is downwind of the northern Pacific and eastern Siberia. An aerosol transport model (GOCART) predicts much higher sulfate content in Siberia aerosol. Other differences are the generally higher altitude of the Canadian region, linked to lower average precipitable water.

A number of constraints were placed on the data sets. To remove extreme meteorological events, the high and low ends of the surface pressure and temperature distributions were trimmed. To reduce 3D biases, the cloud fraction was limited to less than 60% and the cloud optical thickness to greater than 8. Cloud top temperature was limited to higher than 270 K. The most important meteorological constraint was the limitation of total precipitable water in both regions to between 1.4 to 2.4 cm to ensure that the clouds had enough water supply to become fully developed. Cloud systems with lower PW were seen to have effective radii that decreased with altitude. A comparison of cloud optical thickness and fraction in the two regions indicated very similar cloud geometry. The sun-satellite geometry was limited by restricting the solar zenith angle to between 33 and 48 degrees, the satellite zenith angle to les than 50 degrees, and the scattering angle from 25 to 55 degrees.

Since the cloud base altitudes could be highly variable, the satellite imagery was divided into 50 km squares, and the warmest cloud top with an optical thickness between 8 and 13 was used as a proxy cloud base with other cloud top temperatures in the box

subtracted from it. Data were then binned by aerosol loading and temperature difference above the cloud base. Average values of effective radius and cloud optical thickness were calculated within each bin.

The results showed a general decrease in cloud liquid water and effective radius with aerosol loading for both regions. The percentage change in effective radius with AOD increased with AOD. Both the average effective radius and the rate of change of effective radius with AOD were larger in Canada. A simple model to explain these regional differences relied on the assumption of a background sulfate aerosol that was higher in Siberia than in Canada. Variability in AOD was attributed to smoke, which due to it's greater scattering coefficient per particle exhibited a smaller number of cloud condensation nuclei (CCN) per unit AOD than sulfate. With a lower background sulfate aerosol in Canada, the addition of smoke had a larger effect on the CCN population than in Siberia. The smaller average drop size in Siberia could be due either to the extra sulfate, or to the larger smoke particles (as measured by AERONET) with greater CCN activity.

Appendix A: Concepts of Radiation Transfer

Radiation transfer calculations typically divide into the solar spectrum and the terrestrial thermal spectrum. Except in the case of combustion temperatures the two regimes overlap in the mid IR. This region will be avoided, though in some cases there are arguments for using this wavelength band [Rosenfeld et al, 2004]. Thermal emission can be described by the well-known Planck Blackbody equation if the emitting objects have enough optical density to capture and equilibrate the thermal radiation that impinges upon it. For all analysis that follows objects suspected of being thermal gray bodies are rejected. Thermal IR wavelengths are so much larger than atmospheric constituents that scattering can be ignored (see below), so only absorption need be accounted for. A 'window channel' represents a judicious choice of observation wavelength for which absorption (even by water vapor) is small enough to be ignored. Throughout this work the 10.8 μm window channel will be employed. The steps listed above simplify thermal radiation transfer calculations to such an extent that further discussion is unnecessary.

Optical instruments measure radiant intensity. But for objects reflecting the sun's rays, this radiance will change with sun angle, even if the intrinsic reflectivity of the object does not. In order for the radiance from an object to represent its true physical properties, it is common practice to convert radiance to reflectance, defined as the reflected flux divided by the incoming solar flux. Since an instrument typically can only observe light from one direction at a time, it is necessary to assume the reflected light is scattered uniformly in all directions (Lambertian) in order to estimate the reflected flux.

This simplifying assumption can result in calculated reflectances greater than unity.

Radiation transfer in the solar spectrum divides into two steps: calculation of the optical properties of the medium based on composition and size distribution, and use of these optical properties to calculate the fate of solar radiation incident on the atmosphere. These steps will be discussed in reverse order.

A.1 The Radiation Transfer Equation

The basic metric of radiation transfer calculations is the optical depth, τ, defined as the optical cross sectional area per unit area of a given medium such as an atmospheric column, a cloud, or an aerosol layer. In terms of particles that make up the medium, the optical depth may be visualized as the number of times on average a line drawn through the medium would intercept a particle. As discussed below, it is necessary to use the optical cross section of each particle, which due to wave effects is not equal to its geometrical cross section. There being no other forms of interaction available to light, the optical depth must equal the sum of the absorption and scattering cross sections (transmission is considered scattering). The differential element of optical depth is thus

$$d\tau = (\sigma_S(z) + \sigma_a(z))dz \qquad \text{(A.1)}$$

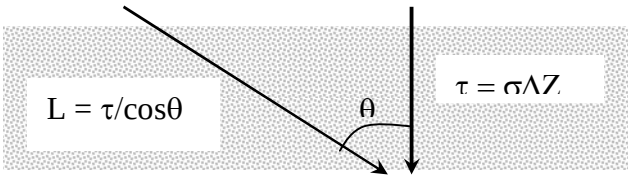

Figure A.1: The optical depth is measured from the vertical, the optical path length L may be calculated from it and the zenith angle.

for which $d\tau$ represents the probable number of interactions per unit area per photon (extinction cross section) and σ_x represent the number of scattering or absorption events per unit volume per photon.

A beam of light of intensity I moving in the direction of the solid angle Ω will be diminished by the scattering and absorption, while light scattered in the same direction (forward scattered from a current event or multiply scattered from a previous event) will augment it. This is described by the radiation transfer equation:

$$dI = -I(\sigma_S + \sigma_a)dz + \sigma_S\{\int P(\Omega - \Omega')I(\Omega')d\Omega'\}dz$$
$$\text{or} \quad \cos(\theta)\frac{dI}{d\tau} = -I + \omega_o \int P(\Omega - \Omega')I(\Omega')d\Omega \qquad \text{(A.2)}$$

Where all variables are assumed to be functions of z, and unless otherwise noted the intensity I is in the original Ω direction. We introduce the scattering phase function $P(\Omega-\Omega')$, which provides the fraction of light from angle Ω' scattered into the angle Ω. The second equation is the result of several steps. Dividing through by the optical depth as defined in equation 1.1 leads to the definition of the single scattering albedo:

$$\omega_o = \frac{\sigma_s}{(\sigma_s + \sigma_a)} \qquad \text{(A.3)}$$

which represents the probability that a photon/particle interaction will be a scattering event. Finally, the common definition of optical depth as measured in the vertical requires accommodating the longer path length of off-vertical directions. This is

accomplished by the factor of 1/cosθ as shown in Figure A.1.

The need to integrate over all scattering angles in the phase function makes the radiation transfer equation (A.2) impossible to solve analytically in all but a few simplified cases. The phase function term will drop out in two cases: if the wavelength is so much larger than the particle radius that scattering can be ignored, or if the direct beam is being observed and the medium is tenuous enough that multiple scattering is not expected to contribute to the original direction. In such cases the exponential solution known as Beer's law results.

In general equation A.2 must be solved numerically. A common approach is to break the radiation into discrete streams in a number of directions, and approximate the phase function in a piecewise manner corresponding to each stream. This 'discrete ordinate' or 'DISORT' method [Stamnes et al, 1988] is used here. Such numerical codes provide input for atmospheric parameters, aerosols, and cloud droplets.

A two-stream model is too simple for use in atmospheric measurement, but yields enough physical insight that aspects of the solution are used as a brief summary of experimental situations. An example is the asymmetry parameter g, which is the vector component of the scattering phase function in the forward direction:

$$g = \int P(\theta)\cos\theta d\theta \qquad \text{(A.4)}$$

The phase function is assumed to be axially symmetric so that the meridional angle may be ignored. Since the phase function is normalized, the asymmetry parameter is

equal to (forward scattered components – backward scattered components). A particle that scatters primarily in the forward direction would have an asymmetry parameter near unity; one that scattered equally in all directions would have g = 0.

A.2 Calculating Particle Optical Properties

The size distribution of the set of particles in question is a key ingredient for any radiation transfer calculations performed. A Gaussian distribution cannot be used because it allows negative particle radii. A common solution is to use the transformed variable x = ln(r), where r is the particle radius, in the Gaussian formula [Wilks, 1995]:

$$n(r) = \frac{1}{r\sigma\sqrt{2\pi}} \exp\left(-\frac{(\ln r - \mu)^2}{2\sigma^2} \right) \qquad \text{(A.5)}$$

Where μ and σ are the average and standard deviation of ln(r), respectively. This is known as the 'lognormal distribution'. The r in the denominator appears because n(r) by itself is not mathematically meaningful; only n(r)dr, and the derivative of ln(r) is dr/r.

With the size distribution in hand, several weighted averages of r, or moments, may be calculated. The nth moment is defined as:

$$< r >_n \;=\; \frac{\int r \bullet r^n n(r) dr}{\int r^n n(r) dr} \qquad \text{(A.6)}$$

For radiation transfer calculations the most useful quantity is the area weighted average, or second moment, referred to as the effective radius. Atmospheric chemists tend to prefer the volume-weighted radius. One of the reasons equation A.5 is so popular is that if used it is easy to convert between different moments. When the integrations of equation 1.6 are transformed to the logarithmic variable x, the moments are shown to be proportional to $\exp\left[\frac{1}{2}(2n-1)\sigma^2\right]$. There is thus no need to recalculate.

Given the complex index of refraction and the size distribution, all optical properties of a set of particles may in principle be calculated. The particle shape will affect these properties, though spheres are commonly assumed in the absence of detailed shape information. In 1908 Gustav Mie solved the problem of plane waves scattered by spheres by matching boundary conditions with an infinite set of spherical orthogonal functions, the Legendre polynomials [Van der Hulst, 1957]. The first Legendre polynomial is the asymmetry parameter introduced in the last section. From this solution the scattering phase function and the single scattering albedo is derived, and the radiation transfer equation A.2 may be applied.

Though Mie theory is sufficient to derive all the optical properties, a qualitative understanding is useful for discussion. Intuitively we expect the scattering cross section of a particle to be proportional to the geometrical cross sectional area. The proportionality constant in fact varies with the radius/wavelength ratio, in a way shown schematically in Figure A.2a. We will use micron scale solar radiation as a reference

wavelength for all the discussion that follows. When the particle is much smaller than the

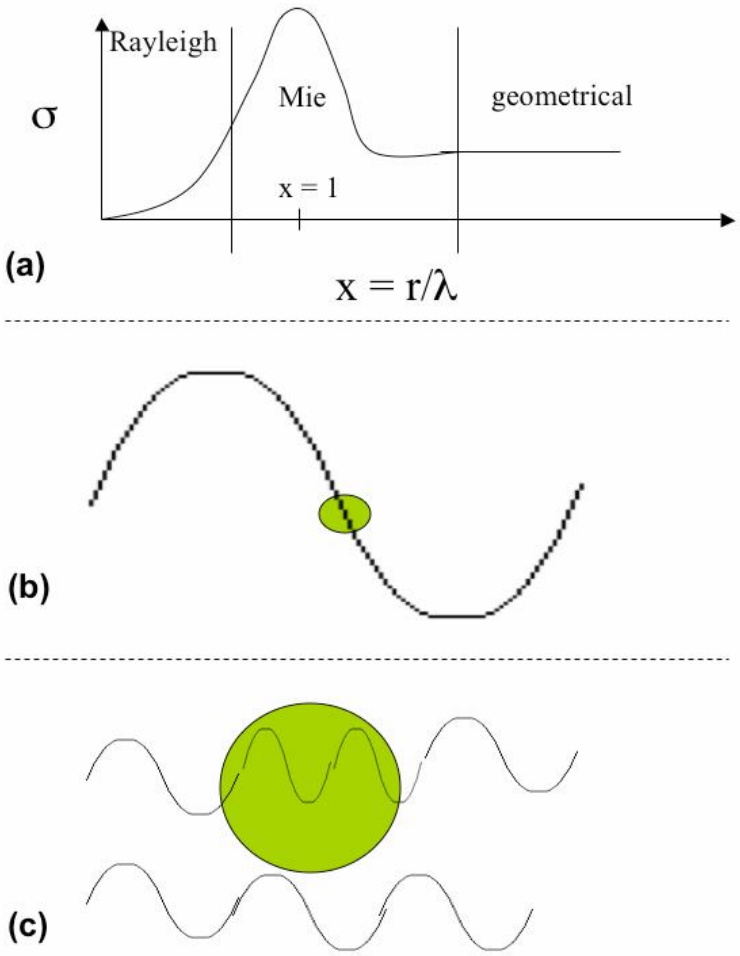

Figure A.2: Variation of scattering cross section σ with incident wavelength. (a) A plot of the full range of variation. (b) The Rayleigh scattering situation. (c) The Mie scattering situation.

wavelength the proportionality rises quickly with size. This is known as the Rayleigh scattering regime, typified by air molecules. When the particle size and wavelength are comparable we are in the rapidly changing Mie regime, common for aerosols. Finally we enter the constant geometrical scattering regime used for cloud drops. Each regime will be explored in turn.

When a small particle encounters a much larger electric wave, the electric field is

nearly constant across the extent of the particle, as shown in Figure A.2b. The particle will become polarized, producing an electric field proportional to the amount of charge in the particle. The amount of charge is proportional to the volume, or r^3. The intensity of the wave is proportional to the electric field squared, or r^6. Dividing by the geometric area leads to a Rayleigh scattering cross section coefficient of r^4. Since dipole radiation increases with the 4rth power of frequency (inversely proportional to wavelength), the Rayleigh scattering coefficient increases as $(r/\lambda)^4$. Small particles therefore have a scattering cross section that increases rapidly with size/wavelength ratio.

As the particle size approaches the wavelength, interference between the wave transmitted by the particle and the wave immediately beside it becomes an issue (Figure A.2c). The index of refraction n decreases the wavelength inside the particle, so for the transmitted wave to line up with and constructively interfere with the external wave, the first interference peak occurs when $\lambda n = r$. Though not shown in figure A.2a, other peaks occur for higher integer ratios, generally weaker for higher ratios.

Finally, as the particle becomes large with respect to the wavelength, spatial separation between the transmitted wave and the external wave becomes much larger than the wavelength itself, and interference effects diminish. The proportionality factor between the optical and geometrical cross section becomes constant. By Babinet's principle the light scattered by transmission is equal to that scattered around the edges by refraction, so the proportionality factor becomes 2.

The scattering Ångstrom exponent is commonly used as an indication of particle size:

$$\alpha = - \frac{\log(\sigma_{s\lambda 1}/\sigma_{s\lambda 2})}{\log(\lambda_1/\lambda_2)} \qquad \text{(A.7)}$$

At the geometrical limit where scattering is independent of wavelength, α equals zero. For extremely small particles α approaches the Rayleigh limit of 4.

The last issue to be discussed qualitatively is the preferred scattering direction. The top of Figure A.3 shows the response of charges in a small particle to a driving electric wave: they respond with a field of their own that propagates equally in all directions, with a fixed phase relation to the driving wave (typically not exactly in phase as shown here). As the particle becomes larger the secondary waves produced will be in phase with each other in the forward direction, but progressively out of phase in the back scatter direction, and so tend to suffer destructive interference (bottom). The result is that larger particles preferentially scatter in the forward direction; smaller particles approach isotropic scatter patterns (phase functions).

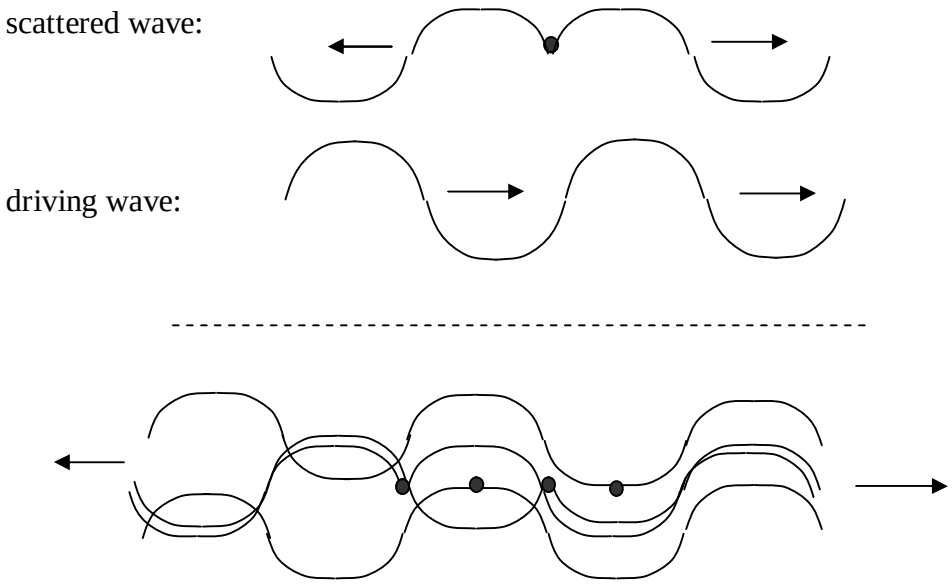

Figure A.3: Backward versus forward scattering. Top: a single dipole response to a driving wave. Bottom: the response of an array of dipoles in an extended object.

Appendix B: Cloud Physics

A major part of the climatic effect of smoke stems from its effects on clouds. Twomey [1977] first pointed out that since aerosols form the cloud condensation nuclei (CCN) needed for cloud drop formation, the aerosol concentration in large part determines the cloud drop concentration. Given fixed cloud liquid water the drop size would decrease as the aerosol concentration increased. As mentioned above, the presence of aerosol could alter the environmental variables and change the fraction of available water vapor converted to cloud liquid water, so that it is conceivable for an increase in aerosol to result in an increase in droplet size [Yuan et al, 2007; Feingold et al, 2002]. Generally absorbing aerosol tends to stabilize the column and decrease the liquid water of clouds in formation [Taubman et al, 2004; Ramanathan, 2001B], so that droplets will almost universally decrease in size with an increase with aerosol loading. Smaller drop sizes inhibit precipitation and could lead to longer cloud lifetimes. In this case the shading effect of aerosols would be augmented through their influence on cloud lifetime.

Background knowledge of cloud processes is essential to understand how aerosols may affect clouds. The next section provides a brief introduction to cloud dynamics and thermodynamics on the cloud scale. This is followed by the physics of droplet formation, generally referred to as 'microphysics'. The majority of this information can be found in standard textbooks, (such as by Rogers and Yau [1996]) so will not be attributed. Equations are also avoided since they are not used for the work that follows.

B.1 Cloud Dynamics and Thermodynamics

A cumulus cloud is a heat engine driven by buoyancy and latent heat. The process begins when heated air near the surface is either warmer than the surroundings or is perturbed into cooler air above. Temperature (and to a lesser extent humidity) differences result in density differences between the air and surroundings, producing a proportional buoyant acceleration. As the air rises into lower pressure it expands and cools by doing work against the environment. The rate at which a parcel of air cools this way, or 'adiabatic lapse rate', is a constant ~10° C/km, which may be increased somewhat by mixing with environmental air. Within a few km of the surface the environmental lapse rate will vary (and be interrupted by inversions), but on average exhibits a decrease of approximately 6° C/km. The situation is as shown in Figure B.1,

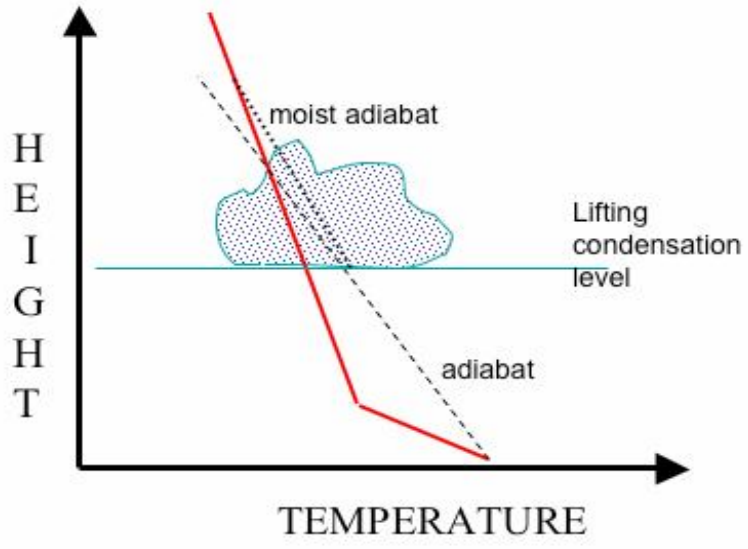

Figure B.1: Atmospheric temperature profiles and cloud formation.

with the dotted line showing the adiabatic lapse rate and the dark line the environmental temperature profile, including an increase in temperature near the surface due to solar heating. For the numbers given above, once the heated air begins to rise it will approach the environmental temperature at a rate of 4° every km. How high it rises depends on the temperature difference imposed by surface heating: if the difference is 8 degrees, it will rise 2 km before the parcel temperature matches that of the environment, assuming no condensation. Such parcels are often referred to as 'thermals', and this maximum level might be called the 'dry thermal height'.

Saturation vapor pressure above a liquid surface is a balance between capture of vapor molecules that impact the surface and evaporation of molecules near the surface that are energetic enough to escape from the Van der Waals forces of the liquid. An increase in temperature results in more molecules escaping, so the vapor density increases until the impaction rate once again balances the evaporation rate. The saturation vapor density is thus a function only of temperature and liquid binding energy, at least for a pure liquid with a flat surface. In meteorology the water vapor density is often rephrased as the mixing ratio, or ratio of the mass of water to mass of dry air. The temperature at which saturation occurs is called the dew point. A parcel of air that rises and cools until it reaches the dew point determined by the mixing ratio will experience condensation that drops the vapor content back to saturation. This altitude is called the lifting condensation level, and marks the location of cloud base. Convective clouds will form so long as the lifting condensation level is below the dry thermal height, a quantity

that will change with local surface heating and so is difficult to predict. As the parcel continues to rise the water vapor will continue to condense out to avoid supersaturation, forming a cloud. This picture will be modified slightly as we discuss vapor pressure above the curved surfaces of water drops in the next section.

With condensation comes latent heat release. The immediate effect is an increase in parcel buoyancy, so that the cloud will develop above the dry thermal height. This is shown in a decreased slope of the 'moist adiabat' of Fig. B.1. The cloud is a pump running on latent heat. The strength of this pump will depend on the environmental lapse rate that fixes the buoyant acceleration and in consequence the rate at which water is condensed.

B.2 Cloud Droplet Formation and Growth

A small drop has evaporation properties very different from the bulk state. As surface curvature approaches the molecular scale molecules become less tightly bound to the drop because on the surface they have fewer neighbors to form hydrogen bonds with (Figure B.2). A small pure water droplet is prone to fly apart under molecular kinetic fluctuations before it can grow, and in the absence of other influences pure water vapor will not condense unless it is highly supersaturated.

Aerosols act as cloud condensation nuclei (CCN) allowing drops to form within a few percent of standard saturation amounts. Water molecules adhere to hydrophilic aerosols, providing a base for drop formation that bypasses the small drop barrier. Water

soluble aerosols also inhibit evaporation by the presence of extra non-water molecules

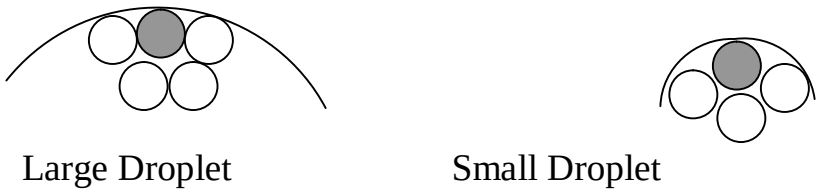

Figure B.2: How drop size can affect molecular hydrogen bonding. The water molecule in question is shown in gray, surrounded by neighbors in white. The molecule in the larger droplet is more tightly bound.

masking the surface area. These same molecules may also enhance evaporation by decreased hydrogen bonding, but which effect is more important depends on the solute.

Once the drop has formed its rate of growth is determined by molecular and thermal diffusion, which in turn depend on the drop radius, environmental saturation and temperature. Clearly the molecular diffusion and the drop growth rate increases with the supersaturation. In order for diffusive transport to operate, there must be a gradient from the drop surface to the ambient conditions at a suitable distance from the drop. These gradients are larger for small drops, which thus grow faster than larger drops, narrowing the size spectrum with time.

The updraft velocity with the associated drop in temperature would create an increasing supersaturation if not for condensation. If droplet condensation does not keep up with the growth of supersaturation, other aerosol which are otherwise too small or insoluble to form drops may activate, increasing the droplet concentration. Cloud dynamics is thereby linked to the droplet spectrum.

The final step in the cloud cycle is either evaporation or precipitation, depending on how large the drops grow before the updraft and/or water vapor runs out. Droplets less than about 14 microns in radius tend to follow the air stream flowing around other solid objects, so do not collide [Rosenfeld and Lensky, 1997; Ramanathan et al, 2001]. These drops are too small for precipitation. Those that do cross this hydrodynamic threshold will grow rapidly by coalescence. The exact rate of growth is determined by variability in the size distribution: large drops 'fall through' smaller drops, collecting them in the process. A sharp size distribution must rely on random collisions, reducing the growth rate.

B.3 Measuring Cloud Properties by Satellite

Satellites provide the best survey of clouds available, but in order to make operational retrieval algorithms mathematically tractable, the clouds are universally assumed to uniformly fill the observed pixel, and be flat with no radiative communication with neighbor pixels [Iwabuchi et al, 2002]. Even though cloudy pixels judged incapable of fulfilling these requirements are flagged or deleted, significant errors still arise and are the topic of chapter 3.

Cloud top brightness temperature can be directly related to the blackbody radiation in a window channel, as discussed above. Since cumulus clouds are not flat it is very possible that a wide variation of actual cloud top temperature may occur within a satellite pixel, making it difficult to assign cloud water phase based on this measurement

alone. Water phase is detected directly by the comparison between a reference wavelength that is not strongly affected by the phase change, and a second wavelength

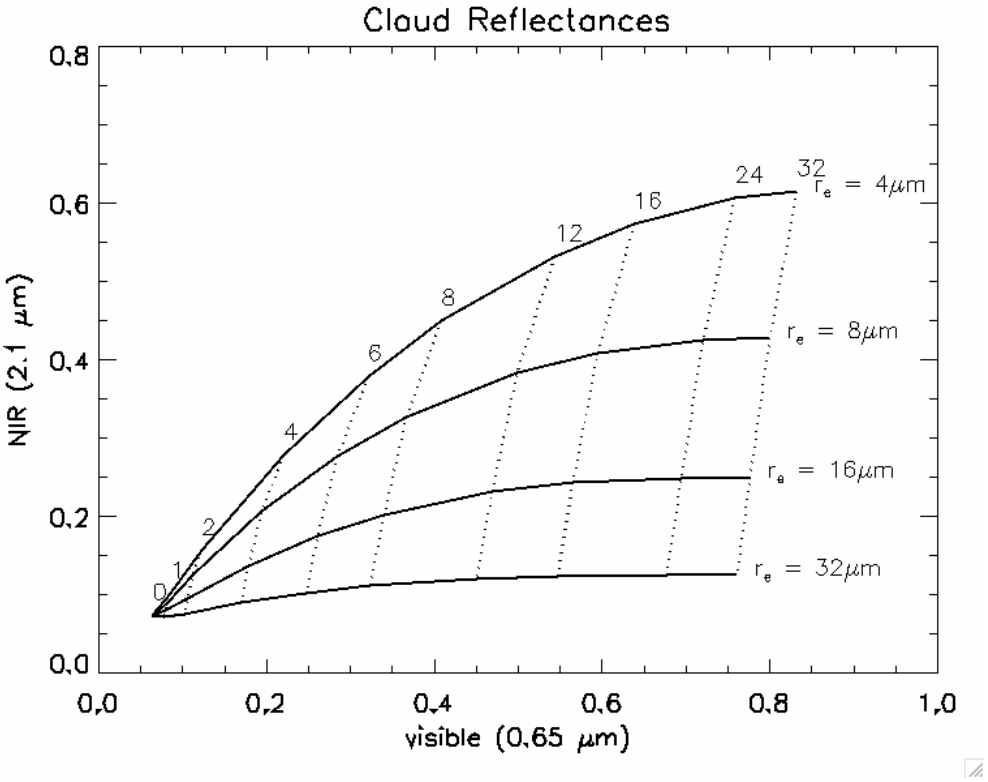

Figure B.3: a lookup table for retrieving cloud optical depth and drop effective radius from reflectances in the visible and NIR. Cloud OD is shown in dotted lines, effective radius in solid lines, for a surface reflectance of 0.1, solar zenith angle of 25 degrees, and the satellite at nadir.

that is [Platnick et al, 2003]. Use of the thermal IR allows an algorithm to be used both day and night, with the 10.8 μm channel used as the reference and 8.5 μm as the phase sensitive channel, for which the emissivity is larger for ice than water. Water vapor absorbs at a wavelength of 8.5 μm, so this test is not useful for low clouds. For daylight phase detection the difference between the 1.6 and 2.1 μm bands is used. In practice multiple tests are often used, and if they contradict one another the phase is flagged as mixed or uncertain.

For this study only water clouds were used, simplifying the retrieval process. Other than cloud top temperature, the only pixel level cloud properties retrievable by satellite are optical depth and effective radius [Nakajima and King,1990]. Two window channel wavelengths are used to estimate these two variables. The simplest approach is to generate lookup tables of these reflectances for theoretical clouds spanning a reasonable range of optical depth and effective radius. Such a lookup table appears in Figure B.3 for reflectances calculated for a point directly above clouds with the sun at a zenith of 25 degrees. Actual observed reflectances for the same geometrical situation would fall somewhere on this chart, and the values of optical depth and effective radius could be interpolated from the surrounding points.

This plot invites physical discussion. The visible channel is not absorbed by water, while the near infrared channel is. For thin clouds both reflectances will be low, (bottom left), with the NIR lower due to absorption, so far constant effective radius the slope of the vis/NIR curve is always less than one. Smaller drops are closer to the Mie scattering peak of figure A.2a, so have a higher scattering to absorption ratio and the NIR reflectance is higher (as is the NIR single scattering albedo). As the cloud becomes thicker multiple scattering results in a graybody NIR reflectance that is independent of the cloud thickness, only on the single scatter albedo determined by the drop radius. Throughout the reflectance range it is seen that for a given optical depth (a quantity defined in the visible) the reflectance increases slightly as effective radius decreases. This is due to greater backscattering from smaller particles.

B.4 Aerosol Effects on Clouds

The strongest effect aerosols have on clouds in through the role of CCN. When water vapor is divided among more condensation nuclei the resulting drop size must decrease [Twomey, 1977]. Though aerosol may be related to or even affect the water supply [Han, 2000; Ackerman, 1995], the bulk of experimental observation bears out the general decrease of drop size with aerosol loading [Rosenfeld and Lensky, 1997; Koren and Kaufman, 2005, Feingold et al, 2002]. The decrease in drop size limits coalescence and precipitation, thus increasing the cloud lifetime [Haywood and Boucher, 2000].

The direct radiative effect of aerosols can affect the atmosphere in ways that influence cloud development. Aerosols shade the surface, decreasing the heated layer that can feed convection. Absorbing aerosol can heat the upper atmosphere, and the combination of the two effects can result in a lower lapse rate and a more stable atmospheric column [Taubman et al, 2004], reducing the thermal height and cloud development. This shading can also reduce transpiration, a major source of water vapor over forested regions [Koren et al, 2004].

Effects other than direct radiative interaction with aerosols are commonly referred to as *indirect effects,* and refer exclusively to aerosol interactions with clouds. The tendency of aerosol to change drop size through the role of CCN is termed the 'first indirect effect'; the tendency to change cloud lifetime via precipitation/CCN processes is termed the 'second indirect effect'; and the effect of modified temperature profiles on clouds is termed the 'semi-direct effect'. Though these terms are in common usage, they possess no descriptive power and will be avoided in this work.

Appendix C: Aerosol Measurement Instrumentation

Remote sensing and in-situ measurements have complementary strengths and weaknesses. Passive remote sensing techniques retrieve column-averaged properties. Surface photometers such as those used by AERONET (described below) offer the advantage of viewing the aerosol sample over a range of scattering angles, allowing the characterization of a complete suite of column-averaged aerosol optical properties [Dubovik et al, 2000]. While remote sensing techniques do not perturb the measured aerosols, validity of the theoretical framework and assumptions dictates the quality of retrievals [Remer et al, 1997; Dubovik et al, 2000]. Satellite retrieval techniques must contend with a varying surface albedo and a fixed viewing angle for any given location, both of which limit retrieval of a full set of optical properties. Usually one or several of the aerosol optical properties are fixed based on independent measurements (or assumption), and the remainder are derived from satellite measured reflectances [Kaufman et al, 1990a; Wang et al, 2003]. In situ observation techniques can resolve vertical profiles inaccessible to remote sensing. If properly calibrated [Bond et al, 1999], they may be used to validate assumptions made in satellite retrievals. On the other hand, they may introduce additional errors from instrumental interaction with the measured aerosols [Remer et al, 1997; Bond et al 1999]. Both in-situ and sun photometer measurements of aerosol optical properties have been incorporated into satellite retrieval algorithms [Bundke et al, 2002; Kaufman et al, 1998].

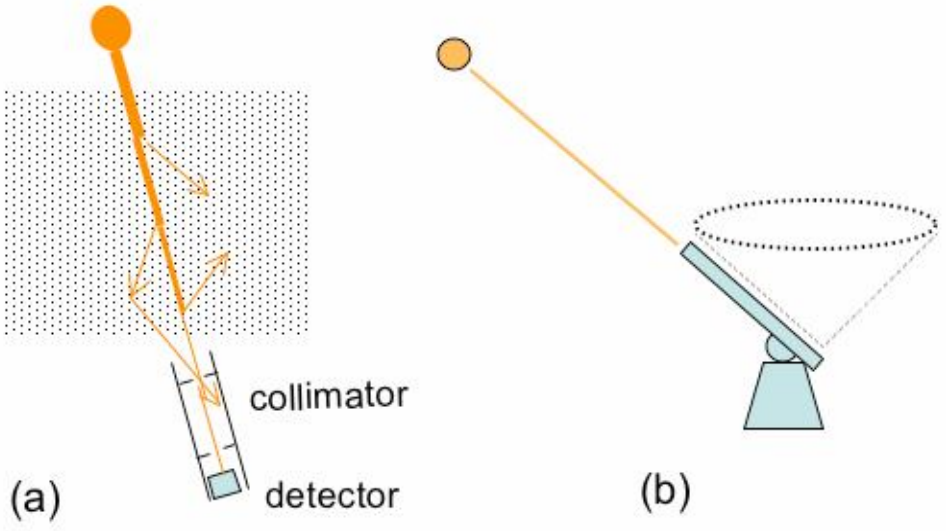

Figure C.1: AERONET operation. a) Direct sun mode. b) Almucantur mode.

C.1 AERONET

AERONET [Holben et al, 1998] is an automated network of ground-based sun photometers that measure aerosol optical thickness and sky radiance at six wavelengths (0.34, 0.38, 0.44, 0.67, 0.87 and 1.02 microns). From the sky radiance measurements aerosol size distributions and optical properties are derived operationally. Optical depth is calculated from attenuation of the solar direct beam, with uncertainties set by instrumental precision. Uncertainty in all other optical properties depends on the reliability of the plane parallel assumption for a large set of measurements at different angles as well as the numerical algorithmic precision.

The key to the accuracy of AERONET's optical depth measurement is precise collimation: secondary scattering events are unlikely to augment the direct beam, as

shown in Figure C.1a. Atmospheric correction - taking into account locally measured pressure and total column water vapor - completes the measurement. Clouds are screened under the assumption that their reflectance variability will be much greater than that of aerosol. Each measurement is actually a triplet of observations taken 30 seconds apart. If the variation is too high the observation is rejected as cloud contaminated.

All other aerosol optical properties are derived from an almacantur scan (Figure C.1b). Assuming a cloud free sky, a series of radiance observations at a set of azimuth angles allows retrievals of size distribution (in 22 bins) and complex index of refraction restricted only by smoothness constraints [Dubovik and King, 2000]. These values are sufficient to calculate the optical properties from Mie theory.

C.2 MODIS Aerosol Retrievals over Land

The MODIS instruments are scanning spectral radiometers mounted on the polar orbiting Terra and Aqua satellites that are sun synchronous with equator overpasses of 10:30 AM and 1:30 PM respectively. The instrument has 36 channels with nadir resolutions of 250 m for the traditional NDVI red/NIR channels, 500 m for the remaining visible and NIR channels, and 1 km for the thermal IR channels. Solar radiances are calibrated to the moon, thermal radiances to an internal blackbody.

When this work was begun (chapter 2 &3) the collection 4 retrievals were available [Remer et al, 2005], but were replaced by the collection 5 retrieval [Levy et al, 2007] by the time work on the final chapter was initiated. In the collection 4 algorithm the surface reflectance in the red and blue (green is rejected as too sensitive to vegetation) is

estimated as constant ratios to the 2.1 μm reflectance, to which all but dust aerosol is transparent. Aerosol models are assumed based on location and season. The atmosphere corrected reflectances in the two visible channels are interpolated to provide the optical depth at 0.55 μm. Collection 5 improves the estimation of surface reflectance to vary with angle and vegetation (NDVI), updates the aerosol models, and introduces a 3-channel inversion to improve estimation of the coarse mode fraction.

Both algorithms use a cloud mask based on spatial variability of the visible reflectance [Martins et al, 2003] under the assumption that aerosol is much smoother than cloud. Further precautions are taken by removing the brightest 50% of cleared pixels and the darkest 20% to remove cloud shadows (Figure C.2).

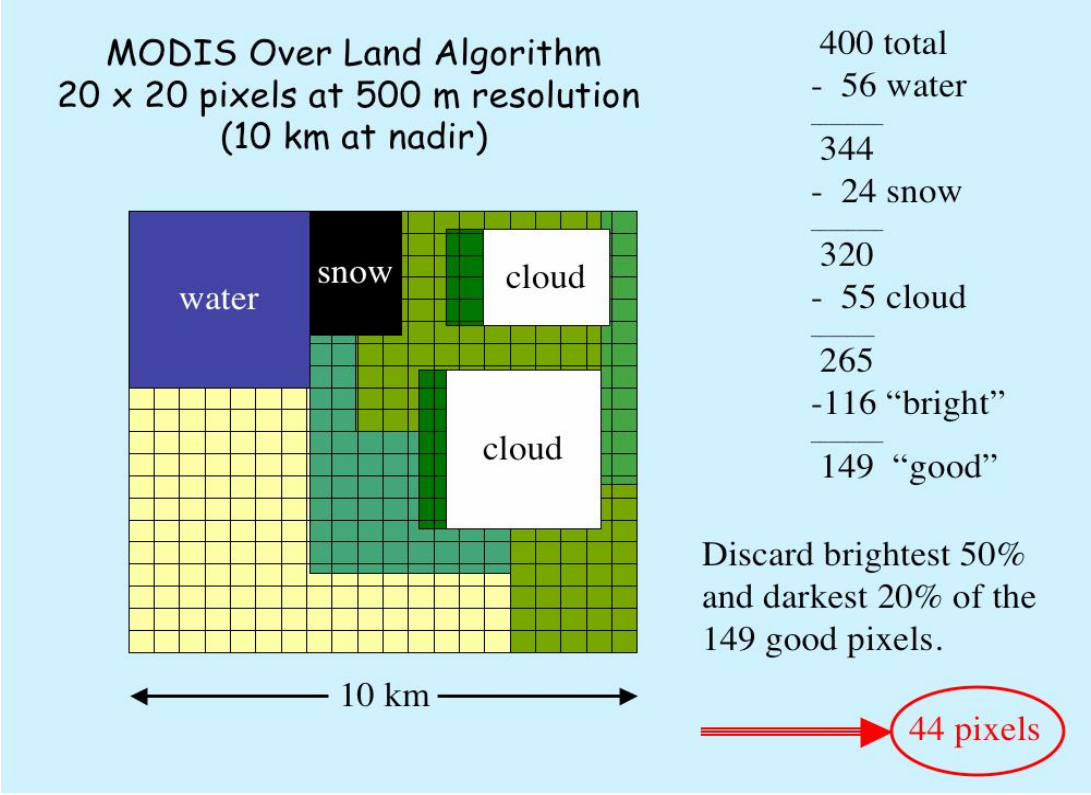

Figure C.2: Final step in the MODIS aerosol cloud screening algorithm. Courtesy of Lorraine Remer and Richard Kleidman.

C.3 In Situ Measurements

The scattering cross section per volume of air can be measured by an integrating nephelometer [Anderson and Ogren, 1998]. Light of carefully monitored intensity at specific wavelengths is projected into a spherical sample chamber. The sides of the chamber are blackened, with a detector attached to a light trap running longitudinally relative to the incoming beam. Since the scatter pattern should be axially symmetric this arrangement is sufficient to infer the total amount of scattered light. The major error is due to detector absence at the light inlet and outlet. The amount of loss depends on the phase function, to which the Ångstrom exponents are related. A empirical correction by Anderson and Ogren [1998] uses the Ångstrom exponents to reduce this error.

The absorption cross section per volume of air can be measured by a Particle Soot Absorption Photometer (PSAP) based on differential filter transmittance [Anderson et al, 1999]. A calibrated volume of air is based through a non-absorbing filter designed to capture the aerosol. Light is passed through it and extinction measured by a wide area detector that catches the forward transmitted light. A clean filter setup is run in tandem for comparison. If all the scattered light were detected the measured extinction would be due to aerosol absorption. Though the filter is designed to reduce backscattering by a close match in index of refraction between it and the aerosol, a correction based on the scattering measured by nephelometers run in parallel may be applied [Bond et al, 1999]. Given that scattering is typically one to two orders of magnitude larger than absorption, the correction is a significant part of the measurement.

References

Ackerman, A., O. B. Toon, P. V. Hobbs, "Numerical modeling of ship tracks produced by injection of cloud condensation nuclei into marine stratiform clouds", *J. Geophys. Res. 100 (D4),* 7121-7133, 1995.

Ackerman, A., O. B. Toon, D. E. Stevens, A. J. Heymsfield, V. Ramanathan, E. J. Welton, "Reduction of Tropical Cloudiness by Soot", *Science,* 288, 1042-1047, 2000.

Albrecht, B., "Aerosols, Cloud Microphysics, and Fractional Cloudiness", *Science,* 245(4923), 1227-1230, 1989.

Anderson, T.L., D.S. Covert, S.F. Marshall, M.L. Laucks, R.J. Charlson, A.P. Waggoner, J.A. Ogren, R. Caldow, R.L. Holm, F.R. Quant, G.J. Sem, A. Wiedensohler, N.A. Ahlquist, and T.S. Bates, "Performance characteristics of a high-sensitivity, three-wavelength, total scatter/backscatter nephelometer", *J. Atmos. Oceanic Technol., 13,* 967-986, 1996.

Anderson, T.L., and J.A. Ogren, "Determining aerosol radiative properties using the TSI 3563 Integrating Nephelometer", *Aerosol Sci. Technol.*, 29, 57-69, 1998.

Anderson, T.L., D.S. Covert, J.D. Wheeler, J.M. Harris, K.D. Perry, B.E. Trost, and D.J. Jaffe, "Aerosol backscatter fraction and single scattering albedo: measured values and uncertainties at a coastal station in the Pacific NW", *J. Geophys. Res.*, 104, 26793-26807, 1999.

Anderson, T.L., S.J. Masonis, D.S. Covert, N.C. Ahlquist, S.G. Howell, A.D. Clarke, and C.S. McNaughton, "Variability of aerosol optical properties derived from in situ aircraft measurements during ACE-Asia", *J. Geophys. Res.*, MS#2002JD003247, accepted 11 Feb 2003.

Andreae, M.O., D. Rosenfeld, P. Artaxo, A. Costa, G. Frank, K. Longo, M. Silva-Dias, "Smoking Rain Clouds Over the Amazon". *Science,* **303,** 1337-1342, 2004.

Andreae, M.O., and P. Merlet, "Emission of trace gases and aerosols from biomass burning", *Global Biogeochem. Cycles, 15,* 955-966, 2001.

Bergstrom, R., P. Russell, P. Hignett, "Wavelength Dependence of the Absorption of Black Carbon Particles: Predictions and Results from the TARFOX Experiment and Implications for the Aerosol Single Scattering Albedo", *J. Atmos. Sci. 59,* 567-577, 2002.

Bodhaine, B.A., "Aerosol absorption measurements at Barrow, Mauna Loa, and the South Pole", *J. Geophys. Res., 100,* 8967-8975, 1995.

Bohren, C. and D. Huffman, *Absorption and Scattering of Light by Small Particles.* John Wiley and Sons, New York, 1983.

Bohren, Craig, "Multiple Scattering of Light and Some of its Observable Consequences". *Am. J. Phys*., 55**,** 524-533, 1987.

Bond, T.C., T.L. "Anderson, and D. Campbell, Calibration and intercomparison of filter-based measurements of visible light absorption by aerosols", *Aerosol Sci. Technol.*, *30*, 582-600, 1999.

Brenguier, Jean-Louis; Pawlowska, Hanna; Schüller, Lothar: "Cloud microphysical and radiative properties for parameterization and satellite monitoring of the indirect effect of aerosol on climate",*J. Geophys. Res.*Vol. 108, No. D15, 8632, doi 10.1029/2002JD002682, 2003

Brennan, J., Y. Kaufman, I. Koren and R.R. Li, "Aerosol-Cloud Interaction – Misclassification of MODIS Clouds in Heavy Aerosol." *IEEE Trans. Geo. Rem. Sens.* vol. 43, pp. 911-915, 2005.

Bundke, U., G. Hanel, H. Horvath, W. Kaller, S. Seidl, H. Wex, A. Wiedensohler, M. Wiegner, V. Freudenthaler. "Aerosol optical properties during the Lindenberg Aerosol Characterization Experiment (LACE 98)", *J. Geophys. Res.* 107, doi:10.1029/2000JD000188, 2002.

Chang, F. and Z. Li, "Estimating the vertical variation of cloud droplet effective radius using multispectral near-infrared satellite measurements", *J. Geophys. Res.* 107(D15), 10.1029/2001JD000766, 2002.

Chang, F., Z. Li and S. Ackerman, "Examining relationships between cloud and radiation quantities derived from satellite observations and model calculations". *J. Clim.* 13, 3842-3859, 2000.

Chang, H. and T. Charalampopoulos, "Determination of the wavelength dependence of refractive indices of soot", *Proc. Roy. Soc. London*, 430, 577-591, 1990.

Charlock, T. *et al.*, "CERES/SARB Surface properties", Surface and Radiation Budget working group web page, http://snowdog.larc.nasa.gov/pub/surf/pages/explan.html, 2002.

Chen, R., F.L. Chang, Z. Li, R. Ferraro, F. Weng. "The impact of vertical variation of Cloud Droplet Size on cloud liquid water path and its potential for Rainfall detection". *Submitted to J. Atmos. Sci*., 2007

Chin, M., A. chu, R. Levy, L. Remer, Y. Kaufman, b. Holben, T. Eck, P. Ginoux, Q. Gao, "Aerosol distribution in the Northern Hemisphere during Ace-Asia: Results from global model, satellite observations, and sun photometer measurements". *J.*

Geophys, Res. 109(D23590), doi: 10.1029/2004JD004829, 2004.

Coakley, J. and C. Walsh, "Limits to the aerosol indirect radiative effect derived from observations of ship tracks." *J. Atmos. Sci.* vol. 59**,** pp. 668-680, 2002.

Conant, W., T. VanReken, T. Rissman, v. Varutbangkul, H. Jonsson, A. Nenes, J. Jimenez, A. Delia, r. Bahreini, G. Roberts, R. Flagan, J. Seinfeld, "Aerosol-cloud drop concentration closure in warm cumulus", *J. Geophys. Res.* 109(D13204), doi: 10.1029/2003JD004324, 2004.

Conny, J., Slater, J.," Black carbon and organic carbon in aerosol particles from crown fires in the Canadian boreal forest." *J. Geophys. Res.* 107**,** doi:10.1029/2001JD001528, 2002.

Cornet, C., H. Isaka, B. Guillemet and F. Szczap, "Neural network retrieval of cloud parameters of inhomogenous clouds from multispectral and multiscale radiance data: Feasibility study." *J. Geophys. Res.* vol 109, doi10.1029/2003JD004186, 2004.

Crutzen, P.J., L.E. Heidt, J.P. Krasnec, W.H. Pollock, and W. Seiler, "Biomass burning as a source of atmospheric gases CO, H_2, N_2O, NO, CH_3CL and COS", *Nature*, 282, 253-256, 1979.

Draxler, R.R., and G.D. Rolph, "HYSPLIT (HYbrid Single-Particle Lagrangian Integrated Trajectory) Model access via NOAA ARL READY Website" (http://www.arl.noaa.gov/ready/hysplit4.html), NOAA Air Resources Laboratory, Silver Spring, MD, 2003.

Dubovik, 0., A. Smirnov, B. N. Holben, M.D. King, Y.J. Kaufman, T.F. Eck, I. Slutsker, "Accuracy assessments of aerosol optical properties retrieved from Aerosol Robotic Network (AERONET) Sun and sky radiance measurements". *J. Geophys. Res.* 105, 9791-9806, 2000.

Dubovik, O., B. Holben, T.F. Eck, A. Smirnov, Y.J. Kaufman, M.D. King, D. Tanre, and I. Slutsker, "Variability of absorption and optical properties of key aerosol types observed in worldwide locations", *J. Atmos. Sciences, 59*, 590-608, 2002.

Eagen, R., P. Hobbs, L. Radke, " Measurements of CCN and cloud droplet size distribution in the vicinity of forest fires", *J. appl. Met.* 13, 553-537, 1974.

Eck, T. *personal communication*, 2006.

Eck, T., B. Holben, J. Reid, N. O'Neill, J. Schafer, O. Dubovik, A. Smirnoff, M Yamasoe, P. Artaxo. "High aerosol optical depth biomass burning events: a comparison of optical properties from different source regions". *Geophys. Res. Lett.* 30(20), 2035, doi:10.1029/2003GL017861, 2003.

Evans, L.F., I.A. Weeks, A.J. Eccleston, and D.R. Packham, "Photochemical ozone in smoke from prescribed burning of forests", *Environ. Sci. Technol*., 11, 896-900, 1977.

Feingold, G., L.A. Remer, J. Ramaprasad, Y. Kaufman, "Analysis of smoke impact on clouds in Brazilian biomass burning regions: an extension of Twomey's approach". *J. Geophys. Res.* **106,** 22,907-22,922, 2002.

Ferek, R., T. Garrett, P.V. Hobbes, S. Strader, D. Johnson, J. Taylor, K. Nielson, A. Ackerman, Y. Kogan, Q. Liu, B. Albrecht, D. Babb, "Drizzle Suppression in Ship Tracks", *J. Atmos. Sci*., 57, 2707-2728, 2000.

Ferrare, R.A., R.S. Fraser, and Y. Kaufman, "Satellite measurement of large-scale air-pollution: measurements of forest fire smoke", *J. Geophy. Res*., 95(D7*)*, 9911-9925, 1990.

Fiebig, M., A Petzold, U. Wandinger, M. Wendisch, C. Kiemle, A. Stifter, M. Ebert, T. Rother, U. Leiterer, "Optical Closure for an aerosol column: Method, accuracy, and inferable properties applied to a biomass-burning aerosol and its radiative forcing". *J. Geophys. Res.* 107, doi:10.1029/2000JD000192, 2002; web correction, 2003.

Fitzgerald, J and P. Spyers-Duran, "Changes in cloud nucleus concentration and cloud droplet concentration associated with pollution from St. Louis", *J. Appl. Met.* 12, 511-512, 1973.

Francis, P., P. Hignett, J. Taylor, "Aircraft observations and modeling of sky radiance distributions from aerosol during TARFOX", *J. Geophys. Res.*, 104(D2), 2309-2319, 1999.

Freud, E., D. Rosenfeld, M. Andreae, A. Costa and P. Artaxo, "Robust relations between CCN and the vertical evolution of cloud drop size distribution in deep convective clouds." *Atmos. Chem. Phys. Disc.* vol. 5, pp. 10155-10195, 2005.

Green, R. and J. Robbins, "ERBE-Like Inversion to Instantaneous TOA Flux, Algorithm theoretical basis document", *NASA CERES*, release 2.2, 37 pp, 1997.

Han, Q., W. Rossow, J. Zeng, R. Welch, "Three different behaviors of liquid water path of water clouds in cloud-aersol interactions", *J. Atmos. Sci.* 59, 726-736, 2002.

Hartley, S., P. Hobbs, J. Ross, P. Russell, J. Livingston, "Properties of aerosols aloft relevant to direct radiative forcing off the mid-Atlantic coast of the United States", *J. Geophys. Res.* 105, 9859-9885, 2000.

Haywood, J., P. Francis, O. Dubovik, M. Glew, B. Holben, "Comparison of aerosol size

distributions, radiative properties, and optical depths determined by aircraft observations and sun photometers during SAFARI 2000", *J. Geophys. Res. 108, (D13)*, 8473, doi:10.1029/2002JD002226, 2003.

Haywood, J. and O. Boucher, "Estimates of the Direct and Indirect Radiative Forcing due to Tropospheric Aerosols: a Review". *Revs. Geophys*, 38(4), p. 513-543, 2000.

Hegg, D., J. Livingston, P. Hobbs, T. Novakov, P. Russel, "Chemical apportionment of aerosol column optical depth off the mid-Atlantic coast of the United States", *J. Geophys. Res.*, 102, 25,293-25,303, 1997

Hobbs, P.V., J.S. Reid, R.A. Kotchenruther, R.J. Ferek, and R. Weiss, "Direct radiative forcing by smoke from biomass burning", *Science*, 275, 1777-1778, 1997.

Hobbs, P.V., L. Radke, S. Shumway, "Cloud condensation nuclei from industrial sources and their apparent influnce on precipitation in Washinton state", *J. Atmos. Sci.* 27, 81-89, 1970.

Holben, B., et al, "AERONET – a federated instrument network and data archive for aerosol characterization", *Remote Sens. Env.*, 66, 1-16, 1998.

Iwabuchi, H. and T. Hayasaka, "A multi-spectral non-local method for retrieval of boundary layer cloud properties from optical remote sensing data." *Rem. Sens. Env.*vol. 88, pp. 294-308, 2003.

Iwabuchi, H. and T. Hayasaka, "Effects of cloud horizontal inhomogeneity on the optical thickness retrieved from moderate-resolution satellite data." *J. Atmos. Sci.* vol. 59**,** pp 2227-2242, 2002.

Jeong, M.J., Z. Li, E. Andrews, S-C. Tsay, "Effect of aerosol humidification on the column aerosol optical thickness over the Atmospheric Radiation Measurement Southern Great Plains site". *J. Geophys. Res.* 112(D10202), doi:10.1029/2006JD007176, 2007.

Kato, S., M. Bergin, T. Ackerman, T. Charlock, E. Clothiaux, R. Ferrare, R. Halthore, N. Laulainen, G. Mace, J. Michalsky, D. Turner, "A comparison of the aerosol thickness derived from ground-based and airborne measurements", *J. Geophys. Res.*, 105, 14,701-14,717, 2000.

Kaufman, Y.J. and I. Koren, "Smoke and Pollution Aerosol Effect on Cloud Cover", *Science*, 313, 655-659, 2006.

Kaufman, Y. J., D. Tanre, O. Bouchier, "A Satellite View of Aerosols in the Climate System", *Nature*, 419**,** 215-223, 2002.

Kaufman, Y. J., P. V. Hobbs, V. W.. Kirchhoff, P. Artaxo, L. A. Remer, B. N. Holben,

M. D. King, D. E. Ward, E. M. Prins, K. M. Longo, L. F. Mattos, C. A. nobre, J.D. Spinhirne, Q. Ji, A. M. Thompson, J. F. Gleason, S. A. Christopher, S. C. Tsay, "Smoke, Clouds, and Radiation-Brazil (SCAR-B) Experiment". *J. Geophys. Res.* 103 (D24), 31,783-31,808, 1998a.

Kaufman, Y. and R. Fraser, "The Effect of Smoke Particles on Clouds and Climate Forcing". *Science*,**277**, 1636-1639, 1997.

Kaufman, Y. and T. Nakajima, "Effect of Amazon smoke on cloud microphysics and albedo – Analysis from Satellite imagery". *J. Appl. Met.* V32, p729-744, 1993.

Kaufman, Y. J., R. Fraser, R. Ferrare, "Satellite Measurements of Large-Scale Pollution: Methods", *J. Geophys. Res*. 95, 9895-9909, 1990a.

Kaufman, Y.J.,C.J. Tucker, I. Fung, "Remote Sensing of Biomass Burning in the Tropics". *J. Geophys. Res*. 95, 9927-9939, 1990b.

Keihl, A. and J. Haywood, "Solar radiative forcing by biomass burning aerosol particles during SAFARI 2000: a case study based on measured aerosol and cloud properties". *J. Geophys. Res*, 108(D13), doi 10.1029/2002JD002315, 2003.

King, M., S. Platnick, P. Hubanks, G. Arnold, E. Moody, G. Wind and B. Wind, "Collection 005 change summary for the MODIS cloud optical property (MOD06) Algorithm". Available: *http://modis-atmos.gsfc.nasa.gov/C005_Changes/C005_CloudOpticalProperties_ver311.pdf, 2007.*

King, M., W. Menzel, Y. Kaufman, D. Tanre, B.-C. Gao, S. Platnick, S. Ackerman, L. Remer, R. Pincus and P. Hubanks, "Cloud and Aerosol Properties, Precipitable Water, and Profiles of Temperature and Water Vapor from MODIS." *IEEE Trans. Geosci. Remote. Sens.* vol. 41, pp. 442-458, 2003.

King, M. D., Y. J. Kaufman, D. Tanre, T. Nakajima, "Remote Sensing of Tropospheric Aerosols from Space: Past, Present, and Future", *Bull. Am. Met. Soc.* 80**,** 2229-2259, 1999.

Koren,, I., Y. Kaufman, D. Rosenfeld, L. Remer and Y. Rudich, "Aerosol invigoration and restructuring of Atlantic convective clouds," *J. Geophys. Res. Lett.* Vol. 32, doi: 10.1029/2005GL023187, 2005.

Koren, I., Y.J. Kaufman, L.A. Remer, V. Martins, "Measurement of the effect of Amazon smoke on inhibition of cloud formation". *Science,* **303,** 1342-1345, 2004.

Kreidenweis, S., L. Remer, R. Bruintjes, O. Dubovik, "Smoke aerosol from biomass burning in Mexico: Hygroscopic smoke optical model". *J. Geophys. Res*. 106,

4831-4844, 2001.

Levy, R. C., L. Remer, S. Mattoo, E. Vermote, and Y. J. Kaufman, "Second-generation algorithm for retrieving aerosol properties over land from MODIS spectral reflectance". *J. Geophys. Res. (In press)*, 2007.

Li, Z., and L. Kou, "Atmospheric direct radiative forcing by smoke aerosols determined from satellite and surface measurements", *Tellus (B)*, 50, 543-554, 1998a.

Li, Z., "Influence of absorbing aerosols on the inference of solar surface radiation budget and cloud absorption", *J. Climate*, 11, 5-17, 1998b.

Loeb, N. and J. Coakley, "Inference of marine stratus cloud optical depths from satellite measurements: does 1D theory apply?" *J. Climate*, vol. 11, pp. 215-233, 1998.

Magi, B. I., P. V. Hobbs, B. Schmid, J. Redemann,, "Vertical profiles of light scattering, light absorption, and single scattering albedo during the dry, biomass burning season in southern Africa and comparisons of in situ and remote sensing measurements of aerosol optical depth". *J. Geophys. Res.* 108, *(D13)* doi:10.1029/2002JD002361, 2003.

Marshak, A., S. Platnick, T. Varnai, G. Wen and R. Cahalan, "Impact of 3D radiative effects on satellite retrievals of cloud droplet sizes." *J. Geophys. Res.*, vol. 111, doi. 10.1029/2005JD006686, 2006.

Martins, J.V., P. Artaxo, C. Liousse, J.S. Reid, P.V. Hobbs, and Y.J. Kaufman, "Effects of black carbon content, particle size, and mixing on light absorption by aerosols from biomass burning in Brazil", *J. Geophys. Res.*, 103, 32,041-32,050, 1998

McKeen, S.A., G. Wotawa, D. Parrish, J. Holloway, M. Buhr, G. Hubler, F. Fehsenfeld, J. Meagher, "Ozone Production from Canadian Wildfires during June and July of 1995". *J. Geophys. Res.* 107(D14), doi:10.1029/2001JD000697, 2002.

Miller, J. and T. O'Neill, "Multialtitude airborne observations of insolation effects of forest fire smoke aerosols at BOREAS: estimates of aerosol optical properties". *J. Geophys. Res.* 102, 29,729-29,736, 1997.

Mishchenko, M. I., L. D. Travis, and A. A. Lacis, *Scattering, Absorption, and Emission of Light by Small Particles*, Cambridge University Press, Cambridge. 2002.

Nakajima, T. and M. King, "Determination of the Optical Thickness and Effective Particle Radius of Clouds from Reflected Solar Radiation Measurements. Part 1: Theory." *J. Atmos. Sci.* vol. 47, pp. 1878-1893, 1990.

Navakov, T. and C.E. Corrigan, "Cloud Condensation activity of the organic component of biomass smoke particles". *Geophys Res. Letts.* 23(16), 2141-2144, 1996.

Novakov, T., D. Hegg and P. Hobbs, "Airborne measurements of carbonaceous aerosols on the East Coast of the United States", *J. Geophys. Res.*, 102, 30,023-30,030, 1997.

O'Neill, N. T., S. Thulaseraman, T. Eck, J. Reid, "Robust optical features of fine mode size distributions: Application to the Quebec smoke event of 2002", *J. Geophys. Res.* 110(D11207), doi: 10.1029/2004JD005157, 2005.

O'Neill, N. T., T. Eck, B. Holben, A. Smirnov, A. Royer, Z. Li, "Optical Properties of boreal forest fire smoke derived from sun photometry", *J. Geophys. Res.* 107(D11), doi:10.1029/2001JD000877, 2002.

Park, R.J., G.L. Stenchikov, K.E. Pickering, R.R. Dickerson, D.J. Allen, and S. Kondragunta, "Regional air pollution and its radiative forcing: Studies with a single-column chemical and radiation transport model", *J. Geophys. Res.*, 106(D22), 28,751-28,770, 2001.

Peng, Y., U. Lohman, R. Leaitch, C. Banic, M. Couture. "The Albedo-cloud droplet effective radius relationship for clean and polluted clouds from RACE and FIRE-ACE". *Geophys. Res. Lett.* V 107(D11), 4106, doi: 10.1029/2002D000281, 2002.

Penner, J.E., R.E. Dickinson, and C.A. O'Neill, "Effects of aerosol from biomass burning on the global radiation budget", *Science*, 256, 1432-1434, 1992.

Platnick, S., M. King, S. Ackerman, W. Menzel, B. Baum, J. Ridi, R. Frey, "The MODIS cloud products: Algorithms and examples from Terra". *IEEE Trans. Geosci. Remote. Sens.* **41**, 459-473, 2003.

Rajeev, K. and K. Parameswaran, "Iterative Method for the Inversion of Multiwavelength Lidar Signals to Determine Aerosol Size Distribution", *J. Appl. Opt.* 37, 4690-4700, 1998.

Ramathan, V., P.J. Crutzen, J.T. Kiehl, D. Rosenfeld, "Aerosols, climate, and the hydrological cycle". *Science*, v. 294, 2119-2124, 2001A

Ramanathan, V. et al, "Indian Ocean Experiment: An integrated analysis of the climate forcing and effects of the great Indo-Asian haze", *J. Geophys. Res.* 106, 28,371-28,398, 2001B.

Reid, J.S., P. Hobbs, C. Liousse, J Martins, R. Weiss, T. Eck, "Comparisons of techniques for measuring shortwave absorption and black carbon content of aerosols from biomass burning in Brazil", *J. Geophys. Res.* 103, 32031-32040, 1998A.

Reid, J. and P. Hobbes. “Physical and Optical properties of young smoke from individual biomass fires in Brazil”, *J.Geophys. Res.* 103(D24), 32013-32030, 1998B.

Reid, J.S., T.F. Eck, S.A. Christopher, P.V. Hobbs, and B. Holben,” Use of the Ångstrom exponent to estimate the variability of optical and physical properties of aging smoke particles in Brazil”, *J. Geophys. Res.*, 104, 27,473-27,489, 1999.

Remer, L., Y. Kaufman, d. Tanre, S. Mattoo, D. Chu., J. Martins, R.-R. Li, C. Ichoku, R. Levy, R. Kleidman, T. Eck, E. Vermote, B. Holben, “The MODIS aerosol algorithm, products, and validation”. *J. Atmos. Sci.* **62**, 947-973, 2005.

Remer, L. A., S. Gasso, D .A. Hegg, Y. J. Kaufman, and B. N. Holben, “Urban/industrial aerosol: Ground based Sun/sky radiometer and airborne in situ measurements”, *J. Geophys. Res*, 102, 16,849-16,859, 1997.

Remer, L. A. and Y.J. Kaufman, “Dynamic Aerosol Model: Urban/Industrial Aerosol”, *J. Geophys. Res.* 103, 13859-13871, 1998.

Remer, L .A., Y. J. Kaufman, B. N. Holben, A. M. Thompson, and D. McNamara, “Biomass burning aerosol size distribution and modeled optical properties”, *J. Geophys. Res.*, 103, 31,879-31,891, 1998.

Ricchiazzi, P., S. Yang, D Gautier, and D. Sowle, “SBDART: a research and teaching software tool for plane-parallel radiative transfer in the Earth's atmosphere”, *Bull. Amer. Met. Soc.*, 79, 2101- 2114, 1998.

Rissman, T. A., A. Nenes, J. Seinfeld. “Chemical amplification (or dampening) of the Twomey effect: Conditions derived from droplet activation theory”. *J. Atmos. Sci.* 61, pp 919-930. 2004.

Roberts, G.C., A. Nenes, J.H. Seinfeld, M.O. Andreae, “Impact of biomass burning on cloud properties in the Amazon Basin”. *J.Geophys.Res.* 108, 4062, doi:10.1029/2001JD000985, 2003.

Roberts, G.C., P. Artaxo, J. Zhou, E. Swietlicki, M. Andreae, “Sensititivity of CCN spectra on chemical and physical properties of aerosol: A case study from the Amazon Basin”. *J. Geophys. Res.* 107(D20), doi:10.1029/2001JD00583, 2002.

Rogers,R. and M. Yau, *A Short Course in Cloud Physics, 3rd edition.* Butterworth-Heinemann, 1996.

Rosenfeld, D., E. Cattani, S. Melani and V. Levizzani, “Considerations on Daylight Operation of 1.6 versus 3.7 μm Channel on NOAA and METOP Satellites.” *Bull. Am. Met. Soc.* pp. 873-881, June, 2004.

Rosenfeld, D. "TRMM observed first direct evidence of smoke from forest fires inhibiting rainfall", *Geophys. Res. Lett*. 26, 3105, 1999.

Rosenfeld, D. and I. Lensky, "Satellite-based Insights into Precipitation Formation Processes in Continental and Maritime Convective Clouds." *Bull. Am. Met. Assc*. Vol. 79**,** 2457-2476, 1998.

Ross, J. L., P. Hobbs, B. Holben, "Radiative Characteristics of regional hazes dominated by smoke from biomass burning in Brazil: Closure tests and direct radiative forcing", *J.Geophys. Res*. 103, 31,925-31,941, 1998.

Russell, P.B., J. Livingston, P. Hignett, S. Kinne, J. Wong, A. Chien, R. Bergstrom, P. Durkee, P. Hobbs, "Aerosol-induced radiative flux changes off the United States mid-Atlantic Coast: Comparison of values calculated from sun photometer and in situ data with those measured by airborne pyranometer". *J. Geophys. Res.* ***104,*** 2289-2307, 1999A.

Russell, P.B., P. Hobbs, L. Stowe, "Aerosol properties and radiative affects in the United States East Coast haze plume: an overview of the Tropospheric Aerosol Radiative Forcing Observational Experiment (TARFOX)", *J. Geophys. Res.* 104, 2213-2222, 1999B.

Russell, P.B., J. Redemann, B. Schmidt, R. W. Bergstrom, J.M. Livingston, D.M. McIntosh, S.A. Ramirez, S. Hartley, P.V. Hobbs, P.K. Quinn, C.M. Carrico, M.J. Rood, E. Ostrom, K.J. Noone, W. Hoyningen-Huene, and L. Remer, "Comparison of Aerosol Single Scattering Albedos Derived by Diverse Techniques in Two North Atlantic Experiments". *J. Atmos. Sci*. 59, 609-619, 2002.

Stephens, G. "Cloud feedbacks in the climate system: a critical review." *J. Climate*, vol. 18, 237-273, 2005.

Stephens, G. "The CloudSat Mission and the A-Train: a New Dimension of Space-Based Observations of Clouds and Precipitation", *Bull. Am. Met. Soc.*, pp 1771-1790, Dec. 2002.

Stith, J.L., F.R. Lawrence, and P.V. Hobbs, "Particle emissions and the production of ozone and nitrogen-oxides from the burning of forest slash", *Atmos. Environ.*, 15, 73-82, 1981.

Taubman, B.A., L. Marufu, B. Vant-Hull, C. Piety, B. Doddridge, R. Dickerson, Z. Li, "Smoke over Haze: Aircraft Observations of Chemical and Optical Properties and the Effects on Heating Rates and Stability". *J. Geophys. Res.* 109,(D2), 10.1029/2003JD003898, 2004.

Tanre, D., M. Herman, Y. Kaufman, "Information on aerosol size distribution contained

in solar reflected spectral radiances", *J. Geophys. Res.* 101(D14), 19043-19060, 1996.

Torres, O., P.K. Bhartia, J.R. Herman, A. Sinyuk, Paul Ginoux, and Brent Holben, "A long-term record of aerosol optical depth from TOMS observations and comparison to AERONET measurements". *J. Atmos. Sci.* 59, 398-413, 2002.

Vant-Hull, B., A. Marshak, L. Remer, and Z. Li, "The effects of scattering angle and cumulus cloud geometry on satellite retrievals of cloud drop effective radius". *Geosci. Rem. Sens. Lett.*, **45** No. 4 1039-1045, 2007.

Vant-Hull, B., Z. Li, B. Taubman, R. Levy, L. Marufu, F.L. Chang, B. Doddridge, R. Dickerson, "Smoke over Haze: Comparative analysis of satellite, surface radiometer and airborne in-situ measurements of aerosol optical properties and radiative forcing over the eastern U.S.", *J. Geophys. Res.* Doi: 10.1029/2004JD004518, 2004.

Varnai, T. and A. Marshak, "Observations of three-dimensional radiative effects that influence MODIS cloud optical thickness retrievals." *J. Atmos. Sci.* vol. 59, pp. 1607-1618, 2002.

Varnai, T. and A. Marshak, "Observations of three-dimensional radiative effects that influence satellite retrievals of cloud properties." *Q. J. Hungarian. Met. S.*, vol. 106, pp. 265-278, 2002.

Vermote, E. and A. Vermeulen, "Atmospheric Correction Algorithm: Spectral Reflectances (MOD09): Algorithm theoretical basis document", *NASA EOS-MODIS*, version 4.0, 103 pp, 1999.

Wang, J., S. A. Christopher, F. Brechtel, J. Kim, B. Schmid, J. Redemann, P. B. Russell, P. Quinn, B. N. Holben, "Geostationary Satellite Retrievals of Aerosol Optical Thickness During ACE-ASIA", *J. Geophys. Res.*, 108**,** (D23), 10.1029/2003JD003580, 2003

Wilks, D., *Statistical Methods in the Atmospheric Sciences.* Academic Press, 1995.

Wong, J., and Z. Li, "Retrieval of optical depth for heavy smoke aerosol plumes: uncertainties and sensitivities to the optical properties", *J. Atmos. Sci.*, 59, 250-261, 2002.

Yu, H., R. Fu, R. E. Dickinson, Y. Zhang, M. Chen, and H. Wang: 'Interannual variability of smoke and warm cloud relationships in the Amazon as inferred from MODIS retrievals'. *Remote Sens. Environ*. (In press) 2007